

**Sensitivity of an hadronic future circular collider to Higgs
boson pair production in the final state with four b-quarks**

Ana Luísa Moreira de Carvalho

Thesis to obtain the Master of Science Degree in

Physics Engineering

Supervisor(s): Dr. José Ricardo Gonçalo
Prof. Pedro Abreu

Examination Committee

Chairperson: Prof. Full Name

Supervisor: Prof. Full Name 1 (or 2)

Member of the Committee: Prof. Full Name 3

Month Year

11 Acknowledgments

12 I would like to express my sincere thanks to my supervisor Ricardo Gonçalo for his support, invaluable
13 scientific advise and inspirational enthusiasm, without which this work would not have been concluded.
14 To my co-supervisor, Pedro Abreu, I thank for his thorough reading of this thesis and for taking the time
15 to engage in interesting physics discussions.

16 I acknowledge the funding of this research by Fundação para a Ciência e Tecnologia - FCT, through
17 CERN/FIS-PAR/0008/2017 grant.

18 I am very thankful to Patricia Conde and Rute Pedro for fruitful discussions and very helpful advise.
19 To my master colleagues in the LIP ATLAS group, Aidan Kelly, António Costa and Ricardo Barrué, I
20 thank for the companionship and motivation throughout this journey.

21 I am thankful to Duarte Azevedo, Pedro Ferreira and Rui Santos for being our on-call theoreticians,
22 always available to help.

23 I would like to thank all my colleagues in the LIP ATLAS group for making me feel very welcome.
24 I extend my gratitude to everybody at LIP for making it a fantastic place to work. I would also like to
25 acknowledge the LIP IT and secretariat for the technical support.

26 To the people at CERN, namely Clement Helsens and Michele Selvaggi, I thank for the numerous
27 occasions in which they helped me regarding the FCC software and sample generation. I would also
28 like to acknowledge the CERN IT for the very efficient service.

29 I would like to thank my boyfriend, João Augusto, for his never ending patience and unconditional
30 support. To my friends of Chafarica I express my most sincere thanks for always being a great support,
31 source of joy and laughter.

32 To my sister I thank for always welcoming me home with a smile, for the numerous time she offered
33 to help and for all the memes that lighten up some of my days.

34 To my parents, I will never be able to thank enough. I thank them for their love, unconditional support,
35 inspiration, help in times of need,

36 Resumo

- 37** Inserir o resumo em Português aqui com o mximo de 250 palavras e acompanhado de 4 a 6 palavras-chave...

- 39 Palavras-chave:** palavra-chave1, palavra-chave2,...

40 **Abstract**

41 The production of pairs of Higgs bosons is a key benchmark process for future colliders because it
42 provides crucial insight into the Electroweak Symmetry Breaking mechanism but it is out of the current
43 reach of the Large Hadron Collider.

44 CERN is currently leading a study that analyzes the feasibility of a 100 km circular collider located
45 in the Geneva area. The hadronic Future Circular Collider (FCC-hh) is expected to work at a center of
46 mass energy of $\sqrt{s} = 100$ TeV and to collect a total integrated luminosity of $O(30)$ ab $^{-1}$.

47 This thesis describes a Monte Carlo study targeting the search for $hh \rightarrow b\bar{b}$ in a boosted kinematic
48 regime, using proton-proton collisions at center of mass energy of $\sqrt{s} = 100$ TeV. The focus is on the im-
49 pact of the granularity of hadronic calorimeter on the significance, S/\sqrt{B} , targeting detector optimization
50 studies for future colliders. In addition to traditional kinematic variables, jet substructure observables are
51 also explored.

52 For the FCC-hh, the achieved significance is $S/\sqrt{B} = 8.8 \pm 1.6$ (stat.) $^{+4.1}_{-3.0}$ (sys.) for an integrated
53 luminosity of $\mathcal{L} = 30$ ab $^{-1}$, which is above the 5σ threshold. When using particle flow jets, the signifi-
54 cance changes by approximately 54% over the range of detector configurations considered. The change
55 is more accentuated when using pure calorimeter jets ($\sim 71\%$).

56 **Keywords:** keyword1, keyword2,...

Contents

58	Acknowledgments	iii
59	Resumo	iv
60	Abstract	v
61	List of Tables	xi
62	List of Figures	xiv
63	Glossary	xviii
64	1 Introduction	1
65	2 The standard model and beyond	4
66	2.1 The Standard Model of Particle Physics	4
67	2.1.1 Higgs pair production	10
68	2.2 Going beyond	13
69	3 Collider experiments	17
70	3.1 Experimental aspects	18
71	3.2 The Large Hadron Collider	18
72	3.2.1 The ATLAS detector	20
73	3.3 Jet reconstruction	23
74	3.3.1 Jet properties and substructure observables	25
75	3.3.2 Jet grooming algorithms	26
76	3.4 Future Colliders	27
77	3.4.1 The hadronic Future Circular Collider	27
78	3.4.2 FCC-hh baseline detector	28
79	3.4.3 FCC-hh physics program	30
80	4 State of the art	31
81	4.1 Searches for Higgs pair production at the LHC	31
82	4.2 Feasibility studies for high-luminosity and future colliders	32
83	4.3 Hadronic calorimeter granularity studies	34

84	5 Sample generation and analysis tools	37
85	5.1 Fast simulation workflow	37
86	5.1.1 Particle flow and calorimeter reconstruction in Delphes	38
87	5.1.2 FCC-hh software	39
88	5.2 Signal and background samples	40
89	5.2.1 MadGraph	40
90	5.2.2 Pythia	42
91	5.2.3 Delphes	43
92	6 Analysis	46
93	6.1 Overview of the $hh \rightarrow b\bar{b}b\bar{b}$ channel	46
94	6.1.1 Event pre-selection	46
95	6.1.2 Signal characterization	47
96	6.1.3 Backgrounds	48
97	6.2 Analysis strategy	50
98	6.2.1 Implementation of b-tagging	52
99	6.2.2 Baseline analysis	53
100	6.2.3 Optimization	56
101	6.2.4 Handling of uncertainties	57
102	6.2.5 Trigger discussion	59
103	7 Results	61
104	7.1 Di-Higgs discovery potential at the FCC-hh	61
105	7.1.1 Comparing with the ATLAS detector	62
106	7.2 Hadronic calorimeter granularity studies for future colliders	63
107	7.2.1 Resolution of jet mass and N-subjetiness	65
108	7.2.2 Signal efficiency and significance	66
109	8 Conclusions	71
110	Bibliography	73
111	A Jet radius discussion	81
112	B Additional background processes	82
113	C Softdrop mass	83
114	D Samples generation: parameters	84
115	D.1 MadGraph	84
116	D.2 Pythia	84
117	E Cutflow tables	86

List of Tables

119	3.1 ATLAS tile and liquid argon hadronic calorimeters: summary of the pseudorapidity coverages and transversal segmentation (granularity)	21
120	3.2 Comparison between the working parameters of the LHC and of the FCC-hh. The values of the number bunches and of the number of events per bunch crossing are given assuming a bunch spacing of 25 ns.	28
121	3.3 Layout, granularity and energy resolution of the proposed hadronic calorimeter for the FCC-hh detector.	29
122	5.1 Summary of the effective cross sections ($\sigma \times BR$) and k factors of the signal and background samples used in the analysis.	44
123	5.2 Summary of the benchmark granularity configurations of the HCAL.	45
124	5.3 Summary of some key detector parameters for the FCC-hh and ATLAS detectors.	45
125	6.1 b-Tagging (black), c (blue) and light (red) mistag probabilities as a function of η and p_T of the (sub)jet. The momentum dependent factor, $(1 - p_T/15000)$, is common to the three probabilities.	53
126	7.1 Cumulative efficiency, in percentage, of each event selection criterion for the signal samples (SM, DM mediator and 2HDM). The absolute value of expected events after some key selection cuts is shown in curved brackets. The number of expected events is normalized to $\mathcal{L} = 30 \text{ ab}^{-1}$. The double horizontal line marks the pre-selection cuts. These results were obtained using the FCC-hh baseline detector design, as implemented in Delphes by the FCC-hh study group.	62
127	7.2 Cumulative efficiency, in percentage, of each event selection criterion for the background samples ($4b+j$, $jj+0/1/2\ j$ and $t\bar{t}+0/1/2j$). The absolute value of expected events after some key selection cuts is shown in curved brackets. The number of expected events is normalized to $\mathcal{L} = 30 \text{ ab}^{-1}$. The double horizontal line marks the pre-selection cuts. These results were obtained using the FCC-hh baseline detector design, as implemented in Delphes by the FCC-hh study group.	63

146	7.3 Cumulative efficiency, in percentage, of each event selection criterion for the signal sam-	
147	ples (SM, DM mediator and 2HDM). The absolute value of expected events after some	
148	key selection cuts is shown in curved brackets. The number of expected events is nor-	
149	malized to $\mathcal{L} = 30 \text{ ab}^{-1}$. The double horizontal line marks the pre-selection cuts. These	
150	results were obtained using the ATLAS detector design, as implemented in Delphes.	64
151	7.4 Cumulative efficiency, in percentage, of each event selection criterion for the background	
152	samples ($4b+j$, $jj+0/1/2\ j$ and $t\bar{t}+0/1/2j$). The absolute value of expected events after	
153	some key selection cuts is shown in curved brackets. The number of expected events is	
154	normalized to $\mathcal{L} = 30 \text{ ab}^{-1}$. The double horizontal line marks the pre-selection cuts.	
155	These results were obtained using the ATLAS detector design, as implemented in Delphes. 64	
156	7.5 Significances achieved with the ATLAS and FCC-hh detector configurations for $\mathcal{L} = 30 \text{ ab}^{-1}$	
157	for the three benchmark signal models: SM, 1 TeV DM mediator and 2HDM with $m_H = 900$	
158	GeV.	65
159	B.1 Effective cross section ($\sigma \times \text{BR} \times \text{k-factor}$), efficiency and expected number of events for	
160	$\mathcal{L} = 30 \text{ ab}^{-1}$ for the $t\bar{t}h + 0/1\ j(h \rightarrow b\bar{b})$ and $h + 0/1/2\ j(h \rightarrow b\bar{b})$ backgrounds.	82
161	D.1 Generator (MadGraph5) level cuts for the signal and background samples.	85
162	D.2 Pythia settings for the signal and background samples.	85
163	E.1 Summary of the significances obtained with particle flow and calorimeter jets for the base-	
164	line and optimized analysis for the SM signal.	86
165	E.2 Summary of the significances obtained with particle flow and calorimeter jets for the base-	
166	line and optimized analysis for the DM mediator and 2HDM signal processes.	86
167	E.3 Cumulative efficiency, in percentage, of each event selection criterion of the baseline	
168	analysis for the signal background samples, for particle flow jets (black) and calorimeter	
169	jets (blue). The double horizontal line marks the pre-selection cuts. These results were	
170	obtained using the ATLAS default detector, as implemented in Delphes.	87
171	E.4 Cumulative efficiency, in percentage, of each event selection criterion of the baseline	
172	analysis for the signal background samples, for particle flow jets (black) and calorimeter	
173	jets (blue). The double horizontal line marks the pre-selection cuts. These results were	
174	obtained using the ATLAS granularity.	88
175	E.5 Cumulative efficiency, in percentage, of each event selection criterion of the baseline	
176	analysis for the signal background samples, for particle flow jets (black) and calorimeter	
177	jets (blue). The double horizontal line marks the pre-selection cuts. These results were	
178	obtained using the ATLAS granularity with $\eta \times 4$	89
179	E.6 Cumulative efficiency, in percentage, of each event selection criterion of the baseline	
180	analysis for the signal background samples, for particle flow jets (black) and calorimeter	
181	jets (blue). The double horizontal line marks the pre-selection cuts. These results were	
182	obtained using the FCC granularity with $\phi/2$	90

183	E.7 Cumulative efficiency, in percentage, of each event selection criterion of the baseline analysis for the signal background samples, for particle flow jets (black) and calorimeter jets (blue). The double horizontal line marks the pre-selection cuts. These results were obtained using the FCC default detector design.	91
184		
185		
186		
187	E.8 Cumulative efficiency, in percentage, of each event selection criterion of the baseline analysis for the signal background samples, for particle flow jets (black) and calorimeter jets (blue). The double horizontal line marks the pre-selection cuts. These results were obtained using the FCC granularity with $\eta, \phi \times 2$	92
188		
189		
190		
191	E.9 Cumulative efficiency, in percentage, of each event selection criterion of the optimized analysis for the signal background samples, for particle flow jets (black) and calorimeter jets (blue). The double horizontal line marks the pre-selection cuts. These results were obtained using the ATLAS default detector, as implemented in Delphes.	93
192		
193		
194		
195	E.10 Cumulative efficiency, in percentage, of each event selection criterion of the optimized analysis for the signal background samples, for particle flow jets (black) and calorimeter jets (blue). The double horizontal line marks the pre-selection cuts. These results were obtained using the ATLAS granularity.	94
196		
197		
198		
199	E.11 Cumulative efficiency, in percentage, of each event selection criterion of the optimized analysis for the signal background samples, for particle flow jets (black) and calorimeter jets (blue). The double horizontal line marks the pre-selection cuts. These results were obtained using the ATLAS granularity with $\eta \times 4$	95
200		
201		
202		
203	E.12 Cumulative efficiency, in percentage, of each event selection criterion of the optimized analysis for the signal background samples, for particle flow jets (black) and calorimeter jets (blue). The double horizontal line marks the pre-selection cuts. These results were obtained using the FCC granularity with $\phi/2$	96
204		
205		
206		
207	E.13 Cumulative efficiency, in percentage, of each event selection criterion of the optimized analysis for the signal background samples, for particle flow jets (black) and calorimeter jets (blue). The double horizontal line marks the pre-selection cuts. These results were obtained using the FCC default detector.	97
208		
209		
210		
211	E.14 Cumulative efficiency, in percentage, of each event selection criterion of the optimized analysis for the signal background samples, for particle flow jets (black) and calorimeter jets (blue). The double horizontal line marks the pre-selection cuts. These results were obtained using the FCC granularity with $\eta, \phi \times 2$	98
212		
213		
214		

List of Figures

215	2.1 Schematic representation of the Standard Model of elementary particles. Particle are represented inside squares. The electric and color charge are shown in the right upper corner of each square. The spin is shown in the right lower corner. The mass of the particles is also shown, in electron Volt.	5
220	2.2 Postulated shape of the Higgs potential for $\mu^2 > 0$ (a) and $\mu^2 < 0$ (b).	8
221	2.3 Feynman diagrams of Higgs pair production from gluon fusion. Triple vertex diagram (left) and box diagram (right). The minus sign between the diagrams indicates that they interfere destructively.	11
224	2.4 Total cross sections at NLO in QCD for the six largest HH production channels at pp colliders. The thickness of the lines corresponds to the scale and PDF uncertainties added linearly.	13
227	2.5 Here, α_1 , α_2 and α_3 represent the coupling constants of $U_Y(1)$, $SU_L(2)$ and $SU_{color}(3)$, respectively. What is shown is the variation of the inverse of the coupling with the energy: on the left for the SM and on the right for the MSSM. Plots from Ref. [23].	14
230	2.6 BSM contributions to Higgs pair production from the spin-2 Kaluza-Klein graviton (a) and from the SUSY partner of the top quark (b). Figures from Refs. [26, 27], respectively.	16
232	3.1 ATLAS detector.	22
233	3.2 FCC detector baseline concept.	30
234	4.1 Exclusion limits (at 95% CL) on the cross section of resonant Higgs pair production from the decay of heavy scalar particles. These results were obtained using proton-proton collision data collected with the CMS (a) and ATLAS (b) detector at a CM energy of $\sqrt{s} = 8$ TeV and result from the combination of different channels. Plots from Refs. [70, 74], respectively.	33
239	4.2 Azimuthal distribution of the energy deposits in the ECAL and HCAL for a pair of K_L^0 with $E = 100$ GeV for an hadronic calorimeter with $20 \text{ cm} \times 20 \text{ cm}$ (a) and $5 \text{ cm} \times 5 \text{ cm}$ (b). Figures from Ref. [80] (based on Ref. [79]).	34

242	4.3 Jet mass (a) and jet mass resolution (b) plots in $t\bar{t}$ events for eflow jets with $p_T > 3$ TeV for	
243	three different HCAL and ECAL configurations: HCAL(ECAL) 0.1(0.025) $\eta \times 5.6(1.4)$ $^\circ \phi$,	
244	HCAL(ECAL) 0.05(0.012) $\eta \times 2.8(0.7)$ $^\circ \phi$ and HCAL(ECAL) 0.025(0.006) $\eta \times 1.4(0.35)$ $^\circ \phi$.	
245	Plots from Ref. [80].	36
246	4.4 τ_{32} resolution plots for QCD dijet events reconstructed using eflow jets (a) and tower jets	
247	(b). Plots from Ref. [81].	36
248	4.5 τ_{21} variable for 20 TeV W (black) and QCD jets (red) for three HCAL granularities: $\Delta\eta \times$	
249	$\Delta\phi = 0.1 \times 0.1$ (left), $\Delta\eta \times \Delta\phi = 0.022 \times 0.022$ (middle) and $\Delta\eta \times \Delta\phi = 0.005 \times 0.005$	
250	(right). Plots from Ref. [80].	36
251	6.1 (a) Higgs pairs branching ratios, (b) event topology targeted by a boosted analysis.	47
252	6.2 (a) $\Delta\phi$ between the Higgs candidates, $\Delta\phi(hh)$, (b) ΔR between the b quarks coming from	
253	the decay of the leading Higgs candidate, h_1 . To obtain this plot the cut $ M - 125 < 40$	
254	GeV was applied in addition to the pre-selection cuts.	49
255	6.3 Example of diagrams that contribute to the QCD multijet background: five final state jets,	
256	four of which are b-jets (left), three final state jets (middle) and four final state jets (right).	
257	Here, q stands for a light quark/jet.	50
258	6.4 Dominant diagrams of $pp \rightarrow t\bar{t}$ at LO.	51
259	6.5 p_T distributions for the leading (a) and sub leading (b) Higgs candidates. The signal is the	
260	SM $hh \rightarrow b\bar{b}$ process. The histograms are normalized to unit area.	51
261	6.6 η (a) and softdrop mass (b) distributions for the leading Higgs candidate. The signal is the	
262	SM $hh \rightarrow b\bar{b}$ process. The histograms are normalized to unit area.	51
263	6.7 Distributions of the $\Delta\eta$ between the Higgs candidates (a) and of the τ_{21} variable for the	
264	leading Higgs candidate (b). The histograms are normalized to unit area.	52
265	6.8 Minimum ΔR between b quarks and subjets of the $R = 0.8$ jets.	52
266	6.9 p_T distributions for the leading (a) and sub leading Higgs candidates (b). The histograms	
267	are normalized to $\mathcal{L} = 30 \text{ ab}^{-1}$	54
268	6.10 (a) p_T distribution for the Higgs pair, (b) τ_{21} variable for the leading Higgs candidate. The	
269	histograms are normalized to $\mathcal{L} = 30 \text{ ab}^{-1}$	55
270	6.11 (a) H_2 variable for the leading Higgs candidate, (b) softdrop mass distribution for the	
271	leading Higgs candidate. The histograms are normalized to $\mathcal{L} = 30 \text{ ab}^{-1}$	55
272	6.12 S/\sqrt{B} as a function of the cut on the p_T of the leading Higgs candidate, $p_T(h_1)$ (a) after	
273	the pre-selection cuts and of the sub leading Higgs candidate, $p_T(h_2)$ (b) after the cut on	
274	$p_T(h_1)$	57
275	6.13 S/\sqrt{B} as a function of the cut on the p_T of the Higgs pair, $p_T(hh)$ (a) after the cut on	
276	$p_T(h_1)$ and as a function of the τ_{21} variable for leading Higgs candidate, $\tau_{21}(h_1)$ (b) after	
277	the cut on $p_T(hh)$	57

278	6.14 S/\sqrt{B} as a function of the cut on the $\Delta\eta$ between the Higgs candidates, $\Delta\eta(hh)$ (a) after 279 the cuts on the transverse momenta and on the τ_{21} variables and as a function of the 280 second Fox-Wolfram momentum for the leading Higgs candidate, $H_l(h_1)$ (b) after the cuts 281 on the transverse momentums, τ_{21} and $\Delta\eta$	58
282	7.1 Leading Higgs candidate softdrop mass after the pre-selection cuts for particle flow (a) 283 and calorimeter (b) jets. The colors indicate the different detector configurations. The 284 x axis range is from 80 GeV to 160 GeV in order to make the differences between the 285 histograms more clear.	67
286	7.2 Invariant mass of the Higgs pair for the SM signal. The plots include the events that pass 287 all the analysis cuts. The colors indicate the different detector configurations.	67
288	7.3 Invariant mass of the Higgs pair for the 1 TeV DM mediator (a) and for the 2HDM with 289 $m_H = 900$ GeV (b). The plots include the events that pass all the analysis cuts. The 290 colors indicate the different detector configurations.	68
291	7.4 Leading Higgs candidate τ_{21} distribution for eflow jets (a) and for HCAL jets (b). The 292 colors indicate the different detector configurations. The distributions are shown for the 293 signal (filled lines) and for the $4b + j$ background (dashed lines).	68
294	7.5 Signal efficiency as a function of the detector configuration for particle flow jets (a) and 295 for calorimeter jets (b). Three signal models are shown: SM (filled squares), 1 TeV DM 296 mediator (empty squares) and type II 2HDM with $m_H = 900$ GeV (crosses). The statistical 297 error bars are drawn but are smaller than the markers.	69
298	7.6 Significance as a function of the detector configuration for the SM signal, for the baseline 299 (a) and optimized (b) analyses. The significances are shown for eflow jets (squares) and 300 pure HCAL jets (triangles).	69
301	7.7 Significance as a function of the detector configuration for the DM mediator signal, for 302 the baseline (a) and optimized (b) analyses. The significances are shown for eflow jets 303 (squares) and pure HCAL jets (triangles).	70
304	7.8 Significance as a function of the detector configuration for the 2HDM signal, for the base- 305 line (a) and optimized (b) analyses. The significances are shown for eflow jets (squares) 306 and pure HCAL jets (triangles).	70
307	A.1 $\Delta R(b, \bar{b})$ distributions for $p_T(h_1) > 200/300$ GeV (solid blue/black) and for $p_T(h_1, h_2) >$ 308 $200/300$ GeV (dashed blue/black).	81
309	C.1 Correlation between the maximum ΔR between the Higgs candidate jet and one of the b 310 quarks (y axis) and the jet's mass (x axis). The horizontal line corresponds to $\Delta R = 0.8$. .	83
311	F.1 τ_{21} distribution for the sub leading Higgs candidate for the baseline analysis. The his- 312 togram is normalized to $\mathcal{L} = 30 \text{ ab}^{-1}$	99

313	F.2 Sub leading Higgs candidate τ_{21} distribution for eflow jets (a) and for HCAL jets (b). The colors indicate the different detector configurations. The distributions are shown for the signal (filled lines) and for the $jj + 0/1/2 j$ background (dashed lines).	99
314		
315		
316	F.3 Signal efficiency as a function of the detector configuration for particle flow jets (a) and for calorimeter jets (b). Three signal models are shown: SM (filled squares), 1 TeV DM	
317	mediator (empty squares) and type II 2HDM with $m_H = 900$ GeV (crosses). The statistical	
318	error bars are drawn but are smaller than the markers.	100
319		

Glossary

2HDM	Two Higgs Doublet Model
ATLAS	A Toroidal LHC Apparatus
BR	Branching Ratio
BSM	Beyond the Standard Model
CERN	European Organization for Nuclear Research
CMS	Compact Muon Solenoid
ECAL	Electromagnetic Calorimeter
EM	Electromagnetic
HCAL	Hadronic Calorimeter
ID	Inner Detector
LHC	Large Hadron Collider
LO	Leading Order
NLO	Next to Leading Order
QCD	Quantum Chromodynamics
QED	Quantum Electrodynamics
QFT	Quantum Field Theory
SM	Standard Model
SUSY	Super Symmetry
TileCal	Tile Calorimeter
VEV	Vacuum Expectation Value

321 **Chapter 1**

322 **Introduction**

323 It is the ultimate goal of particle physics to discover and study all of Nature's fundamental particles and
324 to understand their interactions. Through a joint endeavor of theorists and experimentalists, models that
325 describe particle's dynamics and properties can be precisely probed at collider experiments such as the
326 Large Hadron Collider (LHC).

327 We know today that matter particles interact by means of four fundamental forces: electromagnetic,
328 weak, strong and gravitational, of which the first three are associated with mediator particles. We even
329 know that a very special particle, the Higgs boson, is linked to the mechanism that generates the mass
330 of the mediator particles. It is called the Electroweak Symmetry Breaking (EWSB) mechanism and it
331 involves the spontaneous breaking of a gauge symmetry. Through Yukawa couplings, the Higgs boson
332 is also responsible for the masses of fermions. This knowledge is beautifully summarized in the Standard
333 Model of Particle Physics (SM) that was developed in the 1960's and 1970's, long before many of the
334 particles it predicts were discovered. The extraordinary precision of the predictions it delivers make it
335 a very successful model. The Higgs boson, is the most recent elementary particle to be discovered in
336 2012 at the LHC, which marks an important point in the history of particle physics: we have now found
337 all the particles predicted by the SM and yet we know that it cannot be the whole story. Mainly because
338 there are experimental evidences of physics that it cannot explain.

339 From the theoretical point of view, this is enough motivation to construct models that extend the SM
340 but that can still deliver predictions that are compatible with experimental data. From the experimental
341 standpoint, this is an indication that we need to keep increasing the precision of our measurements and
342 probing new kinematic regimes in the hope of finding more discrepancies with the SM or some hint that
343 some new phenomenon is taking place.

344 A higher precision requires a larger integrated luminosity and a larger center of mass energy opens
345 the door for the exploration of new kinematic regimes. Very recently, work towards the upgrade of the
346 LHC to its High-Luminosity (HL) version has began. It is expected to work for a period of ten years
347 between 2026 and 2036 and it will extend the experimental reach of the LHC. In order to keep extending
348 the physics reach of the LHC and HL-LHC, new colliders with unprecedentedly high center of mass
349 (CM) energies are currently being designed in the hope that they begin to deliver data shortly after the

350 HL-LHC has reached its full discovery potential. One of these projects is the hadronic Future Circular
351 Collider (FCC-hh) that consists of a 100 km ring located in the Geneva area and it is expected to work
352 at a CM energy of 100 TeV. The FCC-hh will deliver a peak luminosity of $\mathcal{L} = 30 \times 10^{34} \text{ cm}^{-2}\text{s}^{-1}$ in
353 its ultimate phase. This will result in $O(30) \text{ ab}^{-1}$ per experiment which corresponds to ten times the
354 expected integrated luminosity by the end of the HL-LHC operation.

355 The next milestone for the FCC-hh project is the submission of a Conceptual Design Report by the
356 end of 2018. This document will be used as input for the next meeting of the European Strategy for
357 Particle Physics that will take place in the beginning of 2019. It should present a baseline design for the
358 detector, a first cost estimate and preliminary analysis for physics benchmark processes demonstrating
359 the physics reach of such a machine.

360 Both in the HL-LHC and in future colliders, one of the most important benchmark processes is the
361 production of pairs of Higgs bosons. Firstly, this process is predicted by the SM but has not yet been
362 measured which is due to its very small cross section and overwhelming backgrounds. Furthermore,
363 it provides unique insight into the EWSB mechanism because it is sensitive to the shape of the Higgs
364 potential and can also be used to probe physics beyond the SM (BSM).

365 In this work we study Higgs pair production at a CM energy of $\sqrt{s} = 100 \text{ TeV}$ using the final state with
366 four b quarks. This final state because benefits from the large branching fraction of the Higgs boson to
367 a pair of b quarks. However, in this channel, the multijet production through Quantum Chromodynamics
368 (QCD) interactions is extremely overwhelming. Nonetheless, it is a well known feature of QCD interac-
369 tions that the partons (and jets) produced tend to have a low transverse momentum (p_T). This indicates
370 that exploring a high p_T region of the phase space could be the key to suppress this background. In
371 this kinematic regime, traditional jet reconstruction techniques, that try to establish a one-to-one cor-
372 respondence between partons and jets, begin to fail because the decay products of heavy and highly
373 boosted particles become more collimated as the p_T of the mother particles increase. State of the art
374 jet reconstruction techniques make use of jets with a larger radius parameter to reconstruct both decay
375 products (two b quarks) as a single jet that can then be used as a proxy for the original particle (a Higgs
376 boson). In order to recover as much information as possible from these jets, it is important to analyze
377 their intrinsic structure, referred to as substructure.

378 Jet substructure techniques explore the existence of localized energy maximums inside the large- R
379 jets (subjets). For example, a jet containing the two b quarks from the decay of a Higgs boson is
380 expected to be more consistent with having two subjets than a jet produced by a QCD process. From
381 the standpoint of detector design for the FCC-hh, as well as for future upgrades of existent detectors, the
382 ability to resolve the substructure of large- R jets is a key requirement for which can be helpful a highly
383 granular hadronic calorimeter (HCAL).

384 The main goal of this thesis is to use boosted di-Higgs production in the four b quarks final state to
385 study the influence of the granularity of the HCAL in significance of the detection that can be achieved.

386 Chapter 2 presents an overview of the SM. It summarizes its particle content and interactions and
387 introduces the mathematical formulation of the EWSB breaking mechanism. The successes and short-
388 comings of the SM are presented and several BSM models are introduced and their motivations dis-

389 cussed. Finally, a theoretical description of the production of Higgs pairs is provided.

390 The FCC-hh baseline accelerator and detector were highly based on LHC and its current experiments,
391 namely ATLAS and CMS. In chapter 3, after a brief discussion of the general features of particle
392 accelerators, we introduce the LHC and the ATLAS experiment. A discussion of jet reconstruction is
393 included. We then introduce the FCC-hh accelerator and its current baseline detector design. Some key
394 detector parameters are compared to ATLAS.

395 In chapter 4 we present the state of the art of searches for Higgs pair production at the LHC and
396 of feasibility studies targeting searches for this process at future colliders (High Luminosity LHC and
397 FCC-hh). We also review previous studies that focus on the impact of the HCAL granularity on the jet
398 mass and jet substructure observables resolution.

399 In chapter 5 we describe in detail the Monte Carlo samples that were used in this work. In addition,
400 the different detector configurations that were tested are described. Chapter 6 entails the description
401 of the analysis strategy and its optimization. A comprehensive characterization of the signal and back-
402 grounds processes is provided.

403 In chapter 7 we present and discuss the main results. We focus on the resolution of the jet mass
404 and of the ratio of N-subjetiness variables, namely, τ_{21} . In addition, we analyze how the significance
405 changes as the granularity of the HCAL is varied. The results obtained using particle flow jets and pure
406 calorimeter jets are compared.

407 Finally, conclusions are drawn in chapter 8.

⁴⁰⁸ **Chapter 2**

⁴⁰⁹ **The standard model and beyond**

⁴¹⁰ The Standard Model (SM) is the theoretical framework that summarizes our present knowledge of par-
⁴¹¹ ticle physics. In section 2.1, we provide an overview of this model, focusing on the Higgs mechanism.
⁴¹² In section 2.2, we motivate the need to explore models beyond the SM and introduce some of the most
⁴¹³ well known beyond the SM (BSM) models. In section 2.1.1, we provide a theoretical description of the
⁴¹⁴ production of Higgs boson pairs which is the physical process that is under study throughout this work.

⁴¹⁵ **2.1 The Standard Model of Particle Physics**

⁴¹⁶ The Standard Model of particle physics summarizes our present knowledge of fundamental particles
⁴¹⁷ and their interactions. It is formulated in the framework of Quantum Field Theory (QFT) and describes
⁴¹⁸ the subatomic world in terms of fields whose excitations are the particles we can detect. The particle
⁴¹⁹ content of the SM is summarized in figure 2.1. Each particle is represented inside a square. The electric
⁴²⁰ and color charge are shown in the right upper corner and the spin in the right lower corner. The mass
⁴²¹ of the particles are given in electron-Volt (eV) on top of each square (M standing for Million eV and G
⁴²² standing for Billion eV). There are two types of fundamental particles: matter particles and force carriers.

⁴²³ Matter particles are the building blocks of all the matter in our world. They come in two groups,
⁴²⁴ leptons and quarks. Quarks make up atomic nuclei; leptons, namely electrons and muons, can orbit
⁴²⁵ atomic nuclei forming atoms. Quarks and leptons are elementary fermions which means they have half-
⁴²⁶ integer spin. There are six flavors of quarks: three of the 'up type' (up, charm and top represented by
⁴²⁷ u , d and t) with electric charge of $+2/3$ and three of 'down type' (down, strange and bottom represented
⁴²⁸ by d , s and b) with electric charge of $-1/3$. Similarly, we have three leptons with charge -1 (electron,
⁴²⁹ muon and tau represented by e , μ and τ) and three neutral leptons (electron, muon and tau neutrinos
⁴³⁰ represented by ν with the symbol of the corresponding charged lepton as subscript) that are, within the
⁴³¹ SM, massless. We can classify quarks and leptons in three generations, each composed of an up type
⁴³² and down type quark or of a charged lepton and the corresponding neutrino.

⁴³³ The force carriers, technically called gauge bosons, are particles associated with the fundamental

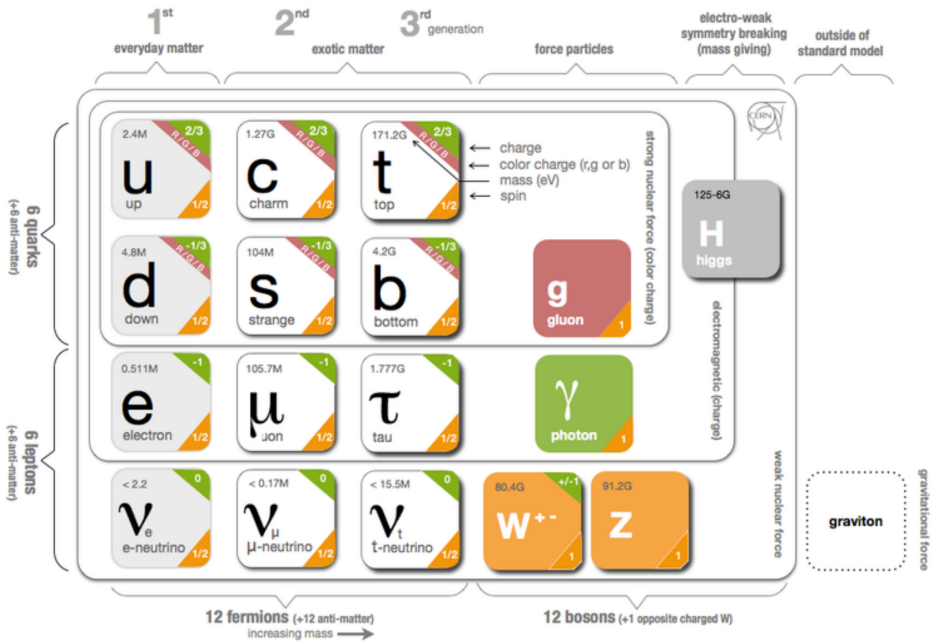


Figure 2.1: Schematic representation of the Standard Model of elementary particles. Particle are represented inside squares. The electric and color charge are shown in the right upper corner of each square. The spin is shown in the right lower corner. The mass of the particles is also shown, in electron Volt.

interactions: strong, electromagnetic, weak and gravitational ¹. Each interaction can be interpreted as the result of the exchange of the corresponding gauge boson. Gluons (g) and the photon (γ) are the mediators of the strong and electromagnetic interactions, respectively. They are massless, electrically neutral and have spin 1. The W^\pm and Z bosons are the mediators of the weak interaction and have a mass of 80.4 and 91.2 GeV, respectively. The W^+ and W^- bosons have electric charges of +1 and -1, respectively and spin 1. The Z boson is electrically neutral and also has spin 1. The gauge bosons can also be referred to as vector bosons because they have spin equal to one.

In addition to matter particles and gauge bosons, the theoretical formulation of the SM rests on the existence of the Higgs boson that is an electrically neutral and spin 0 particle. It has a mass of 125 GeV and it interacts with every particle that has mass.

Historically, an empirically successful quantum theory of electromagnetism, Quantum Electrodynamics (QED), was developed in the late 1940's. In the early 1950's there were high hopes that quantum theories could also be formulated for the weak and strong interactions. This is the context in which Yang-Mills theories emerged. They extend the concept of gauge theory from abelian groups, that led to the development of QED, to non-abelian gauge groups. However, the quanta of the fields predicted by these theories must be massless in order to maintain gauge invariance. Therefore, they were set aside until the 1960's when the idea of particles acquiring mass through symmetry breaking in massless theories was put forward by Goldstone [1], Nambu and Jona-Lasinio [2]. In the following paragraphs we discuss in more detail the caveats of Yang-Mills theories and the phenomenon of Spontaneous Symmetry

¹ The gauge boson that corresponds to the gravitational force has not yet been found. In addition we still do not have a theory that successfully describes gravitation in the framework of QFT so we will not include the gravitational force or its gauge boson in any of the following discussions. Moreover, the gravitational interaction is not relevant for the energy ranges studied.

453 try Breaking (SSB) as the basis of the modern Higgs mechanism. We then describe this mechanism in
 454 the framework of the SM.

455 On the one hand, if one takes a Yang-Mills theory, it becomes clear that it is not possible to include
 456 in the Lagrangian a mass term for the gauge bosons because it is not invariant under a gauge transfor-
 457 mation. This would not be a problem if we just wanted to describe electromagnetic or strong interactions
 458 because the gauge bosons associated with these interactions, the photon and the gluons, are indeed
 459 massless. However, for the weak interactions this is not the case. Even before the discovery of the Z and
 460 W^\pm bosons [3, 4] there was experimental evidence of the short range character of the weak interactions
 461 which indicated that the corresponding gauge bosons should be massive.

462 On the other hand, spontaneous symmetry breaking (SSB) is a phenomenon through which the
 463 invariance of a system under a certain symmetry group is destroyed [5]. The system may then be in-
 464 variant under a subgroup of the initial symmetry but the invariance under the original symmetry group is
 465 no longer present. In particle physics, this happens because the vacuum of the system (lowest energy
 466 states) does not share the symmetry of the Lagrangian. The SSB mechanism predicts the existence
 467 of scalar massless particles, the Nambu-Goldstone bosons, as a consequence of the Goldstone theo-
 468 rem [1] (the number depends on the number of generators of the original and final symmetry groups).
 469 Though, when considering this mechanism we get once again massless particles which does not seem
 470 to be a step in the right direction if we wish to describe weak interactions.

471 However, the real breakthrough occurs when we combine a theory with local gauge invariance with
 472 the mechanism of SSB. In this case the Nambu-Goldstone bosons do not appear and it is possible to
 473 give mass to the gauge bosons. This is the Higgs mechanism, proposed independently by P.W. Higgs
 474 [6], F. Englert and R. Brout [7] and by G. Guralnik, C. R. Hagen and T. Kibble [8] in 1964.

475 The SM is a non-abelian gauge theory with spontaneous symmetry breaking. It is locally invariant
 476 under the following symmetry group:

$$SU_{color}(3) \times SU_L(2) \times U_Y(1), \quad (2.1)$$

477 where the $SU_{color}(3)$ group describes the strong interactions (QCD) and the $SU_L(2) \times U_Y(1)$ group
 478 describes the electroweak interactions. Here, L stands for left and Y stands for hypercharge. In the SM
 479 the Higgs mechanism, which we now describe, is realized in the $SU_L(2) \times U_Y(1)$ group. The Lagrangian
 480 corresponding to the Higgs and gauge sectors of this theory is given by:

$$\mathcal{L} = (D_\mu \phi)^\dagger (D^\mu \phi) - V(\phi^\dagger \phi) - \frac{1}{4} W_{\mu\nu}^a W^{a\mu\nu} - \frac{1}{4} B_{\mu\nu} B^{\mu\nu}, \quad (2.2)$$

where the Higgs potential, $V(\phi^\dagger \phi)$, is given by:

$$V(\phi^\dagger \phi) = \mu^2 \phi^\dagger \phi + \lambda (\phi^\dagger \phi)^2. \quad (2.3)$$

481 $W_{\mu\nu}^a$ and $B_{\mu\nu}$ are the field tensors, defined as a function of the gauge fields of $SU_L(2)$ and $U_Y(1)$,
 482 W_μ^a ($a = 1, 2, 3$) and B_μ , respectively:

$$W_{\mu\nu}^a = \partial_\mu W_\nu^a - \partial_\nu W_\mu^a - g\epsilon^{abc}W_\mu^b W_\nu^c \quad (2.4)$$

$$B_{\mu\nu} = \partial_\mu B_\nu - \partial_\nu B_\mu \quad (2.5)$$

483 where g is the coupling constant associated with the $SU_L(2)$ group and ϵ^{abc} is the completely anti-
484 symmetric tensor in 3 dimensions. The covariant derivative, D_μ , is introduced to preserve local gauge
485 invariance and is given by:

$$D_\mu \phi = \left(\partial_\mu + igW_\mu^a T^a + i\frac{g'}{2} B_\mu \right) \phi. \quad (2.6)$$

486 $T^a = \frac{\tau^a}{2}$ (where τ^a are the Pauli matrices) are the $SU_L(2)$ group generators in the fundamental representation and g' is the coupling constant associated with the $U_Y(1)$ group.

Due to the requirement of Lorentz invariance, only the scalar field, ϕ , can have a vacuum expectation value (VEV), v , different from zero ². The values of v are determined by the minima of the potential:

$$v = 0 \quad \text{or} \quad v = \sqrt{\frac{-\mu^2}{2\lambda}}. \quad (2.7)$$

488 For the equation on the right (for which we get $v \neq 0$) we only obtain a real value for v (which is a
489 requirement for the VEV of a theory) if $\mu^2 < 0$. Therefore we conclude that the equation on the right
490 corresponds to $\mu^2 \leq 0$ while the equation on the left corresponds to $\mu^2 \geq 0$. In both cases λ has to
491 be larger than zero to guarantee that the energy is bounded from below³ because in Eq. 2.3 λ is the
492 coefficient of the term with the highest power in ϕ and therefore determines the concavity of the potential.

493 The shapes of the Higgs potential for $\mu^2 > 0$ and $\mu^2 < 0$ are shown in Figures 2.2(a) and 2.2(b),
494 respectively. For $\mu^2 > 0$ we have a single minimum located at $\langle \phi \rangle = 0$. For $\mu^2 < 0$ the potential has the
495 shape of a 'Mexican hat'. There is an infinite number of minima located in a circumference centered at
496 zero. In this case the minima occur for $\langle \phi \rangle, \langle \phi^\dagger \rangle \neq 0$. Therefore the field acquires a VEV different than
497 zero and this is what leads to the SSB.

We can now write the scalar field in terms of its minimum value, v , and of oscillations around that minimum, h (which corresponds to the Higgs field):

$$\phi = \begin{bmatrix} 0 \\ v + \frac{h}{\sqrt{2}} \end{bmatrix} \quad (\text{unitary gauge}). \quad (2.8)$$

498 If we expand the first term of the Lagrangian shown in Eq. 2.2 using Eq. 2.6 and Eq. 2.8 and taking into
499 consideration that $W_\mu^a T^a$ represents a sum over all values of a we get

²The other fields that appear in Eq. 2.2 are vector fields. If they were to acquire a VEV different from zero that would break Lorentz invariance.

³In a purely mathematical formulation this means that the function that represents the Higgs potential is concave upwards.

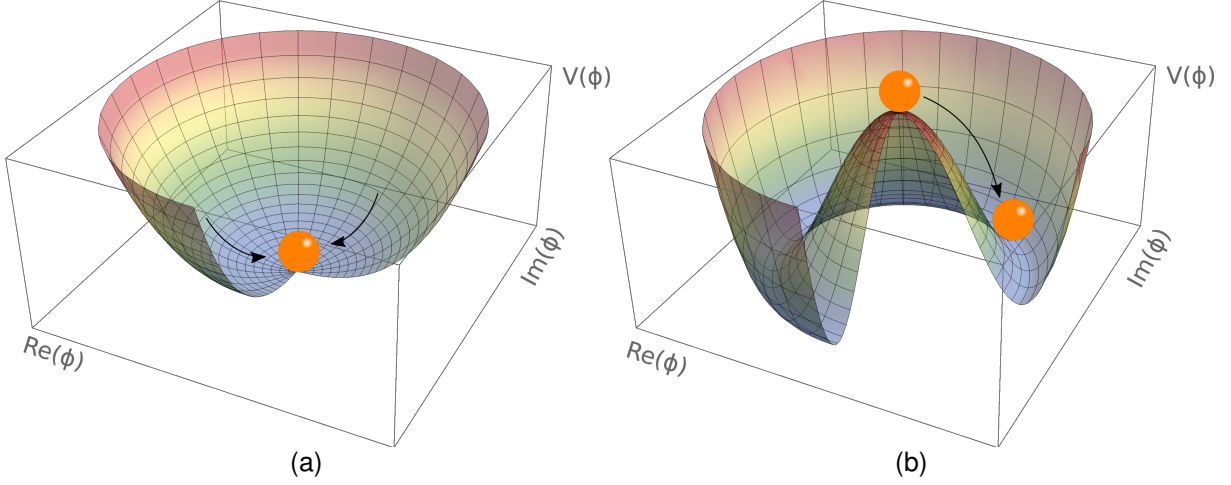


Figure 2.2: Postulated shape of the Higgs potential for $\mu^2 > 0$ (a) and $\mu^2 < 0$ (b).

$$\mathcal{L} = \frac{1}{4} \left(v^2 + \frac{h^2}{2} + \frac{2}{\sqrt{2}} vh \right) [g^2 (W_\mu^1 W^{1\mu} + W_\mu^2 W^{2\mu} + W_\mu^3 W^{3\mu}) - 2gg' B^\mu W_\mu^3 + g'^2 B_\mu B^\mu] + \dots . \quad (2.9)$$

We see that for the W_μ^1 and W_μ^2 fields we have only terms that are quadratic in these fields. These correspond to mass terms. However, for the W_μ^3 and B_μ fields there is a term that mixes the two fields. To obtain the physical states of the theory we need to transform these fields in order to get rid of the mixing term which is not physical. We can start by writing the last three terms of Eq. 2.9 in a matrix form and diagonalize the corresponding matrix:

$$\begin{bmatrix} g^2 & -gg' \\ -gg' & g'^2 \end{bmatrix} \begin{bmatrix} W_\mu^3 \\ B_\mu \end{bmatrix} \xrightarrow{\text{Diagonalization}} \begin{bmatrix} 0 & 0 \\ 0 & g^2 + g'^2 \end{bmatrix} \begin{bmatrix} A_\mu \\ Z_\mu \end{bmatrix}. \quad (2.10)$$

A_μ and Z_μ are the physical fields that are related with W_μ^3 and B_μ by means of a rotation matrix:

$$\begin{bmatrix} A_\mu \\ Z_\mu \end{bmatrix} = \begin{bmatrix} \cos \theta_W & -\sin \theta_W \\ \sin \theta_W & \cos \theta_W \end{bmatrix} \begin{bmatrix} W_\mu^3 \\ B_\mu \end{bmatrix} \quad (2.11)$$

where θ_W is the Weinberg angle. By inverting this relation we can write W_μ^3 and B_μ as a function of A_μ and Z_μ . Replacing in Eq. 2.9 and imposing that the A_μ field has zero mass we can determine θ_W : $\tan \theta_W = \frac{g'}{g}$. The Lagrangian of Eq. 2.9 takes then the form

$$\mathcal{L} = \frac{1}{2} (v^2 g^2) (W_\mu^1 W^{1\mu} + W_\mu^2 W^{2\mu}) + \frac{1}{2} (v^2 [g^2 + g'^2]) Z_\mu Z^\mu + \dots , \quad (2.12)$$

500 where we show only the mass terms for the gauge bosons. Note that, by construction, there is no mass
 501 term for A_μ which allows us to identify this field with the photon. W_μ^1 and W_μ^2 are related to the W^\pm
 502 boson and Z_μ corresponds to the Z boson. We have shown that it is the fact that $v \neq 0$ that allows for
 503 the existence of non-zero mass terms for the W^\pm and Z bosons.

If we now expand the second term of the Higgs potential (Eq. 2.3) using Eq. 2.8 we get, among other terms,

$$\mathcal{L} = -h^3 \sqrt{-\mu^2 \lambda} - h^4 \lambda + \dots . \quad (2.13)$$

These terms encode the Higgs self interactions and represent, respectively, the three and four point interactions. We see that the coupling constants of these interactions depend on the parameters of the Higgs potential, μ^2 and λ .

In addition to being responsible for giving mass to the gauge bosons, the Higgs field is also responsible for the mass of the fermions. However, the mechanism through which this occurs is fundamentally different. In the case of fermions, the mass terms are placed explicitly in the Lagrangian:

$$\mathcal{L}_{\text{fermions}} = G_1 \bar{L} \phi R + G_2 \bar{L} \phi_c R + \text{hermitian conjugate} \quad (2.14)$$

where L denotes a left-handed fermion doublet and R denotes a right-handed fermion singlet. Here, left and right refer to helicity states. G_1 and G_2 are arbitrary coupling constants that can be written in terms of the fermion's mass and the VEV. ϕ is given by Eq. 2.8 and ϕ_c is given by (after the spontaneous symmetry breaking and in the unitary gauge):

$$\phi_c = \begin{bmatrix} v + \frac{h}{\sqrt{2}} \\ 0 \end{bmatrix}. \quad (2.15)$$

We now take a quick detour to motivate why fermions are represented as chiral states (left and right) of the $SU_L(2)$ symmetry. We base this discussion on Ref. [9]. In the context of the unification of the electromagnetic and weak forces, formalized by Weinberg, Glashow and Salam in 1961, both interactions are interpreted as manifestations of the electroweak force. Weak charged currents are axial vector currents which means they couple only to left handed fermions while weak neutral currents, as well as QED, couple to both helicity states. This suggested that fermions were better represented as left-handed doublets and right-handed singlets of the $SU_L(2)$ symmetry group. The left handed doublets, L , are defined as:

$$L : \begin{pmatrix} \nu_l \\ l \end{pmatrix}_L, \begin{pmatrix} u \\ d' \end{pmatrix}_L \quad (2.16)$$

where l represents an electron, muon or tau, u is any quark of the up type and d' is a quark of the down type. The right-handed states, R , are singlets, define as:

$$R : l_R, u_R, d'_R. \quad (2.17)$$

In 1956, C. S. Wu *et al.* showed that the weak interaction violates parity conservation [10]. In 1958, M. Goldhaber *et al.* conducted an experiment that showed that neutrinos are left-handed and anti-neutrinos are right-handed [11] which is why the SM does not include a right-handed state for neutrinos. We can now continue the discussion of the mass generation mechanism for fermions.

The first term in Eq. 2.14 gives mass to down type fermions (electron, muon, tau, down, strange

519 and bottom quarks) and the second to up type fermions (up, charm and top quarks). In addition, these
 520 terms give rise to the interaction terms between the Higgs field and the fermions. Take, as an example,
 521 $\bar{L} = (\bar{t}, \bar{b})_L$ and $R = b_R$. For the first term of Eq. 2.14 we get:

$$G_1 \bar{L} \phi R = G_1 (\bar{t}, \bar{b})_L \begin{bmatrix} 0 \\ v + \frac{h}{\sqrt{2}} \end{bmatrix} b_R = G_1 v \bar{b}_L b_R + \frac{G_1}{\sqrt{2}} \bar{b}_L b_R h. \quad (2.18)$$

The first term is the mass term for b quarks. Therefore we can redefine $G_1 v = m_b$ and obtain:

$$G_1 \bar{L} \phi R = m_b \bar{b}_L b_R + \frac{m_b}{v \sqrt{2}} \bar{b}_L b_R h. \quad (2.19)$$

522 The second term gives the interaction between the Higgs boson and the fermions, in this case, the b
 523 quarks. The strength of this interaction is directly proportional to the mass of the corresponding fermion.

524 In the SM formalism, neutrinos as massless particles. However, there is no reason why they cannot
 525 acquire mass through a mechanism similar to the one we just described. Nonetheless, the usual argu-
 526 ment is that it would be unnatural for the same mechanism to produce the mass of very heavy particles,
 527 such as the top quark, and the mass of very light particle, such as the neutrinos. Therefore, BSM models
 528 that try to explain the mass generation for neutrinos usually resort to a different mechanism.

529 The SM has delivered extremely accurate predictions about the existence and properties of new
 530 particles which make it a very successful theory. It predicted the existence of the W and Z bosons [12],
 531 the gluon, the charm and top quarks and the Higgs boson [6–8]. In addition, the SM prediction for the
 532 value of the anomalous magnetic dipole moment of the electron (calculated up to order α^5) agrees with
 533 the measured value up to the 11th decimal place, making it the most precise measurement in science.

534 2.1.1 Higgs pair production

535 Within the SM there are still some processes that have not been measured. One of these is the pro-
 536 duction of pairs of Higgs bosons. The experimental challenges and efforts related to this process are
 537 discussed in section 4.1. Here we provide a theoretical description of the process.

538 At the Large Hadron Collider (LHC), the main production process of Higgs pairs is gluon-gluon fusion
 539 (ggF). Higgs pairs can also be produced through vector boson (V) fusion (VBF), in association with a
 540 pair of top quarks ($t\bar{t}h$) or through Higgs strahlung (Vh) ⁴. At a center of mass (CM) energy of $\sqrt{s} = 13$
 541 TeV, the ggF production process has a cross section approximately seventeen times larger than the next
 542 most common production process which is VBF (approximately 30 fb *versus* 1.6 fb [13]). Therefore it
 543 is the dominant contribution when we study inclusive production. For this reason we focus the following
 544 discussion on this production mode. The leading order Feynman diagrams for Higgs pair production via
 545 ggF are shown in figure 2.3.

546 The diagram on the right has an off-shell (virtual) Higgs boson, h^* , that couples to gluons by the usual
 547 heavy quark triangle (same mechanism as in single Higgs production). h^* then decays to two on-shell
 548 Higgs bosons. This diagram contains the three point interaction between Higgs bosons and therefore it

⁴In this process, at LO, a Higgs boson is radiated from a vector boson

549 is the one that allows us to probe this coupling. In the diagram on the left, the two Higgs bosons couple
 550 to the gluons by a box of heavy quarks and are directly radiated from a quark. The largest contributions
 551 for these quantum loops come from heavy quarks, such as the top and bottom, because the coupling
 552 constant of the Higgs boson to fermions is directly proportional to the fermions mass (see section 2.1).

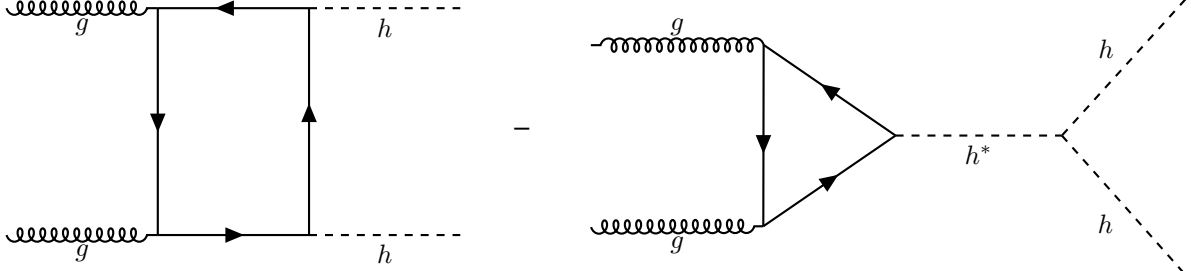


Figure 2.3: Feynman diagrams of Higgs pair production from gluon fusion. Triple vertex diagram (left) and box diagram (right). The minus sign between the diagrams indicates that they interfere destructively.

The amplitudes for the box, \mathcal{M}_\square , and triangle, \mathcal{M}_Δ , diagrams scale as [14]:

$$\mathcal{M}_\square \sim \frac{\alpha_s}{4\pi} y_t^2, \quad \mathcal{M}_\Delta \sim \lambda_{hhh} \frac{\alpha_s}{4\pi} y_t^2 \frac{m_h^2}{\hat{s}} \left(\log \frac{m_t^2}{\hat{s}} + i\pi \right)^2 \quad (2.20)$$

553 where \hat{s} is the CM energy, y_t is the Yukawa coupling of the top quark, α_s is the electroweak coupling
 554 constant, λ_{hhh} is the coupling constant of the Higgs boson three point self-interaction and m_h, m_t are
 555 the masses of the Higgs boson and top quark.

556 At a CM energy of $\sqrt{s} = 13$ TeV the cross section for Higgs pair production, as predicted by NLO
 557 calculations, is very small, approximately 30 fb [13]. It is suppressed due to the destructive interference
 558 between the LO diagrams that leads to a $\sim 50\%$ suppression of the total cross section [14]. Furthermore,
 559 the cross section of the triangle diagram is smaller than the one of the box diagram, approximately 4 fb
 560 compared to 30 fb⁵, and it is strongly suppressed for larger values of the CM energy which can be seen
 561 directly from the expression of the amplitude in Eq. 2.20. This means that the Higgs trilinear coupling
 562 mostly affects the Higgs pair production at threshold. A variable that is sensitive to these effects is the
 563 invariant mass of the Higgs pair. The tail of this distribution (high invariant mass of the Higgs pair),
 564 however, is mostly determined by the box diagram contribution [14].

The LO calculation for the cross section of Higgs pair production has been performed, for example, in Ref. [15]. A value of the order of 10 fb is reported. The NLO calculation is a theoretical challenge: several two-loop diagrams that take into account virtual and real radiation have to be considered. In addition, top quark mass effects can be included in various approximations. This leads to corrections with different signs which suggests that the uncertainty on the cross section due to top quark mass effects are of the order of $\pm 10\%$ at NLO. Therefore, a calculation including the full top mass dependence was of the utmost importance. This result became available recently [16]:

$$\sigma_{gg \rightarrow hh}^{\text{NLO}} = 27.80^{+13.8\%}_{-12.8\%} (\text{scale}) \pm 0.3\% (\text{stat.}) \pm 0.1\% (\text{int.}) \text{ fb} \quad (2.21)$$

⁵These values are obtained using MadGraph5. They are shown here to give a rough estimate of the difference between the values of the cross sections of both diagrams.

565 where the dependence of the result on the variation of the scales by a factor of two around the central
 566 scale, the statistical error coming from the limited number of phase space points evaluated and the error
 567 coming from the numerical integration of the amplitude are shown.

568 This result shows that the introduction of NLO contributions produces a significantly different result.
 569 Therefore the inclusion of such effects is necessary if we wish to obtain an accurate result that can be
 570 compared to experimental values. The analytical expressions for the NLO cross section are long and
 571 complex so we abstain from reproducing them here. Nonetheless, the LO cross section can be written in
 572 a compact form and it allows us to discuss some key features of the process. Therefore, we will present
 573 it here, based on Refs. [15, 17].

The partonic LO cross section for $gg \rightarrow hh$ can be written

$$\hat{\sigma}_{gg \rightarrow hh}^{\text{LO}}(\hat{s}) \sim \int_{\hat{t}_-}^{\hat{t}_+} d\hat{t} \left(|C_\Delta F_\Delta + C_\square F_\square|^2 + |C_\square G_\square|^2 \right) \quad (2.22)$$

where \hat{s} and \hat{t} are the Mandelstam variables and, in addition, \hat{s} can be identified with the square of the partonic CM energy of the process. The integration limits, \hat{t}_\pm , are derived from a momentum parametrization in the CM frame, leading to $\hat{t}_\pm = m_h^2 - \frac{\hat{s}}{2}(1 \mp \beta_h)$, where $\beta_h^2 = 1 - 4\frac{m_h^2}{\hat{s}}$ and m_h is the mass of the Higgs boson [17]. F_Δ , F_\square and G_\square are form factors whose full expressions can be found, for example, in Ref. [15]. C_Δ and C_\square can be interpreted as generalized couplings and are given by

$$C_\Delta = \lambda_{hhh} \frac{m_Z^2}{\hat{s} - m_h^2}, \quad C_\square = 1, \quad (2.23)$$

where m_Z is the mass of the Z boson. If we take the limit $m_Q^2 \gg \hat{s} \sim m_h^2$ (where m_Q is the mass of the quarks that contribute to the quantum loops) we can get simple expressions for the remaining form factors:

$$F_\Delta = \frac{2}{3} + \mathcal{O}(\hat{s}/m_Q^2), \quad F_\square = -\frac{2}{3} + \mathcal{O}(\hat{s}/m_Q^2), \quad G_\square = \mathcal{O}(\hat{s}/m_Q^2). \quad (2.24)$$

In this limit, the partonic cross section is simply given by

$$\hat{\sigma}_{gg \rightarrow hh}^{\text{LO}}(\hat{s}) \sim \int_{\hat{t}_-}^{\hat{t}_+} d\hat{t} \left| \lambda_{hhh} \frac{m_Z^2}{\hat{s} - m_h^2} - 1 \right|^2. \quad (2.25)$$

574 There are two important points that are worth discussing. Firstly, the total cross section has terms
 575 that are proportional to the Higgs triple coupling, λ_{hhh} , which can be read directly from Eq. 2.25. On the
 576 one hand, this means that measuring this process gives us access to the value of λ_{hhh} and therefore
 577 provides valuable insight into the shape of the Higgs potential and ultimately into the EWSB mechanism
 578 in the SM. On the other hand, if λ_{hhh} has a value that is different from the one predicted by the SM, that
 579 will affect the measured value of the cross section and can lead to hints of new physics.

580 Secondly, although this is not evident from Eq. 2.25, the cross section for di-Higgs production in-
 581 creases with \hat{s} . This can be seen in figure 2.4 that shows the variation of the total (integrated) NLO cross
 582 section with the CM energy for the six largest production channels. Note that increasing the CM energy
 583 from 13 to 100 TeV increases the inclusive cross section by approximately two orders of magnitude which

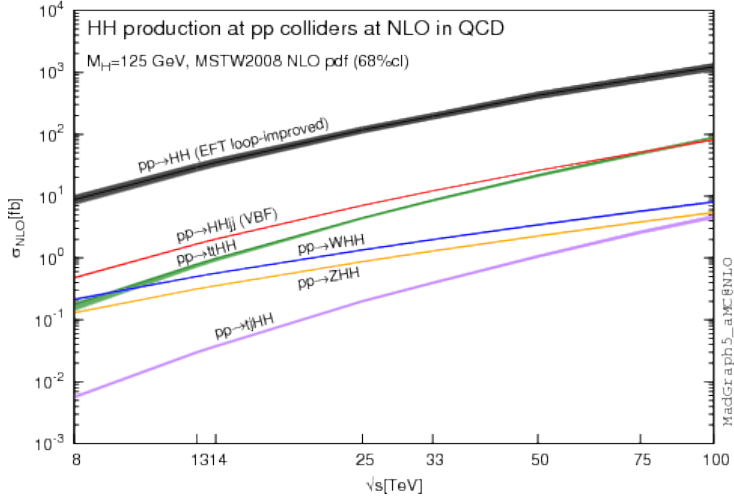


Figure 2.4: Total cross sections at NLO in QCD for the six largest HH production channels at pp colliders. The thickness of the lines corresponds to the scale and PDF uncertainties added linearly.

584 is a consequence of the increased phase space that becomes available.

585 Therefore, the increase in the cross section of rare processes, such as Higgs pairs production, as
586 the CM energy of collision experiments increases supports the claim that future colliders, with higher
587 CM energies, might be our chance of discovering and precisely studying these processes.

588 2.2 Going beyond

589 Despite the success of the SM, there is evidence that indicates that it cannot be the final theory of
590 particle physics. This led to the development of alternative models that extend the SM but that can
591 still reproduce its successful predictions. These are referred to as Beyond the Standard Model (BSM)
592 models.

593 On the one hand, there are several pieces of experimental evidence that the SM cannot explain.
594 These include the nature of dark matter, postulated to explain the experimental observations of the
595 velocity of far away galaxies [18], the asymmetry between matter and anti-matter in the present Universe
596 ⁶ and the fact that neutrinos oscillate between flavors which implies that they have a non-zero mass.
597 This phenomenon was measured independently by two collaborations, the Super-Kamiokande and the
598 Sudbury Neutrino Observatory (SNO), in 1998 and 2001-2002, respectively, [19–21].

599 On the other hand, its theoretical formulation also has some weaknesses: it accurately describes
600 particles interactions at the electroweak scale (~ 246 GeV) but it does not include gravity which means it
601 cannot be valid at the Planck scale ($\sim 10^{19}$ GeV) where gravity cannot be overlooked; it has a lot (over 20)
602 of free parameters whose values have to be tuned to fit experimental observations, and there is a large
603 discrepancy between the mass scales associated with the electroweak and gravitational interactions
604 (this is one of the simplest formulations of what is known as the hierarchy problem).

605 When faced with these weaknesses, or rather hints of incompleteness, the theoretical community
606 put a great effort into the development of models that add new ingredients to the SM. In the following

⁶Or why do we live in a local in an Universe made mostly out of matter?

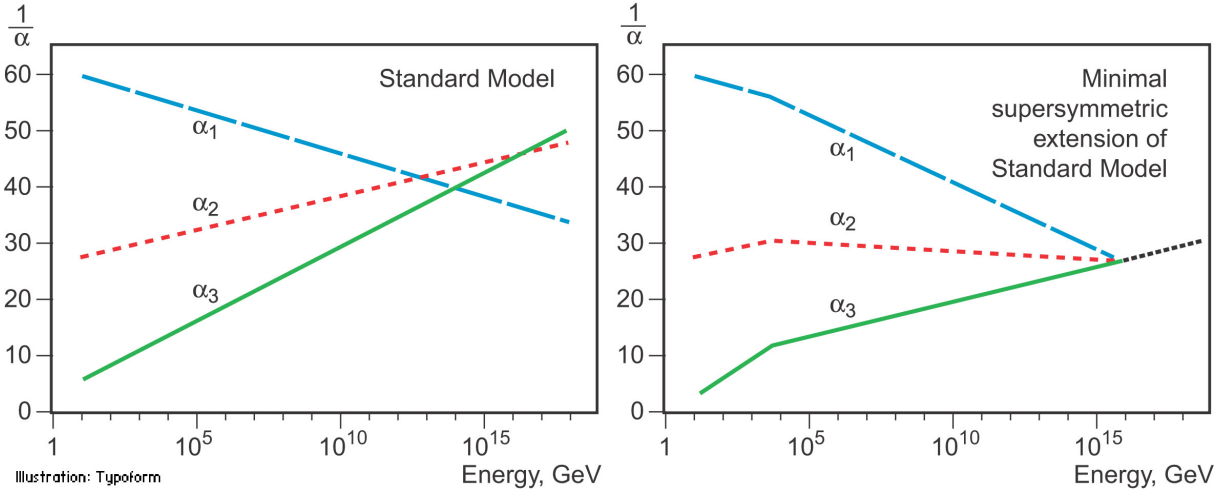


Figure 2.5: Here, α_1 , α_2 and α_3 represent the coupling constants of $U_Y(1)$, $SU_L(2)$ and $SU_{color}(3)$, respectively. What is shown is the variation of the inverse of the coupling with the energy: on the left for the SM and on the right for the MSSM. Plots from Ref. [23].

paragraphs we introduce and briefly describe some of the most well studied (both theoretically and experimentally) BSM models. We follow the discussion presented in Ref. [22] as a starting point.

It is a well known consequence of renormalization in QFT that the coupling constants become dependent on the energy scale at which the theory is probed. As the energy scale increases the $U_Y(1)$ coupling constant gets larger while the $SU_L(2)$ and $SU_{color}(3)$ coupling constants get smaller. If one extrapolates far enough these become nearly equal at an energy scale of approximately 10^{15} GeV. Although this matching is far from perfect, it sparked the idea that these three forces could be unified at an energy scale of 10^{15} GeV. Grand Unification Theories (GUT) try to combine $SU_{color}(3) \times SU_L(2) \times U_Y(1)$ into a larger symmetry group.

Supersymmetric (SUSY) models introduce a new symmetry that links fermions and bosons. For each boson(fermion) of the SM it introduces a fermionic(bosonic) partner. Apart from spin, the supersymmetric partners would share the same mass and quantum numbers. Since we have not found any supersymmetric particles in the LHC this means that supersymmetry is necessarily a broken symmetry and, if they exist, new particles should have a larger mass (outside of the present reach of the LHC) than their SM partners. SUSY models were introduced because they offer a natural fix for the hierarchy problem. In addition, the Minimal Supersymmetric extension of the SM (MSSM) also leads to a better convergence of the coupling constants as can be seen in figure 2.5. From the standpoint of GUT this is extremely appealing.

An early proposal of a theory that could unify gravity with electromagnetism was given by Theodore Kaluza in 1921. In particular, he showed that these two forces could stem from a single tensor with the introduction of an extra space dimension. In 1926, Oscar Klein offered an explanation for this extra dimension; he proposed that it had a circular topology such that at each point of the four dimensional space-time we would have a circle with a small radius. This theory has more degrees of freedom (because it is formulated in a higher dimensional space-time) and therefore it predicts new particles that are usually known as Kaluza-Klein gravitons (and their excited states). Nonetheless, the Kaluza-Klein

model does not provide a satisfactory explanation for the hierarchy problem. Therefore, in 1999, Lisa Randall and Raman Sundrum introduced a new model that does. This model introduces only two new particles: a spin 2 graviton (and its Kaluza-Klein excitations) and a radion, that is a spin 0 neutral particle.

Models with two Higgs doublets (2HDM) are one of the simplest possible extensions of the Higgs sector of the SM. They are appealing because while the fermionic sector is rather complex, having three families, the scalar sector is quite simple, having a single particle, which seems unnatural. This type of structure is realized in various new physics models including SUSY models. In addition, they provide an additional source for CP violation which could help explain the matter-anti-matter asymmetry in the Universe.

The most general renormalizable 2HDM scalar potential is written as [24]

$$\begin{aligned} V = & m_{11}^2 |\Phi_1|^2 + m_{22}^2 |\Phi_2|^2 - (m_{12}^2 \Phi_1^\dagger \Phi_2 + h.c.) \\ & + \frac{1}{2} \lambda_1 |\Phi_1|^4 + \frac{1}{2} \lambda_2 |\Phi_2|^4 + \lambda_3 |\Phi_1|^2 |\Phi_2|^2 + \lambda_4 |\Phi_1^\dagger \Phi_2|^2 \\ & + \left[\frac{1}{2} \lambda_5 (\Phi_1^\dagger \Phi_2)^2 + \lambda_6 |\Phi_1|^2 (\Phi_1^\dagger \Phi_2)^2 + \lambda_7 |\Phi_2|^2 (\Phi_1^\dagger \Phi_2)^2 + h.c. \right], \end{aligned} \quad (2.26)$$

where Φ_1 and Φ_2 are hypercharge doublets and the coefficients m_{12}^2 and $\lambda_{5,6,7}$ can be complex. However, when including the Yukawa interactions, the most general lagrangian leads to tree-level flavor changing neutral currents (FCNC) in the Yukawa sector. These FCNC are very tightly constrained by experimental data and should be avoided. They can be eliminated by imposing a \mathbb{Z}_2 symmetry. Although, usually, this symmetry is allowed to be softly broken in order to allow the theory to have a decoupling limit [25] where the mass of all the scalars other than the SM-like one can be made very large. In addition to the softly-broken \mathbb{Z}_2 symmetry, which leads to $\lambda_{6,7} = 0$, we also impose CP conservation which makes all possible complex phases vanish. In this case, we obtain five Higgs bosons that are CP eigenstates. Three of them are neutral, h , H and A , and the other two are charged, H^\pm . h and H are CP-even states while A is CP-odd. h is usually taken to be the SM Higgs boson and its mass is set to 125 GeV.

There are several types of 2HDM classified according to their fermion-scalar interactions. We highlight the type II (the one used in this work), where all right-handed up-type quarks couple to Φ_2 and right-handed down-type quarks and charged leptons couple to Φ_1 . This type of couplings is analogous to what happens in SUSY models.

Instead of the parameters in Eq. 2.26, we can describe the model in terms of the four physical masses, m_h , m_H , m_A and m_{H^\pm} , the angles α and β , the VEV $v = 246$ GeV and a further parameter, chosen to be m_{12}^2 [24]. The angle β is defined as $\tan(\beta) = v_2/v_1$, where $v_{1,2}$ are the VEVs of the two Higgs doublets. The angle α diagonalizes the square mass matrix of the CP-even states. The quartic couplings of the potential can then be written in terms of these parameters, as can be found in Eq. 11 of Ref. [24].

Simplified dark matter (DM) models are based on the exchange of a single particle between DM and SM particles and try to explain the nature of DM and how it interacts with the SM. The particle exchanged is called a mediator and, depending on the specific model, it can be neutral or electrically charged and have spin 0, 1 or 2. The simplest possible scenario is a neutral scalar mediator.

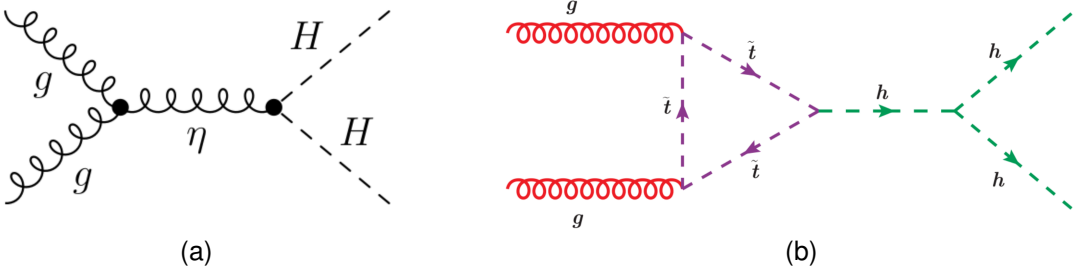


Figure 2.6: BSM contributions to Higgs pair production from the spin-2 Kaluza-Klein graviton (a) and from the SUSY partner of the top quark (b). Figures from Refs. [26, 27], respectively.

665 The CP-conserving 2HDM and dark matter model with a spin 0 mediator are explored in this work
 666 as sources of alternative di-Higgs production processes. For these models, the main modification with
 667 respect to the SM occurs because new heavy particles, namely, H and the DM mediator can couple
 668 to the Higgs bosons through the s-channel diagram. This corresponds to replacing the off-shell Higgs
 669 boson by one of these particles in the Feynman diagram on the right in figure 2.3.

670 The spin-2 graviton predicted by Kaluza-Klein and Randal-Sundrum models can couple directly to
 671 gluons and then decay producing a Higgs pair, as it illustrated in figure 2.6(a). SUSY particles can
 672 contribute to the quantum loops in the Higgs production Feynmann diagrams. An example is shown in
 673 figure 2.6(b), where the top quark is replaced by its supersymmetric partner is the s-channel diagram.
 674 These are two other examples of how BSM models can change the Higgs pair production process with
 675 respect to the SM.

676 The crucial point is that some BSM contributions can lead to an enhancement of the cross section
 677 for Higgs pair production with respect to what is predicted by the SM. Experimentally, this means that
 678 we would not need as much sensitivity and therefore the process could be measured with less data and
 679 therefore sooner. This is the reason why a lot of the searches performed at the LHC focus on this type
 680 of scenario. In addtion, if a new heavy particle couples to the Higgs boson via an s-channel diagram, it
 681 could lead to the existence of a peak in the Higgs pair invariant mass spectrum (assuming that we have
 682 enough experimental resolution and that there are not other processes coming into play).

683 Moreover, BSM models introduce new free parameters (in addition to the SM ones) that can be
 684 constrained using the experimental results obtained at the LHC (and other experiments). This reduces
 685 the available parameter space of the models and may even reject some of them.

686 Chapter 3

687 Collider experiments

688 In this chapter we start by providing an overview of the goals and main challenges of modern collider
689 experiments. The definitions of some key quantities that describe an accelerator are introduced and a
690 brief discussion on how they influence the discovery potential of an accelerator is presented.

691 In section 3.2 we introduce the LHC and in section 3.2.1 we describe the ATLAS experiment, includ-
692 ing brief discussions on b-tagging, trigger and data acquisition algorithms and systems. In section 3.3
693 we introduce the concept of a hadronic jet and describe how these objects are reconstructed in a general
694 collider experiment. Jet properties and substructure observables, as well as jet grooming algorithms,
695 are introduced in sections 3.3.1 and 3.3.2, respectively.

696 In section 3.4 we shift the focus to future collider experiments and accelerators and motivate their
697 need. In sections 3.4.1 and 3.4.2 we introduce the hadronic Future Circular Collider (FCC-hh) and
698 describe the baseline detector design.

699 Collider experiments are the best tool we have to explore matters' most fundamental structure. When
700 we accelerate a particle we increase its momentum. If we take into account the wave particle duality
701 and the De Broglie expression, $\lambda = h/p$, where λ is the wavelength and p is the particle's momentum,
702 we can see that a particle with a large p will have a small λ . The wavelength gives us the dimension
703 scale of the objects we can probe with a given wave. If we want to probe very small particles (subatomic
704 and smaller) we need very small λ and therefore very large p . Conceptually, this is the basic idea behind
705 modern particle accelerators.

706 In practice, charged particles can be accelerated and their trajectories controlled by means of electro-
707 magnetic fields. However, this is not without numerous technical challenges. When a charged particle is
708 subject to an acceleration perpendicular to its velocity (which is exactly what happens in circular acceler-
709 ators) it emits electromagnetic radiation, called synchrotron radiation. The power emitted is proportional
710 to the fourth power of the particle's energy and inversely proportional to the radius squared and to the
711 fourth power of the particle's mass. This radiation limits the maximum energy that can be achieved in
712 electron-positron colliders. In proton-proton colliders, however, the energy is limited by the maximum
713 magnetic field that can be achieved. Therefore, there is also the need for extremely powerful magnets
714 which are usually implemented using technology based in superconductivity. Using superconducting

715 magnets raises another challenge: they can only operate at very low temperatures, close to the ab-
716 solute zero. In addition, in order to sustain a stable beam it is necessary that the beam pipe has an
717 environment very close to absolute vacuum.

718 3.1 Experimental aspects

One of the most important parameters of a particle accelerator is the time integrated luminosity, $\int \mathcal{L}(t)dt$. For a given process with cross section σ , it determines the number of event that will be produced, N :

$$N = \sigma \int \mathcal{L}(t)dt, \quad (3.1)$$

where $\mathcal{L}(t)$ is the instantaneous luminosity that is a measure of the number of collisions per bunch crossing. The instantaneous luminosity is given by:

$$\mathcal{L} = f_{coll} \frac{n_1 n_2}{4\pi \sigma_x \sigma_y}, \quad (3.2)$$

719 where f_{coll} is the collision frequency, n_1 and n_2 are the number of protons in each bunch and σ_x and σ_y
720 characterize the transverse beam size in the horizontal and vertical directions.

721 To increase the chances of measuring a rare process, or to increase the statistical significance of the
722 measurement of an already discovered process, we want to increase N as much as possible. To do so
723 we can either increase the integrated luminosity or change the CM energy in order to increase the cross
724 section of the process.

725 While the cross sections of most physics processes increase when the CM energy varies from 13 to
726 100 TeV, many BSM models predict new processes, or new contributions to existing processes, whose
727 cross sections increase more rapidly than the SM backgrounds. In addition, by conservation of energy,
728 a larger CM energy implies that particles with larger mass can be created. We can tune the parameters
729 of Eq. 3.2 to obtain the highest possible luminosity. Nonetheless, because we are dealing with charged
730 particles, there is a limit on how close the bunches can be and on how many protons we can pack in
731 a bunch. Moreover, the beam's transverse dimensions cannot be infinitely reduced. A smarter way to
732 increase the number of collisions that an accelerator can produce is to run for a longer time, therefore
733 increasing the integration time in Eq. 3.1.

734 In conclusion, the CM energy and the integrated luminosity are two of the main parameters that drive
735 the discovery potential of an accelerator.

736 3.2 The Large Hadron Collider

737 The Large Hadron Collider (LHC) is the world's largest and most powerful particle accelerator. It is
738 housed by the European Organization for Nuclear Research (CERN) which focuses on fundamental
739 particle physics with the goal of probing matter's most elementary structure. Ever since its creation, in

740 1954, CERN has housed many accelerators and experiments and played a key role in the development
741 of fundamental and applied science.

742 The LHC consists of a 27-kilometer ring located beneath the Franco-Swiss border, near Geneva.
743 Most of its running time is dedicated to accelerating protons in opposite directions up to a maximum
744 center of mass energy of $\sqrt{s} = 13$ TeV and colliding them at the center of the two general purpose
745 experiments, ATLAS (described in section 3.2.1) and CMS. The LHCb experiment also records data
746 from proton-proton collisions but it is dedicated to the study of beauty particles. The ALICE experiment
747 is optimized to study heavy-ion collisions at a CM energy of 2.76 TeV per nucleon.

748 The acceleration of charged particles at the LHC is based on radio frequency (RF) cavities. These
749 cavities are shaped to sustain a resonant electromagnetic field that oscillates at a frequency of 400 MHz.
750 During the acceleration stage, charged particles passing through the cavities feel an overall force that
751 propels them forward. When the LHC is running at full energy, a perfectly timed proton with exactly the
752 right energy feels a zero net force when passing the cavities. Protons with a slightly different energies
753 arriving slightly earlier or later are decelerated or accelerated in order to keep the beam sorted in discrete
754 packages with the same energy. These are called bunches. There are 2808 bunches circulating at the
755 same time, each containing approximately 10^{11} protons. The bunches are spaced by 25 ns. Furthermore,
756 the successful operation of the LHC also relies on superconducting magnets made of Niobium-Titanium
757 filaments chilled to -271.3° C and on an ultra high vacuum (of the order of $10^{-10} - 10^{-11}$ mbar) inside
758 the beam pipes. The magnets are placed along the LHC ring and produce dipole and quadrupole
759 electromagnetic fields. The dipole magnets create a nominal field of 8.3 T and bend the beam along the
760 tunnel. The quadrupole magnets focus the beam at the interaction points. The ultra high vacuum greatly
761 reduces the probability that the beam interacts with any particle. It is crucial to keep a stable beam to
762 continuously maintain collisions during long runs.

763 One of the main research goals of the LHC was to discover the Higgs boson. This was achieved
764 in 2012 when ATLAS and CMS reported the discovery of a particle consistent with the boson predicted
765 by the Higgs mechanism, with a mass of 125 GeV [28, 29]. Ever since, efforts have been directed
766 to measuring its mass, couplings, spin-parity properties with increasing precision using different decay
767 channels and production modes.

768 ATLAS and CMS reported the observation (measurement with a significance greater than five sigma)
769 of the Higgs decaying to $b\bar{b}$ [30, 31]. The searches targeted the VH production mode. It offers the
770 best sensitivity to the $hb\bar{b}$ Yukawa coupling because requiring a vector boson helps reduce the SM
771 backgrounds, namely the ones from QCD interactions. The observation of $h \rightarrow b\bar{b}$ means we have
772 now observed most of the Higgs boson's decay modes predicted by the SM. CMS reported the first
773 observation of the Higgs boson decaying to a pair of tau leptons [32]. In addition, the observation of
774 Higgs boson production in association with a $t\bar{t}$ pair was very recently reported by both collaborations
775 [33, 34]. Moreover, precision measurements of the masses of the Higgs [35, 36] and W [37] bosons and
776 of the top quark [38, 39] were also performed. So far, no conclusive signs of new physics were seen at
777 the LHC.

778 Future prospects for the LHC include its upgrade to the High Luminosity-LHC (HL-LHC) after the

779 scheduled long shutdown of 2024-2026. This upgrade will increase the size of the dataset to 3000 fb^{-1}
780 over the course of ten years [40]. During the shutdown, the ATLAS detector will be upgraded.

781 In the Higgs sector, the high value of the integrated luminosity will improve the statistical precision of
782 already measured channels and the discovery potential of rare processes [41].

783 3.2.1 The ATLAS detector

784 The ATLAS detector has a cylindrical geometry and a multi layered structure. Its dimensions are 25
785 meters in height (diameter) and 44 meters in length and it weights approximately 7000 tonnes. In the fol-
786 lowing paragraphs we describe the detector's layers and their functionalities. A schematic representation
787 of the detector as well as the appropriate coordinate system can be found in figure 3.1.

788 A combination of cartesian and cylindrical coordinates is used to describe the detector. In both
789 cases, the origin is defined to coincide with the interaction point. The Cartesian system is right-handed
790 and the z axis is defined to be the direction of the beam. The x-axis points from the interaction point
791 to the center of the LHC ring and the y-axis points upwards. The azimuthal angle, ϕ , is measured
792 around the beam axis and the polar angle, θ , from the beam line. The pseudorapidity is defined as
793 $\eta = -\ln \tan(\theta/2)$. Another commonly used quantity is the rapidity, y , defined as a function of a particle's
794 energy, E , and longitudinal momentum, p_L : $y = \frac{1}{2} \ln \left(\frac{E+p_L}{E-p_L} \right)$. In the limit where a particle's mass is
795 negligible with respect to its momentum the pseudorapidity converges to the definition of rapidity. In
796 addition, the angular distance between two points, ΔR , is defined as $\Delta R = \sqrt{(\Delta\phi)^2 + (\Delta\eta)^2}$, where
797 rapidity can also be used instead of the pseudorapidity.

798 The detector consists of an inner detector (ID) or tracker, electromagnetic (EM) and hadronic calorime-
799 ters (ECAL and HCAL, respectively) and a muon spectrometer (MS). The magnet configuration consists
800 of a thin superconducting solenoid that surrounds the ID cavity and three superconducting toroids (one
801 barrel and two end-caps) arranged with an eight-fold azimuthal symmetry around the calorimeters.

802 The ID covers the pseudorapidity range $|\eta| < 2.5$ and it makes up the innermost layer of the detector.
803 It consists of silicon pixel, silicon micro-strip, and straw tube transition radiation tracking detectors. It is
804 contained in a solenoid magnet with a central field of 2 T. The tracker provides precision measurements
805 of the positions and momenta of charged particles. As a charged particle transverses the several layers
806 of the ID it ionizes the medium creating electrical signals that can be read out. These individual electrical
807 signals are then combined to reconstruct the trajectory of the particle.

808 Lead/Liquid-Argon (LAr) sampling EM calorimeters cover the pseudorapidity range $|\eta| < 3.2$. The
809 EM calorimeter has an accordion like structure with layers of showering material (lead) interleaved with
810 layers of active material (liquid argon). These calorimeters provide measurements of the energy of
811 electrons and photons. The interaction of these particles with the lead layers induces the production
812 of an EM shower whose energy is measured in the liquid argon layers. The granularity of the EM
813 calorimeter strongly depends on the longitudinal layer and on the pseudorapidity region.

814 The hadronic calorimetry in the pseudorapidity range $|\eta| < 1.7$ is provided by a scintillator-tile
815 calorimeter (TileCal) which is divided in a central barrel and two smaller end-cap barrels, one on each

Table 3.1: ATLAS tile and liquid argon hadronic calorimeters: summary of the pseudorapidity coverages and transversal segmentation (granularity).

TileCal	Barrel	Extended barrel
Coverage	$ \eta < 1.0$	$0.8 < \eta < 1.7$
Granularity	0.1×0.1	0.1×0.1
LAr calorimeter	End-cap	Forward
Coverage	$1.5 < \eta < 3.2$	$3.2 < \eta < 4.9$
Granularity	0.1×0.1 for $1.5 < \eta < 2.5$ 0.2×0.2 for $2.5 < \eta < 3.2$	0.2×0.2

816 side of the central barrel. The active components are scintillator tiles made of polystyrene that are in-
 817 terleaved with steel plates as the passive material. The scintillation light emitted by the tiles when an
 818 ionising particle crosses the calorimeter is collected on both ends of the tiles by wavelength-shifting op-
 819 tical fibers. The light signal emitted is proportional to the particle's energy. The TileCal is composed of
 820 several cells with transverse segmentation $\Delta\eta \times \Delta\phi = 0.1 \times 0.1$ ¹ [42].

821 For $|\eta| > 1.5$ LAr hadronic calorimeters extend the pseudorapidity range to $|\eta| = 4.9$. The LAr
 822 calorimeter is divided in end-cap and forward. These cover the pseudorapidity ranges $1.5 < |\eta| < 3.2$
 823 and $3.2 < |\eta| < 4.9$, respectively. The active material is liquid-argon and the absorbers are copper and
 824 tungsten for the end-cap and forward calorimeters, respectively. In the end-cap LAr calorimeters the
 825 segmentation is $\Delta\eta \times \Delta\phi = 0.1 \times 0.1$ for $1.5 < |\eta| < 2.5$ and 0.2×0.2 for $2.5 < |\eta| < 3.2$. In the forward
 826 LAr calorimeter the segmentation is $\Delta\eta \times \Delta\phi = 0.2 \times 0.2$.

827 The granularity of the ATLAS hadronic calorimeters is summarized in table 3.1. The hadronic
 828 calorimeters provide measurements of the energy of hadrons and jets; these allow the estimation of
 829 the missing transverse energy (E_T^{miss}). Approximately one third of the energy of jets is deposited in
 830 this layer. In the TileCal, the jet energy resolution is given by $\sigma/E \sim 50\%/\sqrt{E} + 3\%$ [42], where the
 831 first term is the stochastic term that derives from sampling fluctuations and follows a Poisson distribution
 832 and the second term is a constant that depends on the characteristics of the calorimeter. For the LAr
 833 calorimeter, the jet energy resolution is given by $\sigma/E \sim 60\%/\sqrt{E} + 2\%$ [43].

834 The MS is the outermost layer of the detector and it is dedicated to detecting muons that travel
 835 through the previous layers almost without interacting. This layer provides measurements of the muons
 836 momenta. It is composed of Monitored Drift Tubes (MDT) and Cathode Strip Chambers (CSC) that pro-
 837 vide high precision measurements of the muons' momentum in the pseudorapidity range $|\eta| < 2.7$ and
 838 of Resistive Plate Chambers (RPC) and Thin Gap Chambers (TGC) dedicated to triggering purposes
 839 for $|\eta| < 2.4$.

¹The TileCal is composed of three longitudinal layers. Only the first two have a segmentation equal to 0.1×0.1 . In the third layer the segmentation is 0.2×0.1 . However, most of the energy of hadronic showers is deposited in the first layers and therefore this detail is not very relevant for this work.

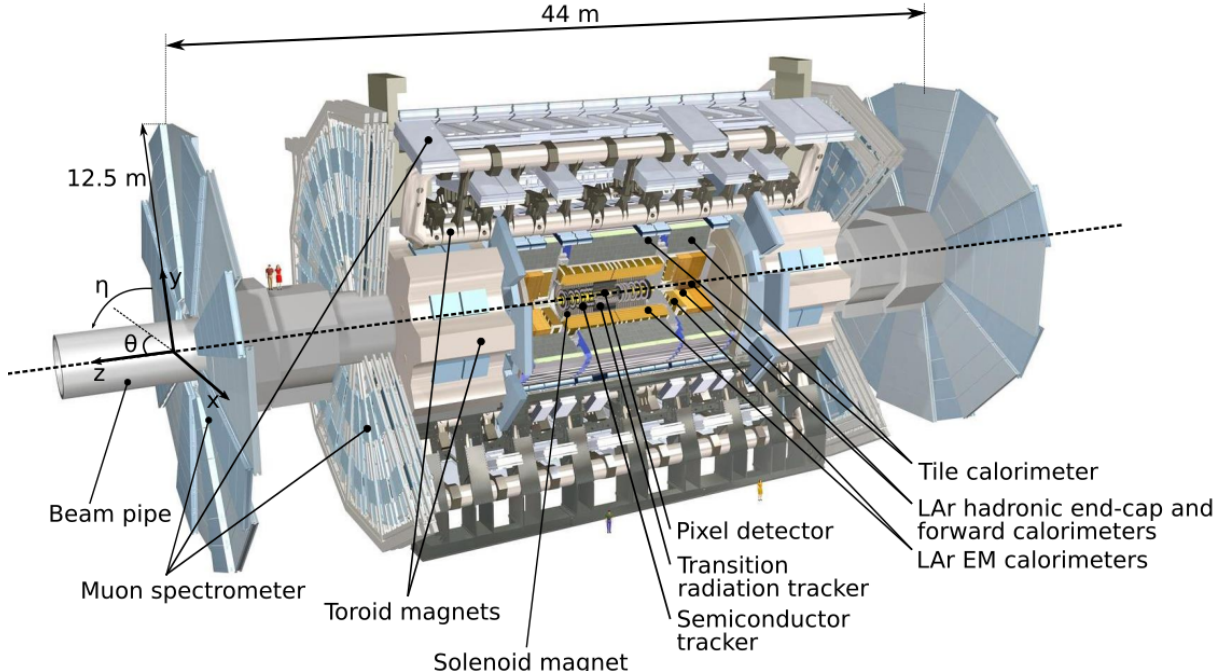


Figure 3.1: ATLAS detector.

840 **b-Tagging**

841 Each collision produces a large number of hadronic jets (we refer to section 3.3 for a detailed description
 842 of jets and how they are reconstructed). For this work, jets initiated by a b quark (b jets) are particularly
 843 important: we are looking for a Higgs pair decaying to four b quarks which leads to an experimental
 844 signature that consists of four b jets. b-Tagging algorithms determine, with a given probability, if a jet
 845 was originated by a b quark.

846 When a b quark is produced it hadronizes almost instantly, producing a B hadron. B hadrons have
 847 a lifetime of ~ 1 ps and can be highly relativistic meaning that they can travel a few millimeters to a few
 848 centimeters inside the inner detector before decaying. When they decay there is often a reconstructible
 849 secondary vertex that is slightly displaced from the primary vertex where the b-quark was produced.
 850 The existence of a secondary vertex is used by b-tagging algorithms to identify, or tag, a jet as coming
 851 from a b-quark. It is important to note that a complete b-tagging algorithm relies on the reconstruction of
 852 a secondary vertex which can only be done using the information from the inner detector. This implies
 853 that, in ATLAS, we can only b-tag jets that are produced in the region $|\eta| < 2.5$.

854 In ATLAS, b-tagging algorithms are applied to the sub-set of tracks that are associated with a given
 855 jet. The matching between tracks and calorimeter-based jets is performed using the ghost association
 856 technique [44]². The identification of b-jets in ATLAS is based on distinct strategies encoded on three
 857 b-tagging algorithms: impact parameter-based algorithms, an inclusive secondary vertex reconstruction
 858 algorithm and a decay chain multi-vertex reconstruction algorithm. The output of these algorithms are

²This procedure works by introducing ghost versions of the measured tracks that have the same direction but infinitesimally small p_T such that they do not modify the properties of the calorimeter jets. The jets are then reclustered and a track is considered to be associated with a given jet if its ghost version is contained in the jet after reclustering.

859 combined in a multivariate discriminant based on a Boosted Decision Tree (BDT) which provides the
860 best discrimination between the different jet flavors [45].

861 The impact parameter-based algorithms [46], IP2D and IP3D, use as discriminant variables the trans-
862 verse impact parameter significance and the transverse and longitudinal impact parameter significance,
863 respectively. The secondary vertex finding algorithm [46], SV, explicitly reconstructs a displaced sec-
864 ondary vertex inside the jet by trying to find pairs of tracks with a common origin. The decay chain
865 multi-vertex reconstruction algorithm [47], JetFitter, tries to reconstruct the full b-hadron decay chain.
866 This approach allows to resolve b- and c-hadrons vertices even if there are not two tracks associated
867 with them.

868 **Trigger and data acquisition**

869 The LHC delivers approximately 1000 million proton-proton collisions per second, which corresponds to
870 an event rate of 1 GHz. On the one hand, only a small fraction of these events result in interesting physics
871 processes. On the other hand, the detector does not have enough storage or read out capabilities to
872 record all the collisions. The triggering and data acquisition systems are responsible for selecting a
873 manageable rate of events for permanent storage and further analysis.

874 The trigger is responsible for selecting events with interesting experimental signatures. The trigger
875 system in Run-2 consists of a hardware-based first level trigger (Level-1) and a software-based high
876 level trigger (HLT). The Level-1 trigger takes as input coarse granularity calorimeter and muon detector
877 information and reduces the event rate to 100 kHz. The HLT uses full granularity detector information
878 and reduces the rate to approximately 1 kHz [48].

879 **3.3 Jet reconstruction**

880 A jet is a collimated spray of hadrons that is interpreted as coming from a single initial parton such
881 that approximately retains information about its physical properties, namely 3-momentum, mass and
882 charge. The existence of such objects is a direct consequence of the confinement property of QCD.
883 Quarks and gluons, the fundamental degrees of freedom of QCD, are not asymptotically free. They are
884 confined inside hadrons. Therefore, when one of these particles is produced it undergoes showering
885 and hadronization processes that lead to the formation of hadrons.

886 At a particle detector we are interested in reconstructing jets. These are the objects that are used in
887 physics analyses. Working with jets instead of hadrons is an advantage because it greatly reduces the
888 number of objects we need to analyze per event. In addition, they work as a proxy for the fundamental
889 partons produced in the event.

890 Jets are obtained through jet finding algorithms. These are clustering algorithms that group together
891 experimental quantities (energy deposits in the calorimeters, tracks or particle flow objects) using a se-
892 quential recombination scheme. If the jets are reconstructed using only the information from the energy
893 clusters in the calorimeter they are called calorimeter or tower jets. Jets can also be reconstructed using

894 particle flow objects that combine information from the tracking system and from the calorimeters. These
895 jets are referred to as particle flow or energy flow jets (eflow in short).

896 A crucial property of jet finding algorithms is that they should be infrared and collinear safe, mean-
897 ing that the outcome of the algorithm (namely the number of jets and their properties) should not be
898 significantly modified by the emission of soft radiation or by a collinear splitting.

899 The most widely used jet finding algorithms are the k_T [49], the Cambridge/Aachen (C/A) [50] and
900 the anti- k_T [51]. They are based on measurements of the quantity:

$$d_{ij} = \min(k_{Ti}^{2p}, k_{Tj}^{2p}) \frac{\Delta_{ij}^2}{R^2}, \quad d_{iB} = k_{Ti}^{2p}, \quad (3.3)$$

901 referred to as a distance between entities i and j with d_{iB} being the distance between entity i and the
902 beam (B). $\Delta_{ij}^2 = (y_i - y_j)^2 + (\phi_i - \phi_j)^2$ and k_{Ti} , y_i and ϕ_i are the transverse momentum, rapidity and
903 azimuth of entity i . Here, k_T stands for the transverse momentum. For $p = 1, 0, -1$ we get the k_T , C/A
904 and anti- k_T algorithms, respectively.

905 The clustering algorithm starts by computing all d_{ij} and d_{iB} distances. If the smallest distance is a
906 d_{ij} , the four momenta of particle i and j are summed and the distances are updated. If the smallest
907 distance is a d_{iB} , particle i is removed and called a jet. This procedure is iterated until all particles are
908 clustered in jets.

909 It is worth discussing further the anti- k_T algorithm since it is the default algorithm used in most
910 analyses, including this one. In this algorithm, the Δ_{ij} distance between constituents i and j is weighted
911 by the inverse of the transverse momentum of the constituent with a largest k_T . This feature implies that
912 particles with larger momenta will have a smaller d_{ij} distance and therefore will be clustered first. This
913 prevents soft particles from being clustered among themselves before clustering the hardest particles.

914 In ATLAS, the transverse and longitudinal segmentation of the calorimeters allow for a three dimen-
915 sional reconstruction of particle showers which is based in a topological clustering algorithm. Topo-
916 clusters of calorimeters cells are seeded by cells whose absolute energy exceeds the electronic and
917 pile-up noise by four standard deviations. The topo-clusters are then expanded by adding all adjacent
918 cells with absolute energy two standard deviations above noise. Finally, all cells neighbouring the pre-
919 vious set are also added. After energy calibration, the topo-clusters are fed as input to a jet finding
920 algorithm.

921 **Boosted kinematic regime**

922 With the increase of the CM energy of particle colliders the production of particles with a transverse
923 momentum much larger than their mass became a reality. In this kinematic regime, referred to as boosted
924 due to the high Lorentz boost of the particles, traditional jet reconstruction algorithms, that rely on a one-
925 to-one correspondence between jets and partons, begin to fail [52].

Due to the high Lorentz boosts, decay products of heavy resonances get more collimated. The

angular separation of the decay products is approximately [53]:

$$\Delta R \sim \frac{2m}{p_T} \quad (3.4)$$

where p_T and m are the transverse momentum and mass of the decaying particle. In addition to decaying particles with a larger p_T , another event topology that can produce highly collimated particles is the decay of a particle with a very large mass. This scenario is of particular interest for new physics searches because BSM models often predict the existence of heavy particles.

Take, as an example, the decay of a Higgs boson to two b quarks. Considering that the p_T of the Higgs is approximately 200 GeV (which is a reasonable and commonly used value in boosted Higgs bosons searches) we get $\Delta R \sim 1$. For resolved jets, the default jet radius parameter used in ATLAS is 0.4. We see that for a $p_T \sim 200$ GeV the angular separation between the decay products of a Higgs boson is already similar to the default jet diameter, which can jeopardize the ability to resolve the individual decay products.

A possible workaround is to use a single jet with a larger R parameter to reconstruct both decay products. The problem with doing so is that we no longer have information about each individual decay product which means we are loosing some information about the event. We cannot, for example, compute angular variables between the decay products. This led to the development of techniques and observables that allow for the exploration of the intrinsic structure (or substructure) of these large- R jets. Some of these techniques are introduced and discussed in the following section.

3.3.1 Jet properties and substructure observables

In general, jet substructure variables aim to quantify the existence of energy clusters insider a jet. Each cluster is interpreted as corresponding to an individual jet. These are called subjets because they are contained inside the large- R jet that was reconstructed. Once they are identified, the subjets can be handled and used for the analysis like normal jets. However, a lot of the substructure techniques do not focus on reconstructing the subjets but rather on determining whether or not they exist, how many they are and how are they distributed inside the large- R jet.

Heavy resonances decaying to two(three) particles will produce large- R jets that are consistent with the existence of two(three) energy clusters. Examples of such topologies are the Higgs boson and top quark decays: the Higgs boson always decays to pairs of particles (leptons, quarks or bosons) and the top quark decays, with a probability close to 96%, to a b quark and a W boson that then decays to a pair of leptons or quarks. These topologies are usually referred to as two or three prong. In contrast, jets initiated by a gluon or a quark are not expected to have a meaningful substructure. The energy is expected to be concentrated around the jet axis following an isotropic distribution and to become less dense as we approach the jet's border. This is the signature of a one-prong topology. The previous discussion is valid at LO and captures the generic features of jets that are targeted by jet substructure techniques. Nonetheless, other effects may come into play. Take, for example, a highly virtual gluon with a high p_T . If it splits into two quarks the resulting jet may have two subjets and thus mimic the topology

960 of a heavy resonance decay.

The N-subjetiness variable [54], τ_N , may be used to identify jets compatible with N subjets. It is given by

$$\tau_N = \frac{1}{d_0} \sum_k p_T^k \min(\Delta R_1^k, \dots, \Delta R_N^k), \quad d_0 = \sum_k p_T^k R_0 \quad (3.5)$$

961 where the index k runs over all particles in a jet, the indexes 1 to N identify the number of axis inside the
962 jet and R_0 is the radius of the jet. This variable will have a small value if the particles with the highest p_T
963 (the ones we are most interested in) are clustered close to the axis (because ΔR will be small) and will
964 have a larger value otherwise. A jet with small τ_N is considered to be consistent with having N or fewer
965 subjets because all its constituents are aligned with the axis.

966 We usually use ratios of τ_N variables ($\tau_{MN} = \tau_M / \tau_N$). Of particular interest for this work is the τ_{21}
967 ratio. This observables can take values between zero and one. A small value (close to zero) indicates
968 that the jet is more compatible with two subjets than with one and therefore it can help discriminate
969 between two-prong and one-prong jets.

The Fox-Wolfram moments, H_l , can be used to identify jets that have a structure of two back-to-back subjets in their rest frames [55]. They are given by:

$$H_l = \sum_{i,j} \frac{|\vec{p}_i||\vec{p}_j|}{E^2} P_l(\cos(\theta_{ij})) \quad (3.6)$$

970 where θ_{ij} is the opening angle between energy clusters i and j with respect to the interaction point, E
971 is the total energy of the clusters in the jet rest frame and $P_l(x)$ are the Legendre polynomials. For a jet
972 that has a structure of two back-to-back subjets in its rest frame, $H_1 = 0$, $H_l \sim 1$ for even l , and $H_l \sim 0$
973 for odd l . This is what we expect for jets coming from the decay of a boosted resonance. In this work we
974 make use of H_2 .

In addition to jet substructure observables, more standard variables, from which we highlight the jet mass, can also be used to discriminate between jets coming from QCD background and jets resulting from heavy resonance decays. In the latter, the jet's invariant mass should roughly correspond to the mass of the resonance. The invariant mass of a jet, M , is calculated from the energies and momenta of its constituents as follows:

$$M^2 = \left(\sum_i E_i \right)^2 - \left(\sum_i \vec{p}_i \right)^2, \quad (3.7)$$

975 where E_i and \vec{p}_i are the energy and three-momentum of the i^{th} constituent. However, the mass resolution
976 is not expected to be very good for large-R jets because of all the extra QCD radiation that may be
977 caught inside the jet. A possible workaround is the use of jet grooming algorithms which we describe in
978 the following section.

979 3.3.2 Jet grooming algorithms

980 The main goal of jet grooming algorithms is to remove contamination of softer jet constituents from pileup
981 or underlying event and to leave behind the hard substructure. The main advantage of such algorithms is

982 that they improve the mass resolution of jets. These features are of particular interest in high luminosity
983 environments such as the HL-LHC and future high energy colliders.

984 The three main jet grooming algorithms are trimming, pruning and mass drop filtering. In this work
985 we do not use pruning or trimming, although these techniques might be worth exploring in future, more
986 comprehensive, studies. In particular, they can be useful to help reject pileup contributions. The mass
987 drop filtering procedure isolates relatively symmetric subjets within a jet, each with a significantly smaller
988 mass than the original jet [53]. This technique was developed and optimized using C/A jets for the search
989 of Higgs decaying to $b\bar{b}$ pairs [56]. It works as follows:

- The last step of the C/A clustering is undone such that the jet is split in two subjets, j_1 and j_2 with $m_{j_1} > m_{j_2}$. We require that there is a significant difference between the mass of the original jet, m_{jet} , and m_{j_1} : $m_{j_1}/m_{\text{jet}} < \mu_{\text{frac}}$, where μ_{frac} is a parameter of the algorithm. In addition, the splitting is required to be relatively symmetric:

$$\frac{\min[(p_T^{j_1})^2, (p_T^{j_2})^2]}{(m_{\text{jet}})^2} \times \Delta R_{j_1, j_2}^2 > y_{\text{cut}} \quad (3.8)$$

990 where y_{cut} is a parameter that defines the energy sharing between the subjets. It is usually taken
991 to be ~ 0.09 . If these two criteria are not met the jet is discarded.

- 992 • The subjets are clustered with the C/A algorithm with radius parameter $R_{\text{filt}} = \min[0.3, \Delta R_{j_1, j_2}/2]$.
993 All jet's constituents that are outside of the three hardest subjets are discarded and we obtained
994 the filtered jet and its subjets.

995 The subjets that are identified within a jet are interpreted as corresponding to the decay products of
996 the particle that produced the original jet. There are usually only two decay products. A third subjet is
997 allowed in order to account for extra QCD radiation.

998 3.4 Future Colliders

999 As we already argued in the beginning of this chapter, a larger CM energy is one of the factors driving
1000 the discovery potential of an accelerator. As far as we know today, proton-proton colliders are the main,
1001 and possibly only, man-made experimental tool available to explore particle physics in the energy range
1002 on tens of TeV, in a controlled way. With this in mind, new hadronic colliders with CM energies of the
1003 order of tens of TeV have been proposed. The main projects are the hadronic Future Circular Collider
1004 (FCC-hh) led by CERN and the Super Proton-Proton Collider (SPPC) proposed by China.

1005 In this work we focus on FCC-hh and use the established detector's baseline design as our starting
1006 point for this study. In the following section we describe in detail the FCC-hh accelerator and detector.

1007 3.4.1 The hadronic Future Circular Collider

1008 CERN's FCC study group was launched as a result of a recommendation made in the 2013 update
1009 of the European Strategy for Particle Physics that '*Europe needs to be in a position to propose an*

Table 3.2: Comparison between the working parameters of the LHC and of the FCC-hh. The values of the number bunches and of the number of events per bunch crossing are given assuming a bunch spacing of 25 ns.

Parameter	LHC	FCC-hh
Circumference [km]	27	100
CM energy [TeV]	13	100
Luminosity (peak) [$10^{34} \text{cm}^{-2}\text{s}^{-1}$]	1	30
Dipole field [T]	8.33	16
Nb. of bunches	2808	10600
Nb. of events per bunch crossing	27	1026

1010 *ambitious post-LHC accelerator project at CERN by the time of the next Strategy update*'. It investigates
 1011 the technological challenges and physics opportunities of a future circular collider. The design and
 1012 infrastructure are driven by a proton-proton collider (FCC-hh) requirements. Electron-positron (FCC-ee)
 1013 and electron-proton (FCC-eh) colliders are also being analyzed. The main goal of this effort is to deliver
 1014 a Conceptual Design Report (CDR) by the end of 2018. This document will include a first cost estimate
 1015 to be submitted for the next update of the European Strategy for Particle Physics, foreseen by 2019.

1016 The FCC-hh baseline design consists of a proton-proton circular collider with a maximum CM energy
 1017 of $\sqrt{s} = 100$ TeV housed by a 100 km tunnel in the area of Geneva. This machine will extend the
 1018 research program of the LHC (and of the HL-LHC) after these have reached their full discovery potential,
 1019 by around 2040. In addition, it will allow for the exploration of an entirely new kinematic regime, probing
 1020 energy scales where new physics may come into play. A possible way of defining the target luminosity of
 1021 this machine is to require that within the first year of operation it surpasses the exploration potential of the
 1022 LHC [57]. Comprehensive studies [57, 58] indicate that this can be achieved with an integrated luminosity
 1023 of the order of 10 ab^{-1} per experiment. Considering a reasonable operation period of 10 years this
 1024 leads to integrated luminosity per experiment of the order of 1 ab^{-1} per year. In this work, we consider
 1025 a slightly more optimistic scenario that sets the target integrated luminosity at 30 ab^{-1} [59].

1026 The FCC-hh is expected to work with a dipole field of 16 T and to provide a peak instantaneous
 1027 luminosity thirty times larger than the LHC. The number of bunches is expected to be almost a factor of
 1028 four larger than for the LHC and the number of events per bunch crossing is expected to be approximately
 1029 1000. The latter brings a lot of technical challenges because it means that the mean pileup expected
 1030 for the FCC-hh is almost 40 times larger than for the LHC. This requires the development of techniques
 1031 and algorithms that allow us to further reject pileup contributions (or improvement of already existing
 1032 techniques). Some relevant parameters of the LHC and FCC-hh are summarized in table 3.2.

1033 3.4.2 FCC-hh baseline detector

1034 The design of the FCC-hh baseline detector, which we describe in detail in this section, has been greatly
 1035 based on that of the ATLAS and CMS experiments, in particular the central barrel. The layers and sub
 1036 detectors are arranged in the same order and perform very similar roles. The geometry is cylindrical
 1037 and therefore we can use exactly the same coordinate system that was introduced in section 3.2.1. The

Table 3.3: Layout, granularity and energy resolution of the proposed hadronic calorimeter for the FCC-hh detector.

Parameter	Barrel	End-cap	Forward
η coverage	$ \eta < 1.3$	$1.0 < \eta < 1.8$	$2.3 < \eta < 6.0$
Layout	Sci-Pb-Steel (1 : 1.3 : 3.3)	LAr-Cu (1 : 5)	LAr-Cu (1 : 200)
Granularity ($\Delta\eta \times \Delta\phi$)	0.025×0.025	0.025×0.025	0.05×0.05
Energy resolution (σ_E/E)	$40\%/\sqrt{E} \oplus 2.5\%$	$50\%/\sqrt{E} \oplus 3\%$	$100\%/\sqrt{E} \oplus 5\%$

1038 dimensions are very close to the ones of ATLAS: 25 meters in height (diameter) and 48 m in length [60].

1039 A schematic representation of the FCC detector is shown in figure 3.2.

1040 The detector consists of trackers, EM and hadronic calorimeters and MS. The magnet configuration
 1041 consists of three solenoid magnets (one central-barrel and two forward) that surround the central bar-
 1042 rel calorimeters and the forward trackers. The center solenoid delivers a magnetic field of 4 T at the
 1043 interaction point [61].

1044 The tracker covers the pseudorapidity range $|\eta| < 6$ and is divided in three sub systems: inner,
 1045 outer and forward. The inner and outer trackers and the forward tracker are expected to cover the
 1046 pseudorapidity ranges $|\eta| < 2.5$ and $2.5 < |\eta| < 6.0$, respectively. The inner tracker will be instrumented
 1047 with pixel detectors while the outer and forward tracker will have layers of both pixel and strip detectors.

1048 The EM calorimeter [62, 63] covers the pseudorapidity range $|\eta| < 6$. It is divided in barrel, end-cap
 1049 and forward. These cover the pseudorapidity ranges $|\eta| < 1.5$, $1.4 < |\eta| < 2.5$ and $2.3 < |\eta| < 6$,
 1050 respectively. The proposed layout for the EM calorimeter is a LAr sampling configuration with lead, glue
 1051 and steal plates as absorbers. The granularity is expected to be two to four times better than for the
 1052 ATLAS ECAL. For the barrel calorimeter, the goal energy resolution is $10\%/\sqrt{E} \oplus 1\%$.

1053 The hadronic calorimeter [64] covers the pseudorapidity range $|\eta| < 6$. It is also divided in barrel,
 1054 end-cap and forward that cover the pseudorapidity ranges $|\eta| < 1.3$, $1.0 < |\eta| < 1.8$ and $2.3 < |\eta| < 6.0$,
 1055 respectively. The proposed layout for the barrel calorimeter consists of scintillator tiles interleaved with
 1056 lead and stainless steel plates as absorbers. The end-cap and forward calorimeters are expected to be
 1057 based on liquid argon with copper plates as absorbers. For the barrel and end-cap calorimeters, the
 1058 expected segmentation $\Delta\eta \times \Delta\phi = 0.025 \times 0.025$ while for the forward calorimeter it is $\Delta\eta \times \Delta\phi = 0.05 \times$
 1059 0.05. Overall, this corresponds to approximately four times the ATLAS HCAL granularity. The energy
 1060 resolution is expected to be $40\%/\sqrt{E} \oplus 2.5\%$, $50\%/\sqrt{E} \oplus 3\%$ and $100\%/\sqrt{E} \oplus 5\%$, for the barrel, end-
 1061 cap and forward calorimeters, respectively. The pseudorapidity coverage, layout, granularity and energy
 1062 resolution of the hadronic calorimeters are summarized in table 3.3.

1063 The muon spectrometer is divided in barrel, end-cap and forward regions that cover the pseudora-
 1064 pidity ranges $|\eta| < 1.0$, $1.0 < |\eta| < 2.5$ and $2.5 < |\eta| < 6.0$, respectively. The muon's system layout is a
 1065 layered structure of gas chambers.

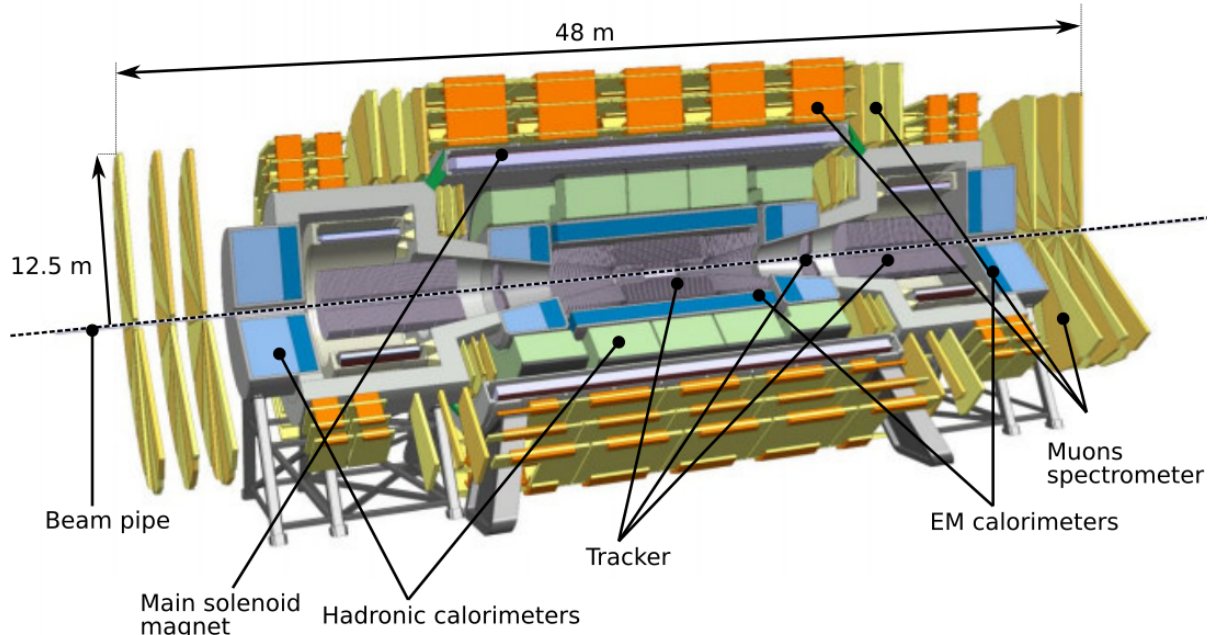


Figure 3.2: FCC detector baseline concept.

3.4.3 FCC-hh physics program

The FCC-hh physics program is vast and diverse. Within the SM, it includes the study of gauge bosons pair production and heavy flavor production, the measurement of the top quark's properties and the study of the EWSB mechanism via multi-Higgs production. In addition, heavy ions collisions will allow for a deeper understanding of the Quark-Gluon Plasma. From a BSM standpoint, searches for supersymmetric and dark matter particles in new kinematic regimes can be pursued. A comprehensive review of the physics potential of the FCC-hh can be found in Ref. [14]. This document collects the results of the many studies that have been carried out since the beginning of the FCC initiative, in 2014.

Regarding Higgs pair production, a maximum precision on the SM cross section of 3% is expected to be achieved using the $b\bar{b}\gamma\gamma$ final state. This would allow to constrain the Higgs triple coupling to be $\lambda_{hhh} \in [0.97, 1.03]$. The $hh \rightarrow b\bar{b}b\bar{b}$ would allow for a 5% precision on the SM cross section and to constraint the triple coupling to be $\lambda_{hhh} \in [0.9, 1.5]$. In spite of the larger background yield, the $b\bar{b}b\bar{b}$ channel provides a reasonable number of events in the tail of the m_{hh} distribution. As discussed in section 2.1.1, the tail of this distribution does not have a large contribution from the triangle diagram. Therefore, the sensitivity to the Higgs triple coupling is expected to be smaller. However, the high energy regime can be more sensitive to new physics contributions which makes the $b\bar{b}b\bar{b}$ channel a very interesting one.

The Higgs quartic coupling could be probed through triple Higgs production. In this case the most promising final state seems to be $b\bar{b}b\bar{b}\gamma\gamma$. This channel could constrain the Higgs quartic coupling to be $\lambda_{hhhh} \in [-4, 16]$.

1086 **Chapter 4**

1087 **State of the art**

1088 In this chapter we present the state of the art of searches for Higgs pairs production at the LHC and
1089 feasibility studies targeting searches for this process at future colliders. In addition, previous studies
1090 focusing on the granularity of the hadronic calorimeter as a key detector parameter are also reviewed.

1091 In section 4.1, we review the searches that have been conducted at the LHC by the ATLAS and CMS
1092 experiments. We include discussions on the different final states that were targeted and report on the
1093 constraints that were derived for the di-Higgs cross section and trilinear coupling. A brief overview of
1094 the current constraints on some BSM models is also presented. In section 4.2, we present the results
1095 obtained from feasibility studies that access the discovery potential for this process at the HL-LHC and
1096 at the FCC-hh. In section 4.3, we present previous studies on the impact of the granularity of the
1097 hadronic calorimeter on the spatial resolution of hadrons and on the resolution of the jet mass and of jet
1098 substructure observables.

1099 **4.1 Searches for Higgs pair production at the LHC**

1100 The searches performed so far at the LHC by ATLAS and CMS covered different decay channels and
1101 targeted not only the SM process but also some BSM scenarios where di-Higgs production is enhanced.
1102 Neither could achieve enough statistical significance to declare the measurement of this process in the
1103 SM nor have found any significant deviation from the expected values. These searches resulted in upper
1104 limits for the cross section of di-higgs production in the SM and for the values of the parameters of BSM
1105 benchmark theories. From the limits on the cross section it is also possible to constraint the values of
1106 the Higgs self coupling, $k_\lambda = \lambda_{hhh}/\lambda_{hhh}^{SM}$.

1107 The $hh \rightarrow b\bar{b}b\bar{b}$ channel [65, 66] benefits from the large branching fraction of $h \rightarrow b\bar{b}$ ($\sim 58\%$). In
1108 addition, ATLAS showed that this is the most sensitive channel to resonance masses over 500 GeV [67].
1109 However, this channel suffers with an overwhelming multijet background which drives the need for very
1110 tight trigger level cuts in order to bring the event rates down to manageable values.

1111 The $hh \rightarrow b\bar{b}\tau\tau$ analysis [68, 69] benefits from a sizable branching fraction of $h \rightarrow \tau^+\tau^-$ ($\sim 7.3\%$)
1112 and from a relatively small background contribution from other SM processes. These searches target

1113 the semi-leptonic decay of the $\tau\tau$ pair to reduce contamination from QCD processes.

1114 The $hh \rightarrow b\bar{b}\gamma\gamma$ [70, 71], $WW^*\gamma\gamma$ [67, 72], $ZZ^*\gamma\gamma$ [72] analysis can make use of very efficient diphoton triggers and isolation criteria that greatly reduce multijet background. In addition the excellent mass resolution of $h \rightarrow \gamma\gamma$ can be exploited. The $hh \rightarrow b\bar{b}WW^*$ channel also benefits from the large branching fraction of $h \rightarrow W^+W^-$ ($\sim 21\%$).

1118 The most stringent upper limit on the cross section of Higgs pair production comes from a combination
1119 of three searches using up to 36.1 fb^{-1} of proton-proton collision data at a CM energy of $\sqrt{s} = 13$
1120 TeV collected with the ATLAS detector [73]. The combination is based on the three most sensitive decay
1121 channels of Higgs boson pairs, i.e., $hh \rightarrow b\bar{b}\gamma\gamma$, $hh \rightarrow b\bar{b}\tau^+\tau^-$ and $hh \rightarrow b\bar{b}b\bar{b}$. The combined observed
1122 limit on the non-resonant Higgs boson pair cross-section is 0.223 pb at 95% CL, which corresponds to
1123 6.7 times the cross-section predicted by the SM. The ratio of the Higgs boson self-coupling to its SM
1124 expectation, k_λ , is constrained, at 95% CL, to be $-5.0 < k_\lambda < 12.1$.

1125 The upper limits on the cross section (at 95% CL) of Higgs pair production at 8 TeV as a function of
1126 the mass of a spin 0 resonance are summarized in figure 4.1(a) [70]. The limits were obtained using
1127 data collected with the CMS detector and come from searches using different final states, namely, $b\bar{b}\gamma\gamma$
1128 (blue), $b\bar{b}b\bar{b}$ (red and pink) and $b\bar{b}\tau\tau$ (green). Depending on the analysis, the corresponding integrated
1129 luminosity varies between 17.9 fb^{-1} and 19.7 fb^{-1} . The results are usually interpreted in the framework
1130 of the Randall-Sundrum models such that the spin 0 resonance corresponds to the radion that decays
1131 to a pair of Higgs bosons. For a mass of 1 TeV the upper limit on the cross section is approximately 12
1132 pb.

1133 The upper limits on the cross section (at 95% CL) of Higgs pair production as a function of the mass
1134 of a heavy scalar Higgs, m_H , are summarized in figure 4.1(b) [74]. The limits were obtained through a
1135 combination of searches performed in the $hh \rightarrow b\bar{b}\gamma\gamma$, $hh \rightarrow b\bar{b}b\bar{b}$, $hh \rightarrow b\bar{b}\tau^+\tau^-$ and $hh \rightarrow \gamma\gamma WW^*$
1136 channels using proton-proton collision data corresponding to an integrated luminosity of 20.3 fb^{-1} col-
1137 lected with the ATLAS detector at a CM energy of $\sqrt{s} = 8 \text{ TeV}$. The improvement above $m_H = 500 \text{ GeV}$
1138 is due to the sensitivity of the $hh \rightarrow b\bar{b}b\bar{b}$ analysis. For $m_H = 900 \text{ GeV}$ the observed limit is 0.015 pb .

1139 4.2 Feasibility studies for high-luminosity and future colliders

1140 Without any BSM contribution, the discovery of Higgs pairs production in the four b quarks final state at
1141 the LHC is highly unlikely even considering the total expected integrated luminosity of 300 fb^{-1} . There
1142 might be evidence for this process but retrieving useful information about the value of the Higgs tri-
1143 linear coupling will remain out of reach. Nonetheless, the HL-LHC as well as future colliders pose a
1144 good opportunity for the discovery and precision studies of this process. Therefore, Monte Carlo stud-
1145 ies assessing the feasibility of searches for $hh \rightarrow b\bar{b}b\bar{b}$ at the HL-LHC and at the FCC-hh have been
1146 performed.

1147 For the HL-LHC, a study including the $pp \rightarrow b\bar{b}b\bar{b}$, $pp \rightarrow b\bar{b}jj$, $pp \rightarrow jjjj$ and $pp \rightarrow t\bar{t} \rightarrow b\bar{b}jjjj$
1148 backgrounds reports a significance (S/\sqrt{B}) of 4 (1.3) for an integrated luminosity of 3000 (300) fb^{-1} [75].
1149 The analysis is performed in three orthogonal regions (boosted, intermediate and resolved) and the

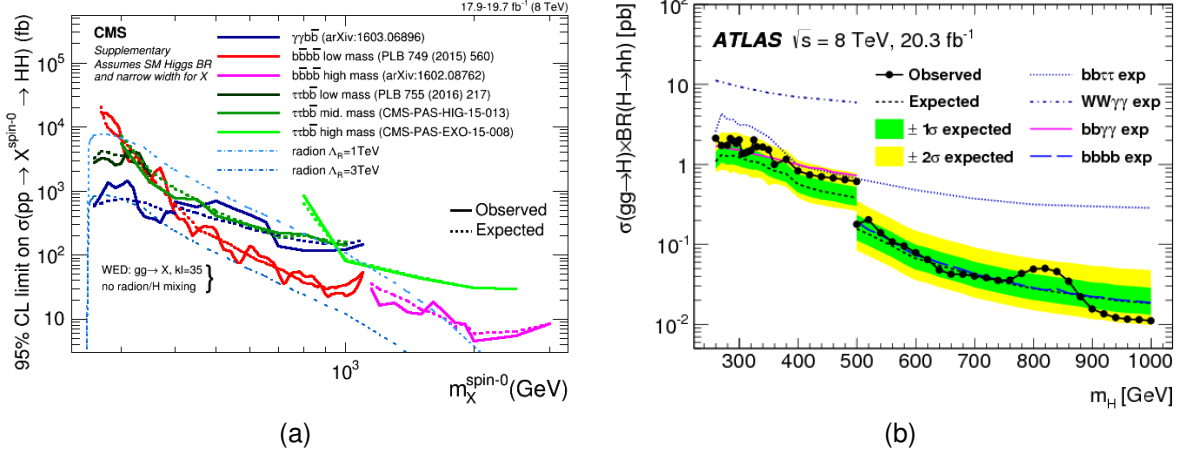


Figure 4.1: Exclusion limits (at 95% CL) on the cross section of resonant Higgs pair production from the decay of heavy scalar particles. These results were obtained using proton-proton collision data collected with the CMS (a) and ATLAS (b) detector at a CM energy of $\sqrt{s} = 8$ TeV and result from the combination of different channels. Plots from Refs. [70, 74], respectively.

reported significance is obtained from the combination of these three regions. The highest significance ($S/\sqrt{B} = 2.9$) is achieved in the boosted category. In addition, the impact of pile up is evaluated. Considering a mean pile up of 80 and making use of jet grooming techniques, a significance of 3.1 (1.0) for an integrated luminosity of 3000 (300) fb^{-1} is reported (also considering the three analysis regions). This work makes use of artificial neural networks (ANN's) as well as of jet substructure observables to further increase the signal-background separation. Furthermore, single Higgs backgrounds, namely $Z(\rightarrow b\bar{b})h(\rightarrow b\bar{b})$, $t\bar{t}h(\rightarrow b\bar{b})$ and $b\bar{b}h(\rightarrow b\bar{b})$, are shown to be negligible for the analysis, when compared to the dominant QCD multijet background.

ATLAS and CMS also carried out preliminary studies for the sensitivity on the trilinear coupling at the HL-LHC. Several channels have been investigated: $hh \rightarrow b\bar{b}\gamma\gamma$, $hh \rightarrow b\bar{b}\tau^+\tau^-$, $hh \rightarrow b\bar{b}WW^*$ and $hh \rightarrow b\bar{b}b\bar{b}$. The $b\bar{b}\gamma\gamma$ final state is the most sensitive one. In this channel, ATLAS and CMS reported significances of 1.05σ [76] and 1.6σ [77], respectively, for an integrated luminosity of 3000 fb^{-1} . Taking, as an example, the ATLAS result, the achieved significance translates to an upper limit on the total di-Higgs cross section of approximately twice the SM value. This corresponds to an exclusion limit of $-0.8 < k_\lambda < 7.7$. The analysis conducted by ATLAS in this channel is done at generator level. The energy and momenta of the particles are smeared to simulate the detector's response. A mean pile up of 200 is considered. No MVA techniques are employed in the analysis.

For the $hh \rightarrow b\bar{b}b\bar{b}$ channel, ATLAS states that a cross section 5.2 times larger than the SM value can be excluded at 95% CL, with systematic uncertainties being taken into consideration. The Higgs trilinear coupling is expected to be constrained to $-3.5 < k_\lambda < 11$. These results are based on the extrapolation of the current results obtained with the 2016 dataset, comprising an integrated luminosity of 10.1 fb^{-1} . This study is based only on the resolved analysis documented in Ref. [65].

For the FCC-hh, a recent study that uses as signal sample $pp \rightarrow hhj \rightarrow b\bar{b}b\bar{b}j$ and that includes only the irreducible background $pp \rightarrow b\bar{b}b\bar{b}j$ reports a significance of 6.61 for an integrated luminosity

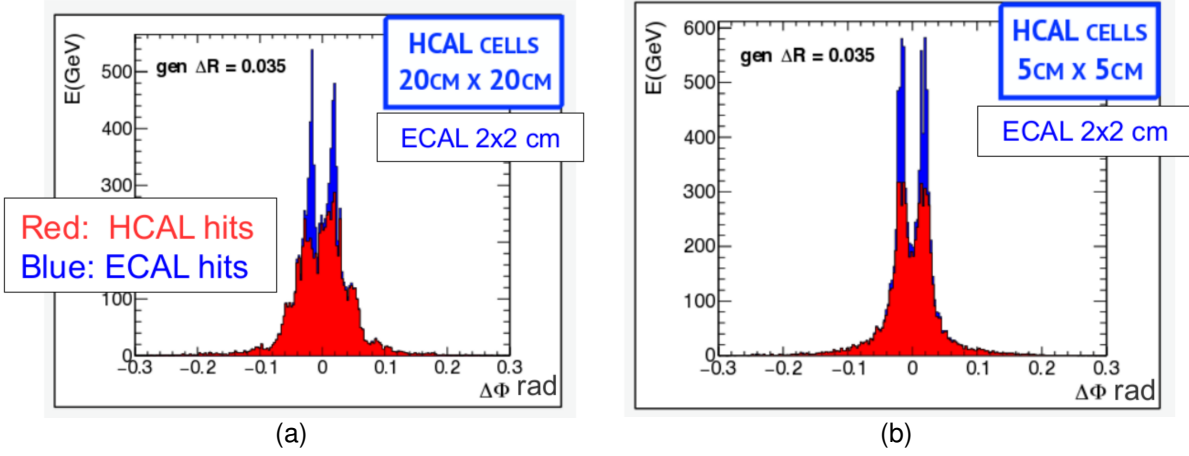


Figure 4.2: Azimuthal distribution of the energy deposits in the ECAL and HCAL for a pair of K_L^0 with $E = 100$ GeV for an hadronic calorimeter with $20\text{ cm} \times 20\text{ cm}$ (a) and $5\text{ cm} \times 5\text{ cm}$ (b). Figures from Ref. [80] (based on Ref. [79]).

of 30 ab^{-1} , considering an analysis that targets the boosted region [59]. The extra jet in the signal sample has $p_T > 200$ GeV which provides the Higgs pair with a large Lorentz boost. This enhances the sensitivity to the Higgs boson self coupling because it favors highly boosted virtual Higgs bosons decaying to a pair of Higgs bosons. The analysis relies on the jet substructure observable τ_{21} and on a tight mass cut around the Higgs mass. No multivariate techniques are employed.

A study comparing the feasibility of the search for di-Higgs production in the $b\bar{b}b\bar{b}$ in the HL-LHC and at the FCC-hh was presented in Ref. [78]. Only the irreducible background is considered. For a boosted region, cut based analysis, a significance of 1.1 is reported for an integrated luminosity of 3 ab^{-1} at $\sqrt{s} = 14$ TeV (HL-LHC). For an integrated luminosity of 10 ab^{-1} at $\sqrt{s} = 100$ TeV, which corresponds to the FCC-hh, this number is 5.7. While the significance is large for the FCC-hh, the reported signal to background ratio (S/B) is approximately one order of magnitude smaller, which means the measurement might be more sensitive to systematic uncertainties on the backgrounds.

4.3 Hadronic calorimeter granularity studies

Even before the baseline design for the FCC-hh was established, there were studies regarding the impact of the granularity of the calorimeters in the spatial resolving power of hadronic showers and on the resolution of jet mass and substructure variables. These studies targeted the development of future colliders and greatly influenced the baseline design of the FCC-hh.

The granularity of hadronic calorimeters is a key parameter for future collider detectors because it determines how well we can resolve energy deposits from pileup vertices and highly-boosted jet topologies. In Ref. [79], the use of smaller calorimeter cells (smaller than the ones that are used in currently operating hadronic calorimeters) to resolve individual hadrons is investigated. For two Kaons (K_L^0) with an energy of 100 GeV each and with a truth level separation (ΔR) equal to 0.035 the energy deposited in the ECAL (blue) and HCAL (red) is shown as a function of ΔR for HCAL cells with sizes $20\text{ cm} \times 20\text{ cm}$

1197 $(\Delta\eta \times \Delta\phi = 0.1 \times 0.1)$ and $5 \text{ cm} \times 5 \text{ cm}$ ($\Delta\eta \times \Delta\phi = 0.022 \times 0.022$) in figures 4.2(a) and 4.2(b),
1198 respectively. The ECAL segmentation is equal to $2 \text{ cm} \times 2 \text{ cm}$. It is shown that for a granularity of
1199 $\Delta\eta \times \Delta\phi = 0.022 \times 0.022$ both hadrons can be resolved in the HCAL.

1200 Additional studies focusing on the jet mass resolution and on the resolution of jet substructure ob-
1201 servables were performed for three calorimeter configurations (HCAL and ECAL). Some of these studies
1202 were presented in major conferences focused on future colliders, namely FCC week 2015 and 2016 and
1203 BOOST 2017. Here, we show results presented in Refs. [80–82]. The calorimeter configurations tested
1204 are: HCAL(ECAL) $0.1(0.025) \eta \times 5.6(1.4)^\circ \phi$, HCAL(ECAL) $0.05(0.012) \eta \times 2.8(0.7)^\circ \phi$ and HCAL(ECAL)
1205 $0.025(0.006) \eta \times 1.4(0.35)^\circ \phi$. For the segmentation in ϕ the numbers are give in degrees. For the HCAL,
1206 these correspond to approximately $\Delta\eta \times \Delta\phi = 0.1 \times 0.1, 0.05 \times 0.05, 0.025 \times 0.025$.

1207 For $t\bar{t}$ events generated at NLO with MadGraph5 and passed through Delphes 3.2 to simulate de-
1208 tector response, the energy flow jet mass distribution for $p_T(\text{jet}) > 3 \text{ TeV}$ is shown in figure 4.3(a) [81].
1209 The jet mass resolution is shown in figure 4.3(b). For $\Delta\eta \times \Delta\phi = 0.1 \times 0.1$ cells the root mean square
1210 (RMS) of the distribution is 0.130. This value decreases to 0.090 and 0.088 for $\Delta\eta \times \Delta\phi = 0.05 \times 0.05$
1211 and $\Delta\eta \times \Delta\phi = 0.025 \times 0.025$ cells, respectively. This indicates that the mass resolution increases as
1212 the granularity of the HCAL increases.

1213 Regarding jet substructure, the resolution of the τ_{32} variable in QCD dijet events generated with
1214 Pythia8 is shown in figure 4.4(a) for particle flow jets [81]. The same distribution is shown in figure 4.4(b)
1215 for calorimeter jets. Regardless of the type of jets used (eflow or tower jets), the τ_{32} resolution increases
1216 as the HCAL resolution increases. In addition, it is important to note that the resolution is a lot worse
1217 when using tower jets which is an indication that exploiting tracking information is vital to achieve a good
1218 resolution in substructure variables.

1219 Another interesting result, presented in Ref. [80], has to do with the overlap between the τ_{21} distribu-
1220 tion for jets resulting from QCD interactions and from the decay of a W boson. Jets with p_T of 2.5 TeV
1221 show a reduction in overlap ($80\% \rightarrow 60\%$) going from $\Delta\eta \times \Delta\phi = 0.1 \times 0.1$ to $\Delta\eta \times \Delta\phi = 0.005 \times 0.005$
1222 HCAL cells. For $5(10) \text{ TeV}$ jets the overlap varies from $88(91)\%$ to $78(85)\%$. However, for 20 TeV jets, the
1223 change in the HCAL granularity does not significantly modify the overlap, as is shown in figure 4.5.

1224 In summary, previous studies focus on the impact of granularity in the resolution of jet mass and jet
1225 substructure observables. We did not find any studies that explored the change in the significance of a
1226 given analysis as a function of the granularity or of the detector configuration.

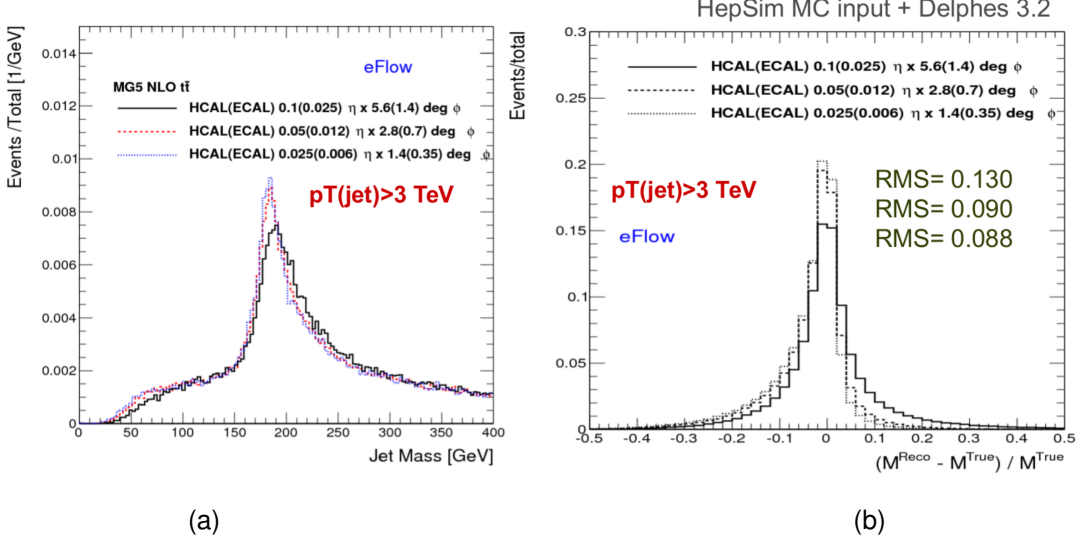


Figure 4.3: Jet mass (a) and jet mass resolution (b) plots in $t\bar{t}$ events for eflow jets with $p_T > 3$ TeV for three different HCAL and ECAL configurations: HCAL(ECAL) 0.1(0.025) $\eta \times 5.6(1.4)$ $\circ \phi$, HCAL(ECAL) 0.05(0.012) $\eta \times 2.8(0.7)$ $\circ \phi$ and HCAL(ECAL) 0.025(0.006) $\eta \times 1.4(0.35)$ $\circ \phi$. Plots from Ref. [80].

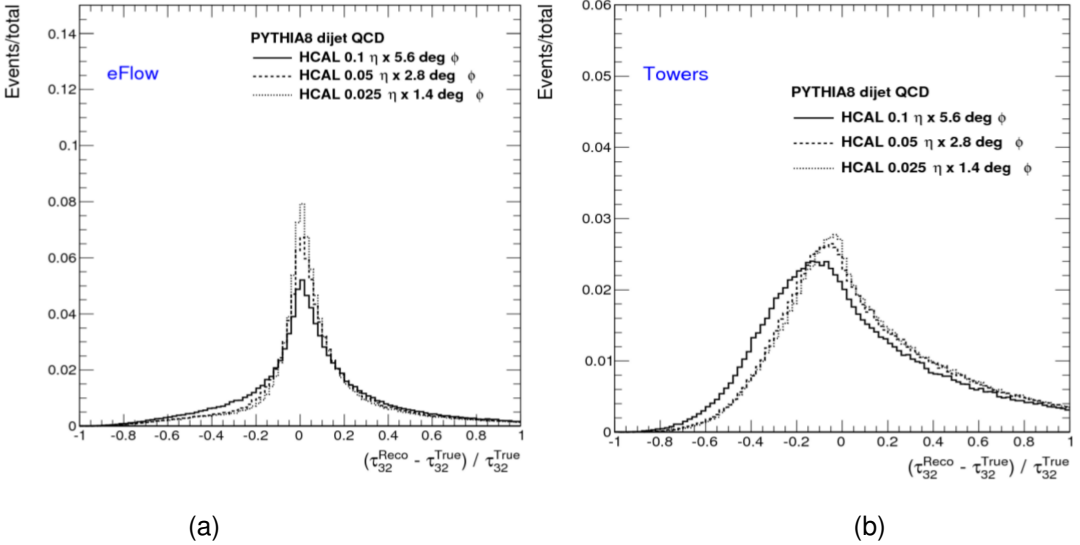


Figure 4.4: τ_{32} resolution plots for QCD dijet events reconstructed using eflow jets (a) and tower jets (b). Plots from Ref. [81].

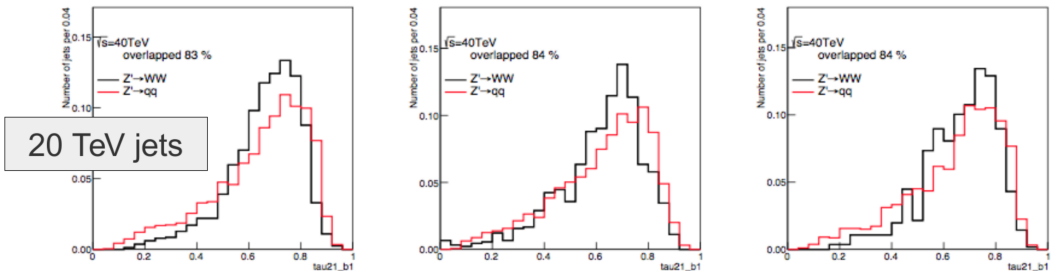


Figure 4.5: τ_{21} variable for 20 TeV W (black) and QCD jets (red) for three HCAL granularities: $\Delta\eta \times \Delta\phi = 0.1 \times 0.1$ (left), $\Delta\eta \times \Delta\phi = 0.022 \times 0.022$ (middle) and $\Delta\eta \times \Delta\phi = 0.005 \times 0.005$ (right). Plots from Ref. [80].

1227 Chapter 5

1228 Sample generation and analysis tools

1229 A crucial component of this work is the generation of the Monte Carlo samples that are used in the anal-
1230 ysis. They are produced using fast simulation. We use the software and machinery that was developed
1231 by the FCC study group at CERN. The simulation work flow and Monte Carlo samples are described in
1232 this chapter.

1233 In section 5.1 we introduce the generators used to produce the Monte Carlo samples and briefly
1234 describe their working principles and functionalities. We then focus on the FCC-hh software, in subsec-
1235 tion 5.1.2, and explain how the previously described simulation work flow is implemented. A detailed
1236 description of the technical settings used to produce the samples is provided in sections 5.2 and 5.2.3.

1237 5.1 Fast simulation workflow

1238 The Monte Carlo samples used in this study were generated using MadGraph5_aMC@NLO [83]. The
1239 showering and hadronization are simulated using Pythia 8 [84] and the detector response is parametrized
1240 using Delphes 3 [85]. These samples are available at the CERN EOS storage.

1241 MadGraph5 is a matrix element generator for high energy physics processes, such as decays and
1242 scatterings. The user specifies the desired process in terms of the initial and final states and can impose
1243 additional constraints such as allowing for a number of refined criteria, including forced or forbidden s-
1244 channel resonances, excluded internal particles, and forced decay chains of final state particles [83].
1245 As a result, MadGraph automatically generates the corresponding Feynman diagrams and creates the
1246 necessary code to compute the matrix element at a given point of the phase space. The output file is
1247 written in the Les Houches Accord [86].

1248 Pythia8 is frequently used for event generation in high energy physics. In this work, however, we use
1249 it only to simulate the showering and hadronization process and not the parton level hard process which
1250 is simulated in MadGraph5. The Les Houches file that is produced by MadGraph5 is used as input to a
1251 Pythia8 program that can decay unstable particles, simulate initial and final state showers as well as the
1252 hadronization of coloured particles, such as quarks and gluons. The desired settings can be specified
1253 in an additional file, a card, that is used as input for a Pythia8 run.

1254 Delphes3 allows for a quick and simple simulation of the detector's response [85]. Its goal is to allow
1255 the fast simulation of a multipurpose detector for phenomenological studies. The simulation includes a
1256 track propagation system, electromagnetic and hadronic calorimeters and a muon identification system.
1257 Low level physics objects, such as tracks and energy deposits, and high level physics objects, such as
1258 leptons and jets, are reconstructed from the detector's response and can be used to perform physics
1259 analysis. In the following paragraphs we briefly describe how the detector response is simulated and
1260 how jet reconstruction is performed.

1261 The magnetic field is uniform, axial and parallel to the beam direction. Charged particles follow a
1262 helicoidal trajectory from the interaction point to the calorimeters while neutral particles have a straight
1263 line trajectory. The probability of a charged particle being reconstructed as a track is defined by the
1264 user. Only a smearing in the modulus of the transverse momentum is applied (not to the direction). The
1265 tracking efficiency, as well as energy and momentum resolutions, are specified by the user and may in-
1266 clude a dependency on the particle type, momentum and pseudorapidity. The calorimeters have a finite
1267 segmentation in the (η, ϕ) plane and the cell size can be defined in the configuration file. The amount
1268 of energy deposited in the calorimeters by each particle type can be defined by the user. By default,
1269 stable hadrons deposit all their energy in the HCAL although in a real detector a significant fraction of
1270 their energy is deposited in the ECAL. The energy resolution of the ECAL and HCAL are parameter-
1271 ized as a function of η and include stochastic, noise and constant terms: $\sigma(E)/E = a/\sqrt{E} \oplus b$. The
1272 electromagnetic and hadronic energy deposits are independently smeared by log-normal distributions.

1273 Jets can be produced using generator level long-lived particles after showering and hadronization,
1274 tracks, calorimeter towers or particle-flow tracks and towers. These are referred to as generator, track,
1275 calorimeter or particle-flow jets, respectively. For generator level jets no detector simulation nor recon-
1276 struction are taken into account. In spite of the type of jet, the user can choose the jet clustering algorithm
1277 and the values of its parameters as well as the minimum transverse momentum of the jets that are stored
1278 in the final collection. Delphes integrates the FastJet package [87] and therefore allows jet reconstruc-
1279 tion with the most popular jet reconstruction algorithms, namely, anti- k_T , k_T and Cambridge-Aachen
1280 (C/A). Jets resulting from the hadronization of a b quark (known as b jets), are identified if a b quark is
1281 found within a ΔR distance from the jet's axis. The tagging efficiency and mis-tagging probabilities can
1282 be defined by the user.

1283 5.1.1 Particle flow and calorimeter reconstruction in Delphes

1284 In Delphes, hadronic jets can be reconstructed using only the information from the HCAL towers or using
1285 a particle flow algorithm that combines information from the tracking system and from the HCAL towers.
1286 These two approaches create jets that are referred to as calorimeter and particle flow jets, respectively.
1287 The latter can also be referred to as energy flow jets (eflow jets in short). In this work we performed the
1288 analysis using both sets of jets and compare the results. Therefore we briefly describe them here.

1289 Calorimeter jets are very simple. They are reconstructed using as input for the jet clustering algorithm
1290 the 4-vectors associated with the calorimeter towers, after a cell energy smearing has been applied.

1291 Therefore the spatial resolution is limited by the transverse segmentation of the calorimeters.
 1292 The goal of the particle flow approach is to make use of all the available information provided by the
 1293 various sub-detectors for reconstructing an event [85]. This approach is used by some experimental
 1294 collaborations [88, 89] but the exact implementation depends on the specificities of the experiment. If
 1295 the momentum resolution of the tracking system is better than the energy resolution of the calorimeters
 1296 it might be convenient to use the tracking information to estimate the momentum of charged particles.
 1297 In real experiments, the tracking resolution is only better than the calorimeter's energy resolution up to
 1298 some energy threshold. However, in Delphes, it is assumed that it is always convenient to estimate the
 1299 momentum of charged particles via the tracker.

1300 The particle flow algorithm works as follows [85]. For each calorimeter tower it counts:

- 1301 • the total energy deposited in ECAL and HCAL, E_{ECAL} and E_{HCAL} , respectively;
- 1302 • the total energy deposited in ECAL and HCAL originating from charged particles for which a track
 1303 has been reconstructed, $E_{\text{ECAL,trk}}$ and $E_{\text{HCAL,trk}}$, respectively.

Then it defines $\Delta_{\text{ECAL}} = E_{\text{ECAL}} - E_{\text{ECAL,trk}}$, $\Delta_{\text{HCAL}} = E_{\text{HCAL}} - E_{\text{HCAL,trk}}$ and computes $E_{\text{Tower}}^{\text{eflow}}$ given by

$$E_{\text{Tower}}^{\text{eflow}} = \max(0, \Delta_{\text{ECAL}}) + \max(0, \Delta_{\text{HCAL}}). \quad (5.1)$$

1304 All reconstructed tracks result in a particle flow track. If $E_{\text{Tower}}^{\text{eflow}} > 0$ a particle flow tower is created
 1305 with energy $E_{\text{Tower}}^{\text{eflow}}$. The particle flow tracks and towers are then used as input for the jet clustering
 1306 algorithms.

1307 5.1.2 FCC-hh software

1308 FCC software (FCCSW) [90], common to all FCC studies (electron-electron, electron-hadron and hadron-
 1309 hadron) has been developed and is maintained by the FCC study group. The software is based on Gaudi
 1310 [91]. An FCC Event Data Model based on Podio [92] was also developed. It consists in specific classes
 1311 that encode the information about the events.

1312 The FCC-hh study group is responsible for the generation of Monte Carlo quick simulation samples
 1313 for the main benchmark processes for the FCC-hh and corresponding backgrounds. The samples are
 1314 generated using the workflow described in the previous section. CERN users can request rights to run
 1315 the EventProducer package [93] and produce samples for any desired process using the machinery that
 1316 is already implemented. In addition, the FCC Event Data Model classes are directly accessible and can
 1317 be used to read the ROOT files that are produced after the events are passed through Delphes.

1318 The machinery to submit jobs to CERN's batch system is also implemented for both the generation
 1319 (MadGraph5) and reconstruction (Pythia8 plus Delphes3) levels.

1320 In this work we make use of this software in order to produce the necessary samples.

1321 **5.2 Signal and background samples**

1322 In this work we focus on the $hh \rightarrow b\bar{b}b\bar{b}$ channel and perform an analysis targeting the boosted kinematic
1323 region. The main backgrounds are multijet and $t\bar{t}$ production and the irreducible $pp \rightarrow b\bar{b}b\bar{b}$ process. This
1324 was introduced and motivated in chapter 1 and it is discussed in detail in chapter 6. Here we provide a
1325 technical description of how the signal and background samples were generated.

1326 **5.2.1 MadGraph**

1327 The irreducible background is generated with an extra jet with a high p_T at generator level, $4b + j$,
1328 where j stands for a light jet (initiated by a gluon or u, d, c, s quarks). This is referred to as the four
1329 flavor scheme. A high- p_T extra jet forces the four b quarks to have a high Lorentz boost and therefore
1330 increases the probability of the events being reconstructed with two large- R jets consistent with a two-
1331 prong substructure. For this process, QCD and electroweak contributions are considered separately,
1332 i.e, we include three different types of samples: one in which only QCD processes are considered, one
1333 in which only electroweak processes are considered and one in which both process are considered
1334 simultaneously. The samples do not overlap. The $4b + j$ QCD sample is constituted by two independent
1335 samples that have a different generator level cut in the minimum p_T of the light jets, namely, $200 <$
1336 $p_{T,j}^{\min} < 500$ GeV and $p_{T,j}^{\min} > 500$ GeV. This allows for a more efficient generation.

1337 The multijet background is simulated through $jj + 0/1/2 j$ where j stands for a light or b jet (five flavor
1338 scheme). This background is divided into several individual samples that are produced in different H_T
1339 regions, where H_T is the scalar sum of the p_T of all partons at generator level. The minimum(maximum)
1340 allowed H_T is 500(100,000) GeV. Since these backgrounds are QCD processes, the p_T distribution of
1341 the final state jets falls very steeply as the p_T increases. Therefore, if one were to generate events for
1342 these processes without restricting the phase space, most events would consist of jets with a very low
1343 p_T which are exactly the type of events that are rejected the most by a boosted analysis (see chapter
1344 6 for more details on the event topology that is targeted and on the analysis strategy). As we move to
1345 regions of the phase with a higher H_T the cross section decreases meaning we need fewer MC events
1346 to properly simulate the background in that region.

1347 Note that for the $4b + j$ (QCD) and $jj + 0/1/2 j$ samples we do not take into account the regions of the
1348 phase space with $p_{T,j} < 200$ GeV and with $0 < H_T < 500$ GeV. We assume that we can reject most of
1349 the events (if not all) with these kinematic characteristics by going to a sufficiently boosted region of the
1350 phase space. In addition, note that after the showering procedure there could be some overlap between
1351 the $4b + j$ and $jj + 0/1/2 j$. This is taken care of in our analysis code: if an event from the $jj + 0/1/2 j$
1352 sample has four b quarks at truth level (which happens for approximately 0.01% of the events) then we
1353 do not consider it because it will certainly overlap with an event from the $4b + j$ sample.

1354 The $t\bar{t}$ background sample is generated with extra jets at generator level, $t\bar{t} + 0/1/2 j$, using the five
1355 flavor scheme. We consider an inclusive sample for this background, meaning that we do not force any
1356 particular decay of the top quark or of the subsequent particles.

1357 For the hh SM signal sample, one of the Higgs is decayed to $b\bar{b}$ in MadGraph. The reasoning behind

1358 this choice is that most searches for Higgs pair production make use of a final state that includes at
 1359 least two b quarks in order to keep the cross section times BR of the process large enough. In addition,
 1360 this method allows the same generator level samples to be used to perform different analysis, simply by
 1361 choosing the decay channel of the remaining Higgs boson. The decay of the remaining Higgs boson
 1362 can be implemented in Pythia, in the case of this work, to $b\bar{b}$.

1363 The generator level cuts for the signal and background samples are summarized in table D.1 in
 1364 appendix D.

1365 Signal samples - BSM

1366 In addition to the SM di-Higgs signal, we also explore the signature and analysis sensitivity for di-Higgs
 1367 signals produced by two benchmark BSM models: CP-conserving type II 2HDM and a simplified dark
 1368 matter model (DM) with a spin 0 mediator. These models were described in section 2.2.

1369 Both models are readily available in FeynRules [94] model database and can be straightforwardly
 1370 implemented in Madgraph5. The parameters of the models, namely the masses of the new particles,
 1371 can be changed by the user. In the case of this work, we want new particles to have a large mass so
 1372 that they produce SM Higgs pairs with a high Lorentz boost.

1373 For the DM model [18], the spin 0 mediator's mass is set at 1 TeV. The cross section for the signal
 1374 generated with this model is smaller than the cross section of the SM signal (approximately 0.2 pb *versus*
 1375 0.7 pb) and therefore this model is not excluded by experimental data.

1376 For the 2HDM [95, 96], a finer tuning of the parameters is required because the model is very general
 1377 and has many free parameters. In addition, it is written in the Higgs basis such that we need to convert
 1378 the parameters from the physical basis (introduced in section 2.2) to this basis. The free parameters of
 1379 the model are the masses of the neutral, $m_{h_1}, m_{h_2}, m_{h_3}$, and charged scalars, m_{hc} , the neutral scalars
 1380 mixing angles, $\text{mix}_h, \text{mix}_{h_2}, \text{mix}_{h_3}$, the real and imaginary parts of the up, down and charged lepton
 1381 3×3 Yukawa matrices, $GUR, GUI, GDR, GDI, GLR, GLI$ and the values (real and imaginary parts)
 1382 of the second, third and seventh quartic couplings, $l_{2,3,7}.$. In the CP-conserving model $h_{1,2,3}$ can be
 1383 identified with the physical states h, H and A , respectively.

We start from the following parameters (in the physical basis):

$$\begin{aligned}
 m_h &= 125 \text{ GeV}, & m_H &= 900 \text{ GeV}, & m_A &= 850 \text{ GeV}, & m_{H^\pm} &= 800 \text{ GeV} \\
 \beta &= \frac{\pi}{4}, & \alpha &= -0.75 \\
 m_{12}^2 &= [(m_H^2 + m_A^2 + m_{H^\pm}^2)/3] \cos(\beta) \sin(\beta) \simeq 181041.6667.
 \end{aligned} \tag{5.2}$$

In the Higgs basis, the input parameters for the model are

$$\begin{aligned}
m_{h_1} &= 125 \text{ GeV}, & m_{h_2} &= 900 \text{ GeV}, & m_{h_3} &= 850 \text{ GeV}, & m_{hc} &= 800 \text{ GeV} \\
mix_{h_2} &= mix_{h_3} = 0 \\
mix_{h_1} &= \frac{\pi}{2} - (\beta - \alpha) \simeq 0.035 \\
l_2 &\simeq 0.27, & l_3 &\simeq 9.46, & l_7 &\simeq 0.46.
\end{aligned} \tag{5.3}$$

1384 The masses of the scalars cannot change when going from one basis to the other. Therefore we set
1385 them to the exact same values. $mix_{h_2}, mix_{h_3} = 0$ because we are considering the CP-conserving
1386 model. To obtain the values of $l_{2,3,7}$ we use Eq. 11 from Ref. [24] and write the λ parameters of the
1387 scalar potential in terms of the parameters defined in Eq. 5.2. Then we use Eq. 47,48 and 50 from Ref.
1388 [97] to obtain the values of the quartic coupling in the Higgs basis.

Regarding the Yukawa interactions, we work in the type II model. Following the type II restriction file found in Ref. [95] we set

$$\begin{aligned}
GLR &= GLI = GDI = GUI = 0 \\
GDR &= \text{diag} \left(0, 0, \frac{m_b \sqrt{2} \tan(\beta)}{v} \right) \\
GUR &= \text{diag} \left(0, 0, -\frac{m_t \sqrt{2}}{v \tan(\beta)} \right)
\end{aligned} \tag{5.4}$$

1389 where $m_b = 4.7$ GeV and $m_t = 172$ GeV are the masses of the bottom and top quarks.

1390 5.2.2 Pythia

1391 For the signal samples (SM and BSM) we simply turn off all other decays except $h \rightarrow b\bar{b}$ therefore forcing
1392 the Higgs to decay to a pair of b quarks leading to the desired final state with four b quarks. All other
1393 settings are not altered with respect to their default configuration. For the BSM samples, this implies that
1394 the coupling of the SM Higgs boson to the b quarks is set to its SM value.

1395 For the $jj + 0/1/2$ and $t\bar{t} + 0/1/2 j$ samples we have to perform jet matching because we require
1396 additional jets at the level of the matrix element. In addition to the partons generated in MadGraph
1397 and that can produce a jet, Pythia may introduce extra jets that are usually soft and collinear (with the
1398 particle from which they were radiated) and result from the showering process. This could lead to the
1399 same process (with the same final states) being counted twice (double counting). Take, for example,
1400 the processes jj and $j jj$ at MadGraph level. It can happen that Pythia generates an extra jet for the
1401 first process but not for the second, leading to both processes having the same final state (three jets).
1402 Each process would then give its independent contribution to the total number of events but because
1403 they simply represent two distinct ways of achieving the same final state they should only be counted
1404 once. The goal of jet matching procedures is to avoid this problem.

1405 The cross section times branching ratio (when applicable), the k-factors and the approximate number

1406 of events for the samples used in the analysis are summarized in table 5.1. The k-factor multiplies the
 1407 cross section times branching ratio in order to reproduce known higher order results. It corresponds only
 1408 to the ratio between the total cross sections and it does not correct for possible differences that might
 1409 exist between the differential cross sections. The number of events changes according to the granularity
 1410 configuration and to the type of jets that were used. The numbers shown should be taken only as an
 1411 order of magnitude.

For the SM signal, $\sigma \times BR$ is given by $\sigma(hh, h \rightarrow b\bar{b}) \times BR(h \rightarrow b\bar{b})$, with $BR(h \rightarrow b\bar{b}) = 0.5824$ for $m_h = 125$ GeV [98]. $\sigma(hh, h \rightarrow b\bar{b})$ is given by:

$$\sigma(hh, h \rightarrow b\bar{b}) = \sigma_{NNLO}(hh) \times 2 \times BR(h \rightarrow b\bar{b}) = 1.22 \text{ pb} \times 2 \times 0.5824 = 1.42 \text{ pb} \quad (5.5)$$

1412 where $\sigma_{NNLO}(hh) = 1.22$ pb follows from Ref. [99] and the factor of 2 is a combinatorial factor that
 1413 indicates that both Higgs bosons can decay to a pair of b quarks. The k-factor is given by $\sigma_{NNLL}/\sigma_{NNLO}$,
 1414 where σ_{NNLL} is calculated according to the prescription given in equation I.7.8 of Ref. [98], with $\delta_t =$
 1415 -0.315 , which yields $\sigma_{NNLL} = 1.33$ pb. Therefore, the k-factor has the value 1.09.

For the BSM signal samples, $\sigma \times BR$ is given by:

$$\sigma \times BR = \sigma(hh)_{\text{MG}} \times (BR(h \rightarrow b\bar{b}))^2 \quad (5.6)$$

1416 where $\sigma(hh)_{\text{MG}}$ is the cross section for Higgs pair production as given by MadGraph. For these samples
 1417 we consider a k-factor of 1.0.

1418 For the remaining samples, $\sigma \times BR$ are the values given by MadGraph. In these samples no decay
 1419 mode is imposed, therefore the branching ratio is one. For the $4b + j(\text{QCD})$ samples, a k-factor of
 1420 two is applied [93] in order to parameterize our ignorance on the QCD irreducible background. For the
 1421 $t\bar{t} + 0/1/2 j$, a k-factor of 1.74 is applied, following Ref. [93].

1422 The parameters used in Pythia 8 can be found in table D.2 in appendix D.

1423 5.2.3 Delphes

1424 It is one of the main goals of this work to evaluate how the analysis sensitivity is influenced by the
 1425 granularity of the hadronic calorimeter. We start from the same MadGraph level samples and pass them
 1426 through Pythia and Delphes changing the settings of the Delphes card that correspond to the HCAL. All
 1427 other detector's parameters were kept unchanged with respect to the FCC default Delphes card. We
 1428 tested five benchmark granularity configurations:

- 1429 1. ATLAS HCAL granularity (as implemented in the standard ATLAS Delphes card);
- 1430 2. Starting from the ATLAS HCAL configuration we increase the granularity in η by a factor of four, in
 1431 the pseudo rapidity range $|\eta| < 1.7$ which corresponds to the TileCal region;
- 1432 3. Starting from the FCC HCAL configuration we decrease the granularity in ϕ by a factor of two, in
 1433 the entire pseudo rapidity range covered by the HCAL.

Table 5.1: Summary of the effective cross sections ($\sigma \times BR$) and k factors of the signal and background samples used in the analysis.

Sample	$\sigma \times BR$ [pb]	k-factor	\sim no. events
$hh \rightarrow b\bar{b}b\bar{b}$ - SM	0.827	1.09	5×10^6
$hh \rightarrow b\bar{b}b\bar{b}$ - DM mediator	0.218	1.0	5×10^6
$hh \rightarrow b\bar{b}b\bar{b}$ - 2HDM type II	0.466	1.0	5×10^6
$4b + j$ (QCD, $200 < p_T^j < 500$)	756.4	2.0	10×10^6
$4b + j$ (QCD, $p_T^j > 500$)	57.71	2.0	10×10^6
$4b + j$ (QCD+EWK)	6.204	1.0	10×10^6
$4b + j$ (EWK)	0.07206	1.0	5×10^6
$jj + 0/1/2 j$ ($500 < H_T < 1000$)	1.64×10^7	1.0	10×10^6
$jj + 0/1/2 j$ ($1000 < H_T < 2000$)	1.67×10^6	1.0	1×10^6
$jj + 0/1/2 j$ ($2000 < H_T < 4000$)	1.32×10^5	1.0	1×10^6
$jj + 0/1/2 j$ ($4000 < H_T < 7200$)	7.32×10^3	1.0	1×10^6
$jj + 0/1/2 j$ ($7200 < H_T < 15000$)	4.75×10^2	1.0	1×10^6
$jj + 0/1/2 j$ ($15000 < H_T < 25000$)	7.35	1.0	1×10^6
$jj + 0/1/2 j$ ($25000 < H_T < 35000$)	0.176	1.0	5×10^5
$jj + 0/1/2 j$ ($35000 < H_T < 100000$)	0.00765	1.0	3×10^5
$t\bar{t} + 0/1/2 j$	4.31×10^4	1.74	5×10^6

- 1434 4. FCC HCAL default granularity (as implemented in the standard FCC Delphes card);
 1435 5. Starting from the FCC HCAL configuration we increase the granularity in η and in ϕ by a factor of
 1436 two, in the entire pseudo rapidity range covered by the HCAL.

1437 The granularities of these five configurations are summarized in table 5.2. The values that are shown,
 1438 as well as the corresponding pseudorapidity regions, are exactly what is implemented in Delphes.

1439 In addition, we also passed the same generator level samples through the default ATLAS detector
 1440 simulation in Delphes. The HCAL granularity is the one that is indicated in the second row of table 5.2
 1441 but the other detector parameters, such as the radius, magnetic field, tracking resolutions are the ones
 1442 that are implemented in the default ATLAS Delphes card. This additional detector configuration gives
 1443 us an extra point in the space of parameters that we are trying to explore. Furthermore, in a first, very
 1444 crude, approximation, it allow us to compare the results obtained at $\sqrt{s} = 100$ TeV to the ones obtained
 1445 at $\sqrt{s} = 13$ TeV by ATLAS. For completion we summarize, in table 5.3, the values of some key detector
 1446 parameters as implemented in Delphes for the ATLAS and FCC-hh detectors. The magnetic field is
 1447 twice as strong for the FCC-hh. The charged hadrons tracking efficiency and the HCAL resolution are
 1448 fairly similar between the two detector configurations.

Table 5.2: Summary of the benchmark granularity configurations of the HCAL.

Configuration	$\Delta\eta \times \Delta\phi$	η range
1 (ATLAS HCAL)	0.1×0.1	$ \eta < 2.5$
	0.2×0.2	$2.5 < \eta < 5.0$
2 (ATLAS HCAL $\eta \times 4$)	0.025×0.1	$ \eta < 1.7$
	0.1×0.1	$1.7 < \eta < 2.5$
3 (FCC HCAL $\phi/2$)	0.2×0.2	$2.5 < \eta < 5.0$
	0.025×0.05	$ \eta < 2.5$
4 (FCC HCAL)	0.05×0.1	$2.5 < \eta < 6.0$
	0.025×0.025	$ \eta < 2.5$
5 (FCC HCAL $\eta, \phi \times 2$)	0.05×0.05	$2.5 < \eta < 6.0$
	0.0125×0.0125	$ \eta < 2.5$
	0.025×0.025	$2.5 < \eta < 6.0$

Table 5.3: Summary of some key detector parameters for the FCC-hh and ATLAS detectors.

Parameter	FCC-hh	ATLAS
Radius of magnetic field coverage [m]	1.5	1.15
Half length [m]	5	3.51
Magnetic field [T]	4	2
Charged hadrons tracking efficiency	90% for $2.5 < \eta < 4.0$, $p_T > 1.0$	85% for $1.5 < \eta < 2.5$, $p_T > 1.0$
HCAL resolution	$\sqrt{E^2(0.03)^2 + E(0.60)^2}$ for $1.7 < \eta < 4.0$	$\sqrt{E^2(0.05)^2 + E(0.706)^2}$ for $1.7 < \eta < 3.2$

¹⁴⁴⁹ Chapter 6

¹⁴⁵⁰ Analysis

¹⁴⁵¹ 6.1 Overview of the $hh \rightarrow b\bar{b}b\bar{b}$ channel

¹⁴⁵² For the SM Higgs, with a mass around 125 GeV, the branching ratio of the $hh \rightarrow b\bar{b}b\bar{b}$ decay is ap-
¹⁴⁵³ proximately 33.6%, making it the most probable decay for Higgs pairs, as is illustrated in figure 6.1(a).
¹⁴⁵⁴ However, in this channel, the main background is QCD multijet production that has a cross section sev-
¹⁴⁵⁵ eral orders of magnitude larger than di-Higgs production in the SM, as table 5.1 shows. Nonetheless,
¹⁴⁵⁶ the jet p_T distributions in this background have a very large yield close to zero and then fall very steeply
¹⁴⁵⁷ while the signal has a much larger tail to high values of p_T . This indicates that searches targeting the
¹⁴⁵⁸ boosted kinematic regime may be the key to measure $hh \rightarrow b\bar{b}b\bar{b}$ using inclusive production.

¹⁴⁵⁹ In this work we target the boosted regime. In this kinematic region, the final state of the signal is
¹⁴⁶⁰ characterized by two jets with a large radius parameter, each containing the two b quarks originated
¹⁴⁶¹ from the decay of one of the Higgs bosons, as figure 6.1(b) illustrates. Extra jets are also expected to
¹⁴⁶² be reconstructed as a consequence of QCD radiation.

¹⁴⁶³ The analysis presented here is performed using the Monte-Carlo samples described in chapter 5. All
¹⁴⁶⁴ samples assume $m_h = 125$ GeV. The event selection criteria are designed to optimize the significance,
¹⁴⁶⁵ given by S/\sqrt{B} , where S and B represent the number of signal and background events, respectively.

¹⁴⁶⁶ 6.1.1 Event pre-selection

¹⁴⁶⁷ We start by applying very simple and loose cuts that target events consistent with the boosted topology.
¹⁴⁶⁸ Jets are reconstructed with the anti- k_T algorithm with a radius parameter $R = 0.8$. They are recon-
¹⁴⁶⁹ structed from particle flow objects or calorimeter towers only. Both approaches were explored in this
¹⁴⁷⁰ analysis.

¹⁴⁷¹ We require at least two b-tagged $R = 0.8$ jets which corresponds to at least four b-tagged subjets,
¹⁴⁷² at least two in each $R = 0.8$ jet. The subjets are found through the soft drop mass technique that was
¹⁴⁷³ described in section 3.3.2. The leading and sub leading jets must have $p_T \geq 200$ GeV in order for the
¹⁴⁷⁴ event to be accepted. From Eq. 3.4, a Higgs boson with, e.g., $p_T = 200$ GeV leads to a pair of b quarks
¹⁴⁷⁵ with $\Delta R \sim \frac{2m}{p_T} = 1.25$. Therefore, considering jets with $R = 0.8$ and $p_T \geq 200$ GeV is a reasonable

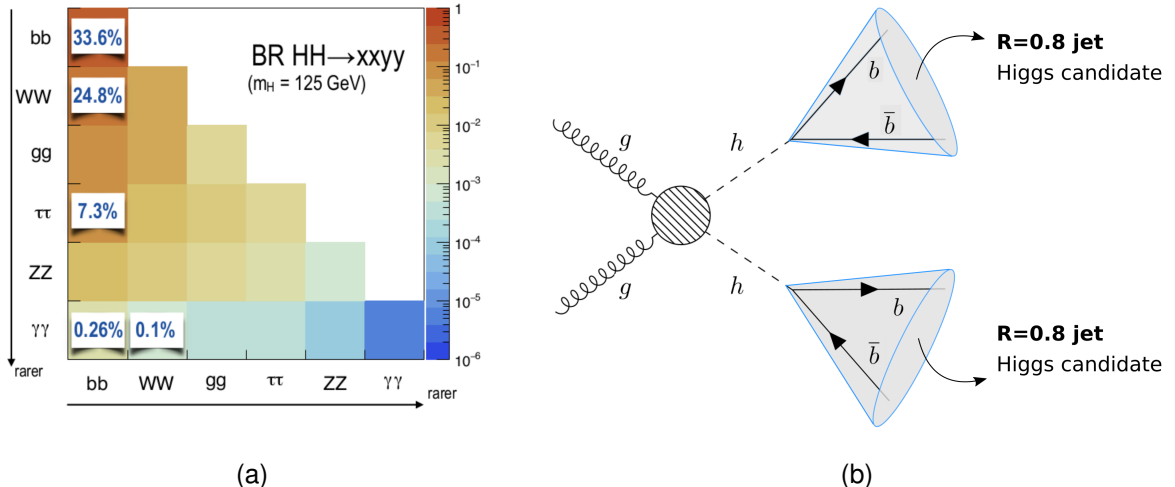


Figure 6.1: (a) Higgs pairs branching ratios, (b) event topology targeted by a boosted analysis.

choice. For a more complete description about the jet radius see appendix A. Due to the b-tagging parameterization (described in detail in section 6.2.1), there is a natural cutoff at $|\eta| = 4$ so we do not place any additional cut in η . From now on, these cuts are referred to as pre-selection cuts.

After the pre-selection cuts we can plot all the relevant distributions that allow us to characterize the signal and background events. These are shown in the next two sections. In addition, these distributions provide a first insight into the discriminating power of the kinematic and substructure variables that are explored.

6.1.2 Signal characterization

The cross section for di-Higgs inclusive production from pp collisions at $\sqrt{s} = 100$ TeV is 1.22 pb [99]. This value is computed at NNLO accuracy. The dominant process is gluon-gluon fusion that has been extensively discussed in section 2.1.1. The signal process comprehends the di-Higgs inclusive production and the $hh \rightarrow b\bar{b}b\bar{b}$ subsequent decays. The total process cross section amounts to approximately 0.9 pb . This number includes the branching ratio and a k-factor to account for known NNLL results. This is described in detail in section 5.2.2. For an integrated luminosity of 30 ab^{-1} of proton-proton collisions at $\sqrt{s} = 100$ TeV we expect 2.7×10^7 events.

The Higgs candidates are reconstructed using large R jets that can be directly measured using information from the calorimeters and tracking systems. Figure 6.2(a) shows the $\Delta\phi$ between the two leading jets (Higgs candidates), $\Delta\phi(hh)$. For a large fraction of the signal events (red curve) $\Delta\phi(hh) \sim \pi$ which indicates that the jets are produced back-to-back in the transverse plane. There is also a small fraction of events for which the jets have $\Delta\phi(hh) \sim 1$. For these events there must be at least a third jet that balances the momentum of the jet pair.

Each wide jet is expected to be consistent with having two subjets associated with the two b quarks from the $h \rightarrow b\bar{b}$ decay. In the Higgs rest frame, the two subjets are produced back-to-back conserving momentum. In the laboratory frame, the ΔR between the subjets depends on the momentum of the

1500 Higgs boson, with larger ΔR corresponding to Higgs bosons with a lower momentum. This correlation
1501 between the ΔR between the subjets of the leading Higgs candidate ($\Delta R(b\bar{b})$) and its momentum
1502 ($p_T(h_1)$) is shown in figure 6.2(b).

1503 The p_T distributions of the leading and sub leading jets (Higgs candidates) are shown in figures
1504 6.5(a) and 6.5(b), respectively. The histograms are normalized to unit area in order to allow for shape
1505 comparison between them. For the leading jet, the signal p_T spectrum peaks at approximately 350 GeV
1506 and has a long tail for large values of p_T , in particular, longer than any of the backgrounds, at least up to
1507 $p_T \sim 1000$ GeV. For the sub leading jet the spectrum is softer, as expected, but the tail of the distribution
1508 is still longer than for any of the backgrounds. These distributions show that the signal process produces
1509 jets with larger transverse momenta than the jets produced by the background processes which indicates
1510 that a boosted analysis might perform well.

1511 The η distribution of the leading jet is shown in figure 6.6(a). This distribution is limited to $|\eta| < 4$
1512 because the b-tagging efficiency goes to zero for $|\eta| > 4$ (see section 6.2.1 for more details). The
1513 number of events decreases as we go to larger values of η which is due to the detector's acceptance.
1514 The η distribution of the sub leading jet is very similar to this one so we abstain from showing it here.

1515 The softdrop mass distribution of the leading jet is shown in figure 6.6(b). For the signal (red curve)
1516 there is a clear peak at approximately 120 GeV which corresponds to the SM Higgs boson mass peak.
1517 The peak is quite broad which means the mass resolution in this channel is not very good. On the one
1518 hand, this is because we are using large- R jets to reconstruct the Higgs candidates. These objects have
1519 a worse mass resolution than other cleaner objects such as photons or muons. On the other hand, the
1520 cuts applied before plotting these distributions are very loose. As we place additional cuts the mass
1521 peak can be made slightly narrower. Another interesting feature of the signal mass spectrum is the
1522 existence of a peak close to zero. The explanation is the following: some jets do not contain both b
1523 quarks from the Higgs decay such that when applying the mass drop procedure only one b quark with a
1524 mass of approximately 5 GeV remains inside the jet, creating the peak at lower masses. A more detailed
1525 discussion, as well as a plot that supports this interpretation, can be found in appendix C.

1526 In addition to the basic kinematic distributions that we have just described, there are a multitude of
1527 other variables one can look at. Here we show the $\Delta\eta$ between the Higgs pairs, figure 6.7(a), and the
1528 τ_{21} variable for the leading Higgs candidate, figure 6.7(b). The first distribution shows that the Higgs pair
1529 tends to have a $\Delta\eta$ close to zero, which indicates that the pair is highly boosted in the longitudinal plane.
1530 The τ_{21} distribution shows that for the signal this variable takes values close to zero which means that
1531 the jet is consistent with having two subjets.

1532 6.1.3 Backgrounds

1533 The relevant backgrounds for this analysis are QCD multijet production, $t\bar{t}$ and $b\bar{b}b\bar{b}$. Although the $b\bar{b}b\bar{b}$
1534 background is a particular case of a QCD multijet production process we consider it separately because
1535 it constitutes the irreducible background and therefore will have a higher efficiency in the analysis. The
1536 cross sections for these processes are several orders of magnitude larger than the cross section for the

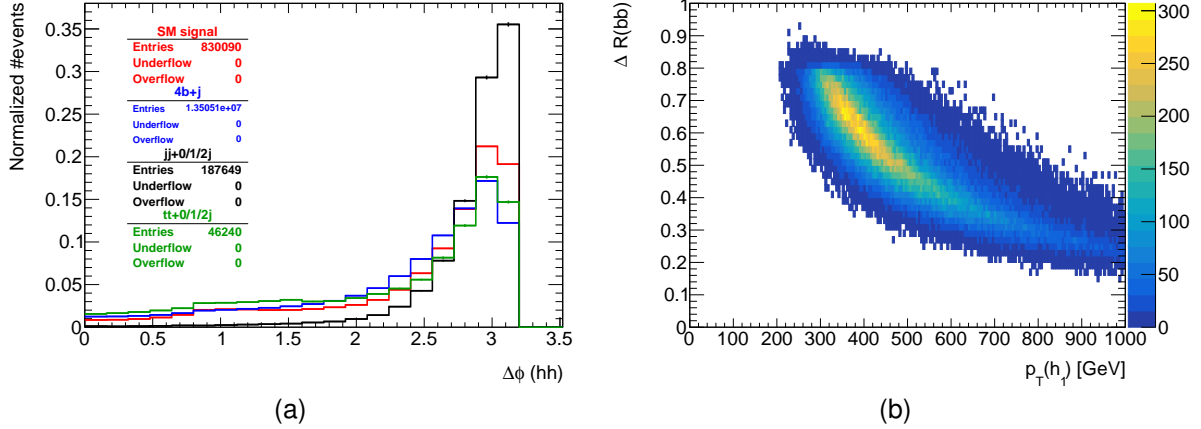


Figure 6.2: (a) $\Delta\phi$ between the Higgs candidates, $\Delta\phi(hh)$, (b) ΔR between the b quarks coming from the decay of the leading Higgs candidate, h_1 . To obtain this plot the cut $|M - 125| < 40$ GeV was applied in addition to the pre-selection cuts.

1537 signal, as table 5.1 shows. In addition, in the case of the $t\bar{t}$ background, the event topology is expected
 1538 to be similar to the signal because it also consists in the production of a pair of particles with the same
 1539 mass.

1540 The assumption that QCD multijet production and $t\bar{t}$ are the two main backgrounds is corroborated by
 1541 the ATLAS di-Higgs search performed in the same channel, where these backgrounds were found to be
 1542 the dominant ones. All other sources of backgrounds, including processes involving Higgs bosons, are
 1543 found to be negligible [65]. In appendix B we discuss and evaluate the importance of some backgrounds
 1544 that include Higgs bosons in our analysis.

1545 Figure 6.3 shows examples of LO Feynman diagrams that contribute to $4b + j$ (left), three (middle)
 1546 and four (right) light jets production. The $b\bar{b}b\bar{b}$ background is generated with an extra light jet at generator
 1547 level, as discussed in chapter 5. This jet boosts the four b quarks and has a minimum p_T of 200 GeV. This
 1548 increases the probability of two b quarks being reconstructed as single large- R jet therefore emulating
 1549 the signal's final state signature, i.e., high p_T jets compatible with a two-prong substructure. The QCD
 1550 $4b + j$ sample with $(200 < p_T < 500)$ GeV has a cross section of approximately 756 pb. In addition, as
 1551 explained in section 5.2.2, we multiply this cross section by a k-factor of 2, which yields a total cross
 1552 section of approximately 1.5×10^3 pb. The cross section is a lot smaller for the other $4b + j$ QCD sample
 1553 as well as for the samples that include both QCD and electroweak contributions, as expected.

1554 The QCD multijet background consists of two, three and four jet events (represented as $jj + 0/1/2 j$),
 1555 at generator level. The jets can originate from light and b quarks and from gluons. A jet matching
 1556 procedure is implemented in Pythia in order to avoid double counting. Due to non-zero mistagging
 1557 probabilities, light and c jets can be identified as b jets. Although these probabilities are relatively small
 1558 when compared to the b-tagging efficiency (see section 6.2.1) the cross section of multijet processes is
 1559 very large such that this background becomes dominant. The $jj + 0/1/2 j$ sample with $(500 < H_T <$
 1560 $1000)$ GeV has a cross section of the order of 10^7 pb. As anticipated, the p_T spectrum of the multijet
 1561 background is a lot softer than for the signal and remaining backgrounds, as it is shown in figures 6.5(a)

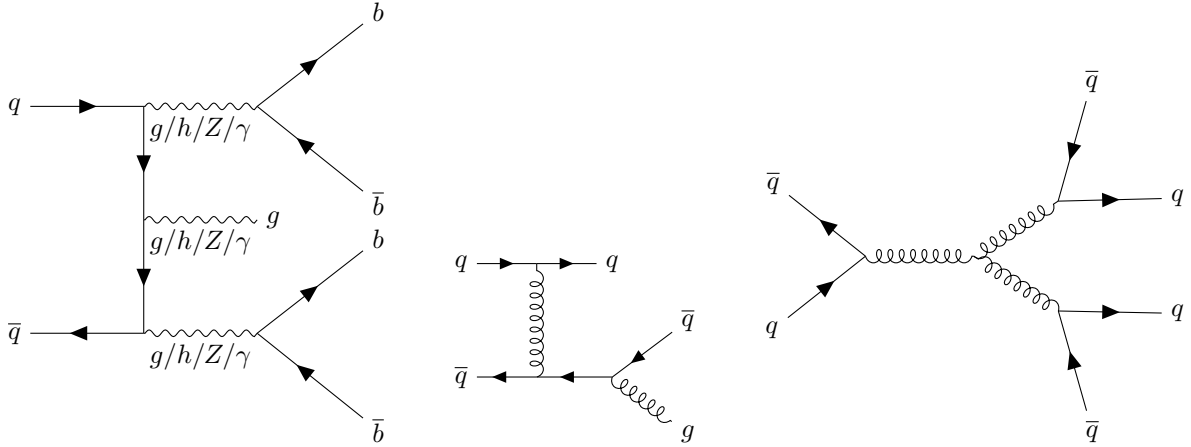


Figure 6.3: Example of diagrams that contribute to the QCD multijet background: five final state jets, four of which are b-jets (left), three final state jets (middle) and four final state jets (right). Here, q stands for a light quark/jet.

and 6.5(b). In addition, for this background the τ_{21} variable takes values close to one, as it is shown in figure 6.7(b). This indicates that the jets are not consistent with two subjets.

Figure 6.4 shows examples of LO Feynman diagrams that contribute to $t\bar{t}$ production through $q\bar{q}$ (left)

and gg (middle and right) fusion. The $t\bar{t}$ background is simulated with additional zero, one or two jets represented as $t\bar{t} + 0/1/2 j$, at generator level. The extra jets can originate from light and b quarks and from gluons. A jet matching procedure is implemented in Pythia in order to avoid double counting.

The top quark has a very short lifetime, predicted to be 5×10^{-25} s, such that it decays before it can hadronize. This sample is inclusive in the top quark decay modes. However, the most favoured decay

of the top quark is $t \rightarrow Wb$ with a branching ratio close to 96% [100]. Therefore, $t\bar{t}$ events will, most of the times, result in the $W^+W^-b\bar{b}$ final state. We do not specify any decay mode for the W such that

the sample is also inclusive in the W decay modes. The W decays to hadrons ($W^+ \rightarrow q\bar{q}$) and leptons ($W^+ \rightarrow l^+\nu$) with $\text{BR}(W^+ \rightarrow q\bar{q}) \sim 68\%$ and $\text{BR}(W^+ \rightarrow l^+\nu) \sim 10\%$. If one (or both) W bosons

decays to hadrons then there will be additional jets in the final state. These can be b jets (although the probability is very small) or can be misidentified as such. If both W bosons decay to leptons there will

still be at least two b jets in the final state, coming from the $t\bar{t}$ decay. The cross section of the $t\bar{t} + 0/1/2 j$ is approximately 4.3×10^4 pb. As explained in 5.2.2, k-factor of 1.74 is applied which yields a total cross

section of approximately 7.5×10^4 pb.

It is interesting to note that in the softdrop mass plot for the leading Higgs candidate (figure 6.6(b))

the $t\bar{t}$ background (green line) shows a small peak around 170 GeV. In this region, all the decay products of the top quark are contained inside the $R = 0.8$ jet such that the jet mass corresponds to the mass of

the original top quark.

6.2 Analysis strategy

As already discussed, this analysis targets events in which at least two large- R jets are reconstructed.

The jet with the highest momentum is assumed to correspond to the leading Higgs candidate and the jet

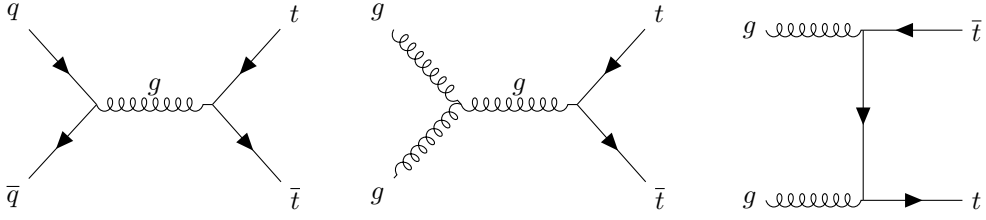


Figure 6.4: Dominant diagrams of $pp \rightarrow t\bar{t}$ at LO.

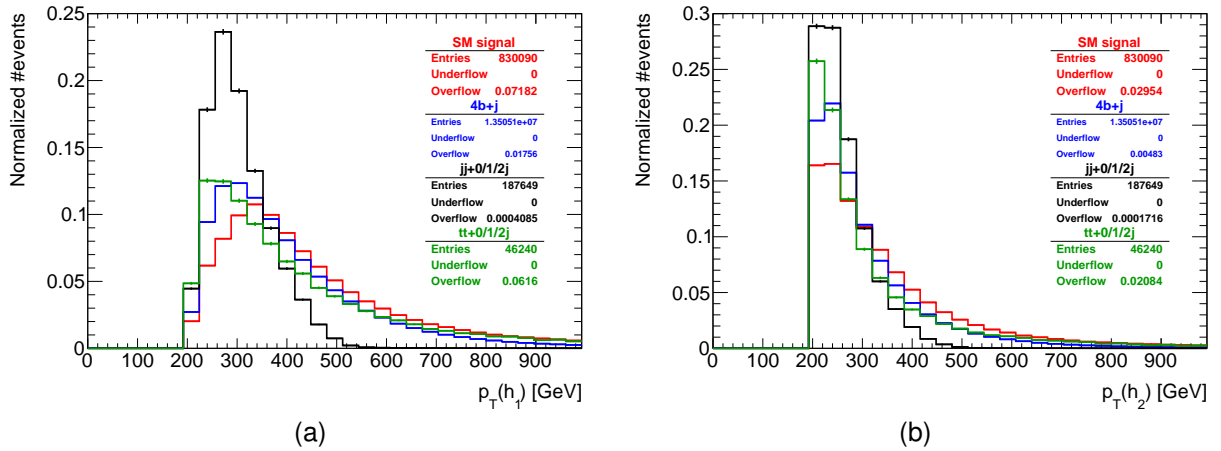


Figure 6.5: p_T distributions for the leading (a) and sub-leading (b) Higgs candidates. The signal is the SM $hh \rightarrow b\bar{b}$ process. The histograms are normalized to unit area.

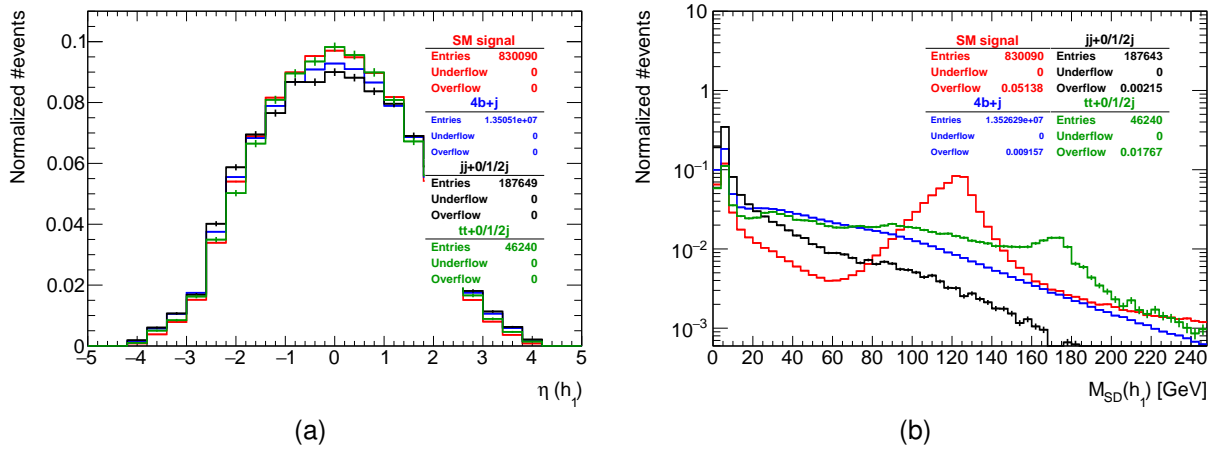


Figure 6.6: η (a) and softdrop mass (b) distributions for the leading Higgs candidate. The signal is the SM $hh \rightarrow b\bar{b}$ process. The histograms are normalized to unit area.

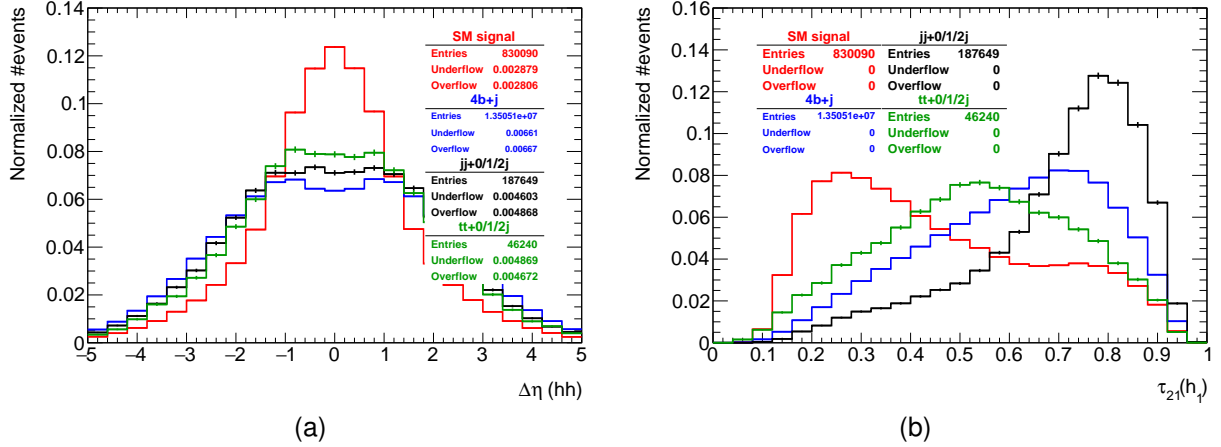


Figure 6.7: Distributions of the $\Delta\eta$ between the Higgs candidates (a) and of the τ_{21} variable for the leading Higgs candidate (b). The histograms are normalized to unit area.

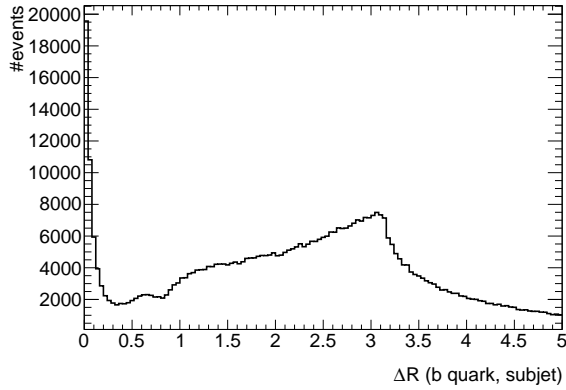


Figure 6.8: Minimum ΔR between b quarks and subjets of the $R = 0.8$ jets.

1586 with the second highest momentum to the sub leading one. Both the leading and sub leading jets must
 1587 be b-tagged in order for the event to be accepted.

1588 The events are reconstructed using particle flow or pure calorimeter jets with $R = 0.8$, clustered
 1589 with the anti- k_T algorithm. We perform the b-tagging of jets using truth level information. Jets with a
 1590 large- R parameter cannot be b-tagged using Delphes default algorithm. The tagging of large R jets is
 1591 an ambiguous task that can be performed in several different ways. Therefore, we implemented our own
 1592 b-tagging algorithm that is described in section 6.2.1.

1593 In this section, we present the baseline analysis based on cuts on kinematic and substructure vari-
 1594 ables. An optimized version of the analysis is also presented and compared to the baseline. The
 1595 optimization is based on plots of the significance (S/\sqrt{B}) as a function of the cut on a given variable.
 1596 We also describe how statistical and systematic uncertainties are estimated.

1597 6.2.1 Implementation of b-tagging

1598 For each jet, the two hardest subjets are found using the mass drop procedure. It might happen that there
 1599 are not two subjets because the algorithm's criteria are not met. In that case, the jet is rejected. For each

Table 6.1: b-Tagging (black), c (blue) and light (red) mistag probabilities as a function of η and p_T of the (sub)jet. The momentum dependent factor, $(1 - p_T/15000)$, is common to the three probabilities.

$\eta \backslash p_T$	$10 < p_T < 500$	$500 < p_T < 15000$
$ \eta < 2.5$	0.85; 0.05 ; 0.01	$(0.85; \textcolor{blue}{0.05}; \textcolor{red}{0.01}) \times (1 - p_T/15000)$
$2.5 < \eta < 4.0$	0.64; 0.03 ; 0.0075	$(0.64; \textcolor{blue}{0.03}; \textcolor{red}{0.0075}) \times (1 - p_T/15000)$

event, we compute the ΔR distance between all b and c quarks with Pythia status equal to 23 [101] and with $p_T > 10$ GeV and each subjet ($\Delta R(\text{subjet,parton})$). Particles with status 23 result directly from the hardest subprocess. We consider that a subjet is matched to a given quark if $\Delta R(\text{subjet,parton}) < 0.3$, as indicated in figure 6.8. If the subjet is matched to at least one b quark, we b-tag the subjet with a given probability. If the subjet is not matched to any b quark but it is matched to at least one c quark we apply a c mistag rate. If the subjet is not matched to any b or c quark we apply a light mis tag rate. The b-tag probability and mistag rates were obtained from the Delphes FCC-hh card. They depend on the momentum of the jet and on its η coordinate. They are summarized in table 6.1. The b-tagging probabilities are given in black and the c and light mis tagging probabilities are given in blue and red, respectively. Note that a jet cannot be b-tagged if $|\eta| > 4$ or if its momentum is smaller than 10 GeV or larger than 15000 GeV.

In terms of the technical implementation, the b-tagging algorithm works as follows: for each subjet we look for a truth-level b quark within $\Delta R = 0.3$ of the subjet and calculate the b-tagging and mistagging efficiencies using the expressions in table 6.1, where p_T and η refer to the subjet. If a b quark is found we generate a random number between 0 and 1. If it smaller than the b-tagging efficiency we consider the subjet to be b-tagged. If the subjet is not b-tagged we look for truth-level c quarks within $\Delta R = 0.3$ of the subjet. If one is found we generate a new random number between 0 and 1 and if the number is smaller than the c mistag probability we consider the subjet to be b-tagged. If the subjet is still not b-tagged we generate a random number between 0 and 1 and consider the subjet b-tagged if the number is smaller than the light mistag probability.

6.2.2 Baseline analysis

The analysis described in this section and in section 6.2.3 were developed using the sample simulated with the default FCC-hh detector implementation. The same event selection was then applied to the samples generated using the different detector configurations. This allows for a straightforward comparison of the results obtained with the different configurations.

As a first step, we implemented a baseline analysis based on rectangular cuts on kinematic and substructure variables. Firstly, we apply cuts on the transverse momenta of the leading and sub leading Higgs candidates, $p_T(h_1)$ and $p_T(h_2)$, and of the Higgs pair, $p_T(hh)$:

$$p_T(h_1) > 400 \text{ GeV}, \quad p_T(h_2) > 350 \text{ GeV}, \quad p_T(hh) > 100 \text{ GeV}. \quad (6.1)$$

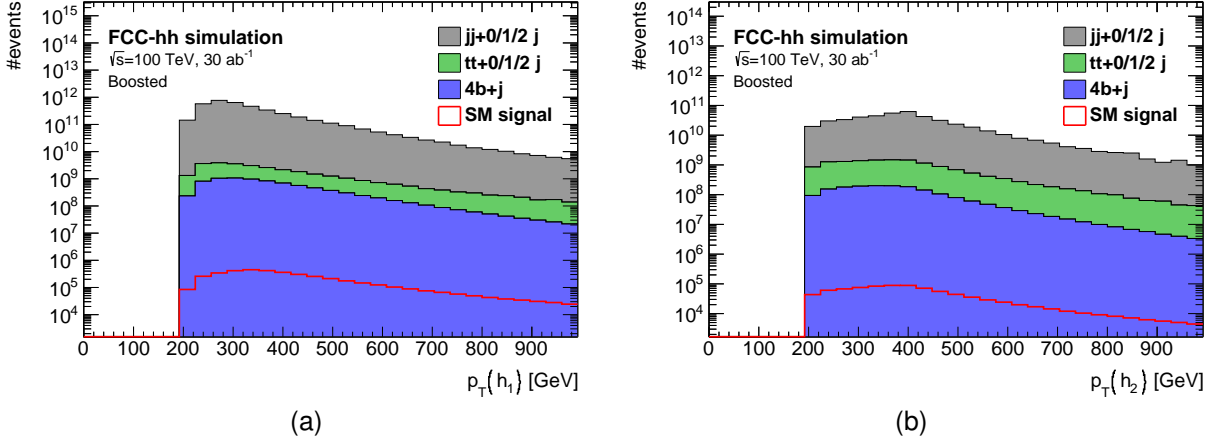


Figure 6.9: p_T distributions for the leading (a) and sub leading Higgs candidates (b). The histograms are normalized to $\mathcal{L} = 30 \text{ ab}^{-1}$.

These cuts follow from the distributions shown in figures 6.9(a), 6.9(b) and 6.10(a) and guarantee that we are choosing events for which the Higgs candidates are sufficiently boosted. In addition, a high threshold for the p_T of the jets suppresses $t\bar{t}$ events because the decay products of the top quark are reconstructed in a single jet.

From figure 6.10(b) we then apply a cut on the τ_{21} of the leading Higgs candidate to select jets that are more compatible with a two-prong structure:

$$\tau_{21}(h_1) < 0.55. \quad (6.2)$$

The cut on this variable works as a Higgs tagging method. Therefore we apply the same cut on the τ_{21} of the sub leading Higgs candidate although that does not necessarily follow from the distribution of τ_{21} for the sub leading Higgs candidate (which can be found in figure F.1 in appendix F). Then, from the distribution in figure 6.11(a), we place a cut on the second Fox-Wolfram momentum (defined in section 3.3.1) of the leading Higgs candidate, $H_2(h_1)$:

$$H_2(h_1) > 0.2 \quad (6.3)$$

This substructure variable is particularly interesting because it helps suppress the $t\bar{t}$ background.

Finally, based on the distribution shown in figure 6.11(b), we apply a cut on the softdrop mass of both Higgs candidates, $M_{SD}(h_1, h_2)$. The distribution of $M_{SD}(h_2)$ is similar to this one so we do not show it here. This cut is placed in a window around the nominal SM Higgs mass:

$$(100 \leq M_{SD}(h_1, h_2) \leq 135) \text{ GeV}. \quad (6.4)$$

Using this analysis, we achieve a significance, S/\sqrt{B} , of $5.1 \pm 0.5 \text{ (stat.)}^{+2.5}_{-1.8} \text{ (sys.)}$ ($1.62 \pm 0.16 \text{ (stat.)}^{+0.8}_{-0.6} \text{ (sys.)}$) for an integrated luminosity of $30 (3) \text{ ab}^{-1}$.

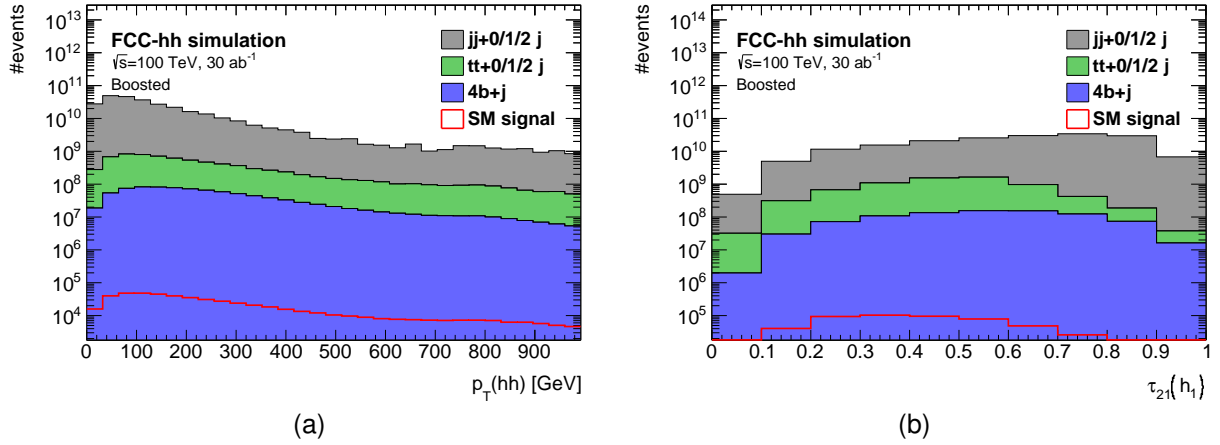


Figure 6.10: (a) p_T distribution for the Higgs pair, (b) τ_{21} variable for the leading Higgs candidate. The histograms are normalized to $\mathcal{L} = 30 \text{ ab}^{-1}$.

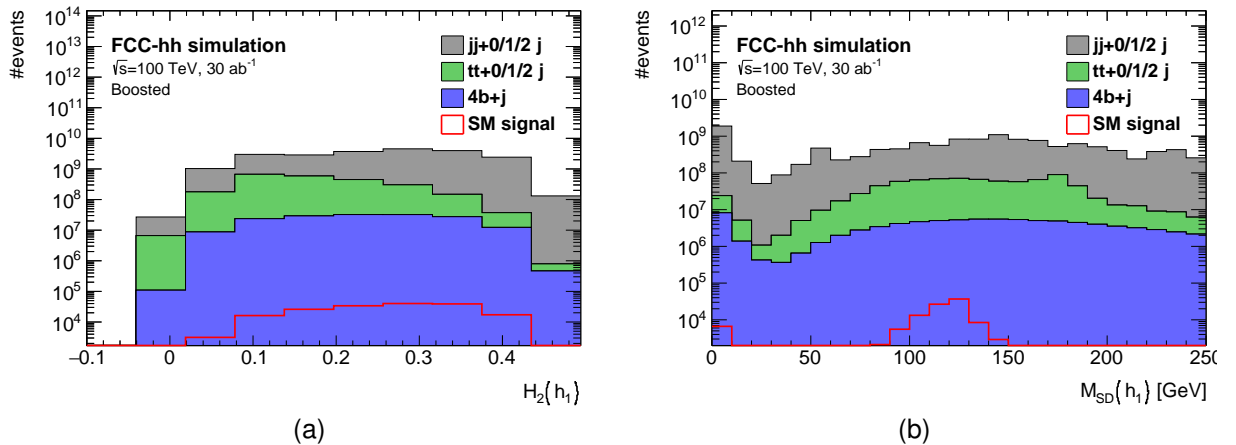


Figure 6.11: (a) H_2 variable for the leading Higgs candidate, (b) softdrop mass distribution for the leading Higgs candidate. The histograms are normalized to $\mathcal{L} = 30 \text{ ab}^{-1}$.

1632 **6.2.3 Optimization**

The first approach to the optimization consists in placing successive cuts in the most relevant kinematic variables. The value of each cut is chosen in order to optimize the significance after that cut. As for the baseline analysis we start by looking at the transverse momenta of the leading and sub leading Higgs candidates. After the pre-selection cuts are applied, we scan the histograms of the p_T of the leading Higgs candidate for signal and backgrounds by placing a lower cut on this variable. For each value of the cut we integrate upwards in order to obtain the expected number of signal and background events after the cut. Using these numbers we calculate the significance, S/\sqrt{B} . The significance as a function of the lower cut on $p_T(h_1)$ is shown in figure 6.12(a). Based on this plot we choose the cut:

$$p_T(h_1) > 300 \text{ GeV}. \quad (6.5)$$

After placing the cut on $p_T(h_1)$ we do the same plot for the p_T of the sub leading Higgs candidate and of the Higgs pair. These are shown in figures 6.12(b) and 6.13(a), respectively. From figure 6.12(b) we see that a cut on $p_T(h_2)$ above 200 GeV is not favorable. Therefore, we do not apply any other cut on this variable. Based on figure 6.13(a) we choose the cut:

$$p_T(hh) > 100 \text{ GeV}. \quad (6.6)$$

Following the cuts on the momenta we place a cut on the τ_{21} variable for both Higgs candidates. From all the variables considered during the optimization process this was the one that lead to the highest increase in the significance. From the definition of the τ_{21} variable we expect the signal to take lower values than the background. Therefore we optimize the cut on this variable by placing an upper cut and integrating the distribution below that cut. The plot is shown in figure 6.13(b). From this plot we place the following cut on the τ_{21} of the leading Higgs candidate:

$$\tau_{21}(h_1) < 0.4. \quad (6.7)$$

1633 We apply exactly the same cut on the τ_{21} of the sub leading Higgs candidate. This guarantees that both jets are consistent with having two subjets and therefore are more likely to originate from the decay of a 1634 Higgs boson.

Next we apply cuts on the $\Delta\eta$ between the Higgs candidates and on the second Fox-Wolfram momentum of the leading Higgs candidates, in this order:

$$|\Delta\eta(hh)| < 1.5 \quad H_2(h_1) > 0.2. \quad (6.8)$$

1636 These cuts follow from the plots on figures 6.14(a) and 6.14(b). The optimization plot for $\Delta\eta(hh)$ is 1637 obtained placing a cut in a window around zero which follows directly from the shape of the distributions 1638 in figure 6.7(a). For the $H_2(h_1)$ variable the cut is placed on the lower value.

1639 Finally we apply the mass cuts on the leading and sub leading Higgs candidates. These are the

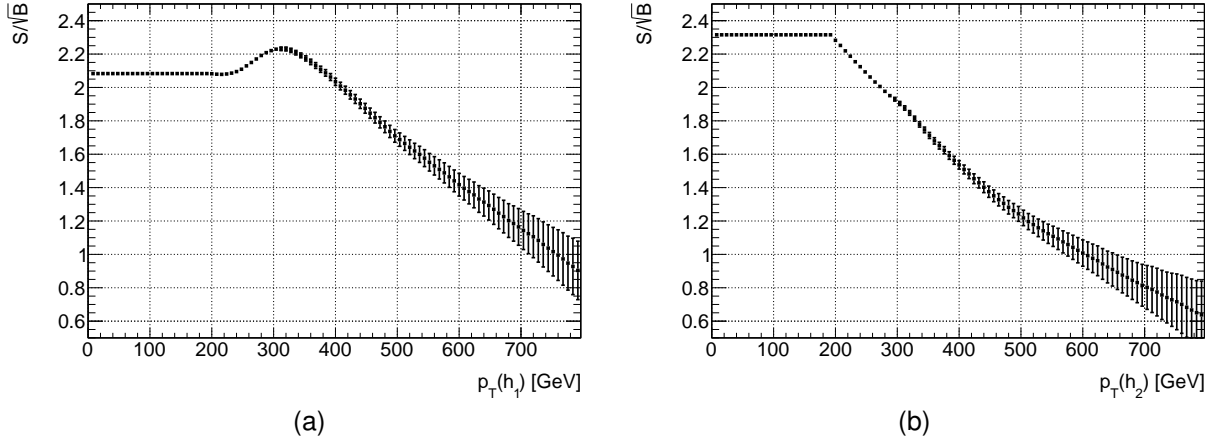


Figure 6.12: S/\sqrt{B} as a function of the cut on the p_T of the leading Higgs candidate, $p_T(h_1)$ (a) after the pre-selection cuts and of the sub leading Higgs candidate, $p_T(h_2)$ (b) after the cut on $p_T(h_1)$.

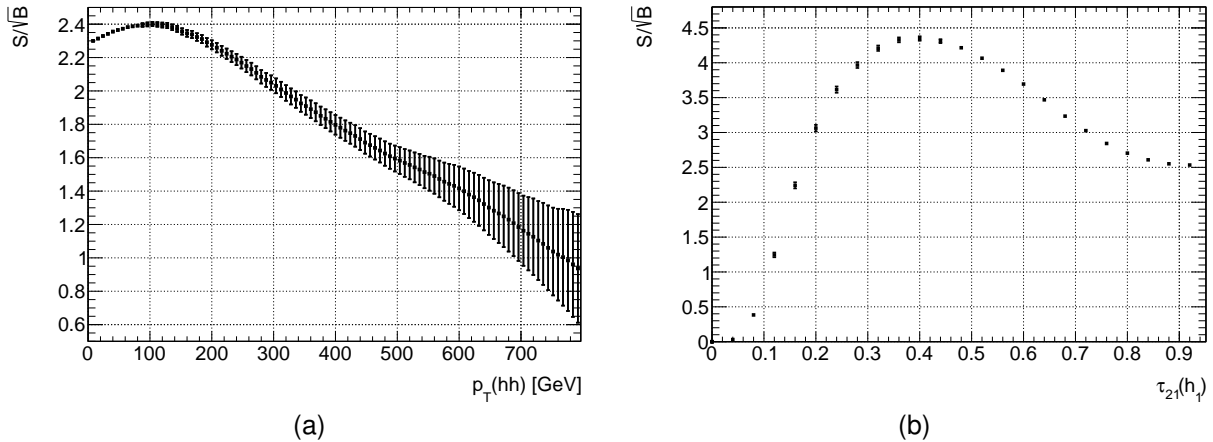


Figure 6.13: S/\sqrt{B} as a function of the cut on the p_T of the Higgs pair, $p_T(hh)$ (a) after the cut on $p_T(h_1)$ and as a function of the τ_{21} variable for leading Higgs candidate, $\tau_{21}(h_1)$ (b) after the cut on $p_T(hh)$.

1640 same that were applied in the baseline analysis.

1641 Using the optimized analysis we obtain a significance, S/\sqrt{B} , of 8.8 ± 1.6 (stat.) $^{+4.1}_{-3.0}$ (sys.) ($2.8 \pm$
 1642 0.5 (stat.) $^{+1.3}_{-1.0}$ (sys.)) for an integrated luminosity of 30 (3) ab^{-1} . This corresponds to an improve-
 1643 ment of approximately 70% with respect to the baseline analysis. This percentage is calculated as
 1644 $\left(((S/\sqrt{B})_{\text{opt.}} - (S/\sqrt{B})_{\text{base.}}) / (S/\sqrt{B})_{\text{base.}} \right) \times 100$.

1645 6.2.4 Handling of uncertainties

1646 Statistical uncertainties

For challenging analyses such as this one, the backgrounds usually have a much larger cross section than the signal meaning that we need a lot of Monte Carlo events to properly simulate them. Most of the times it is not feasible to generate as much events as we would need for a given luminosity. This is the case with this work, in particular because we are targeting very high luminosities (of the order of tens

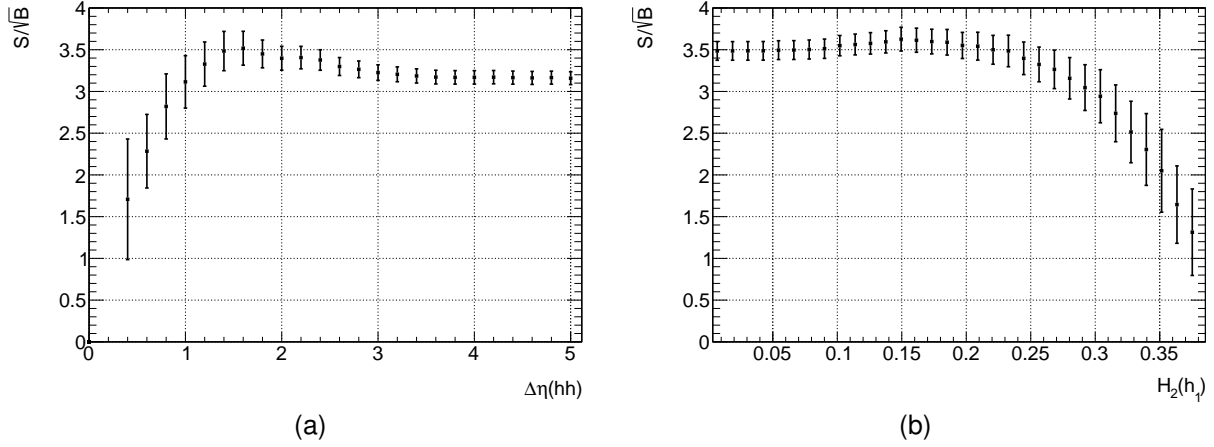


Figure 6.14: S/\sqrt{B} as a function of the cut on the $\Delta\eta$ between the Higgs candidates, $\Delta\eta(hh)$ (a) after the cuts on the transverse momenta and on the τ_{21} variables and as a function of the second Fox-Wolfram momentum for the leading Higgs candidate, $H_l(h_1)$ (b) after the cuts on the transverse momentums, τ_{21} and $\Delta\eta$.

of ab^{-1}). Take for example the multijet sample with $500 < H_T < 1000$, where H_T is the scalar sum of the p_T of all partons at generator level. The cross section is approximately 10^7 pb which means that we expect a total of 3×10^{14} events for an integrated luminosity of 30 ab^{-1} . It is not feasible, within the time frame of this work and with the available computational resources, to generate this number of events. Therefore, we apply a weight, w , to each event given by:

$$w = \frac{\mathcal{L} \times \sigma}{N} \quad (6.9)$$

where \mathcal{L} is the target integrated luminosity, σ is the cross section of the sample and N is the number of MC events generated.

If we assume that the number of events follows a Poisson distribution then the standard deviation (or uncertainty) is given by \sqrt{N} where N is the mean number of events. In order to normalize the number of events to a given luminosity we need to multiply the mean value and the uncertainty by the respective weight such that the number of normalized events, including the uncertainty, $N_{\text{norm}} \pm \Delta N_{\text{norm}}$, is given by:

$$N_{\text{norm}} \pm \Delta N_{\text{norm}} = w \times \left(N \pm \sqrt{N} \right). \quad (6.10)$$

ΔN_{norm} can then be used in standard error propagation to compute the statistical uncertainty associated with any expression, in particular, with S/\sqrt{B} . The statistical error associated with S/\sqrt{B} is given by:

$$\left(\Delta \frac{S}{\sqrt{B}} \right)_{\text{stat.}}^2 = \left| \frac{1}{\sqrt{B}} \right|^2 (\Delta S)^2 + \left| -\frac{S}{B^{3/2}} \right|^2 (\Delta B)^2 \quad (6.11)$$

where ΔS and ΔB are the uncertainties associated with the number of signal and background events. ΔB is given by:

$$(\Delta B)^2 = \sum_i (\Delta B_i)^2 \quad (6.12)$$

1649 where the index i runs over all independent backgrounds.

1650 Systematic uncertainties

1651 Systematic uncertainties are usually related to the detector specificities and object reconstruction tech-
1652 niques, which makes them difficult to list and quantify for a detector that is not yet built. Nonetheless,
1653 we can use the numbers for the systematic uncertainties that are reported in existing searches for
1654 $pp \rightarrow hh \rightarrow b\bar{b}b\bar{b}$ using the ATLAS detector.

1655 When requiring four b-tags, the largest uncertainty affecting the signal is the the b-tagging uncertainty
1656 (table 6 of Ref. [102]). It is of the order of 30%. For the background, the largest uncertainty comes from
1657 the estimation of its yield and shape, according to the same reference. The reported value is 16%.
1658 However, a study performed by the FCC study group [103] considers more conservative values for the
1659 uncertainties on the $t\bar{t}$ and QCD di-jet backgrounds normalizations. The reported values are 20% for $t\bar{t}$
1660 and 50% for di-jet production. In this study we use these values.

1661 To estimated the b-tagging systematic uncertainty, the number of signal events after all the analysis
1662 cuts is varied by 30% up and down. This leads to an upper (lower) bound in the significance of 6.6 (3.6),
1663 considering the baseline analysis.

1664 The background normalization uncertainties are implemented by increasing and decreasing the k-
1665 factor of each background by the corresponding percentage, with respect to what is given in table 5.1.
1666 We vary the k-factors of the QCD multijet ($4b + j$ and $jj + 0/1/2 j$) and of the $t\bar{t}$ backgrounds individually.
1667 For the $4b + j$ and $jj + 0/1/2 j$ backgrounds we consider the same uncertainty of 50% and the variations
1668 are done simultaneously for both. This leads to an upper (lower) bound in the significance of 7.1 (4.2).
1669 For the $t\bar{t}$ background we consider an uncertainty of 20% which leads to an upper (lower) bound in the
1670 significance of 5.13 (5.09). These numbers refer to the baseline analysis.

We assume that the three sources of systematic uncertainty are uncorrelated and therefore the respective variations can be added in quadrature. The statistical error is also added in quadrature. Therefore, the total uncertainty is given by:

$$\left(\Delta \frac{S}{\sqrt{B}} \right)_{\text{sys.+stat.}}^2 = (\delta_{\text{b-tag}})^2 + (\delta_{\text{QCD bkg.}})^2 + (\delta_{t\bar{t} \text{ bkg.}})^2 + (\delta_{\text{stat.}})^2 \quad (6.13)$$

1671 where $\delta_{\text{b-tag}}$, $\delta_{\text{QCD bkg.}}$ and $\delta_{t\bar{t} \text{ bkg.}}$ are the variations with respect to the nominal value of the significance
1672 caused by the b-tagging uncertainty and by the uncertainties on the normalization of the QCD multijet
1673 and $t\bar{t}$ backgrounds, respectively. $\delta_{\text{stat.}}$ is the statistical uncertainty, given by Eq. 6.11.

1674 6.2.5 Trigger discussion

1675 In the previous discussions regarding the baseline and optimized analysis no trigger requirements were
1676 taken into account. We now review the trigger requirements that had to be fulfilled in the analysis
1677 performed by ATLAS and discuss where do the analyses we designed stand with respect to those
1678 requirements.

1679 In Ref. [102], the event selection requires the existence of at least two anti- k_T $R = 1.0$ jets with
1680 $p_T > 250$ GeV, $|\eta| < 2.0$ and $m_J > 50$ GeV. In addition, the leading jet must have $p_T > 450$ GeV to
1681 guarantee 100% trigger efficiency.

1682 We require at least two anti- k_T $R = 0.8$ jets with $p_T > 200$ GeV. In the baseline analysis, we require
1683 that the leading jet has $p_T > 400$ GeV. These p_T thresholds are compatible to the ones used in the
1684 ATLAS analysis mainly when we consider that the radius of the jets is slightly smaller and therefore the
1685 p_T threshold can also be lower. We do not consider any cuts on the pseudorapidity or mass of the jets.
1686 However, we do require that the sub leading jet has $p_T > 300$ GeV and that the Higgs pair has $p_T > 100$
1687 GeV which would help lower the rate.

1688 In the optimized analysis, however, the p_T cuts are significantly looser: the leading jet must have
1689 $p_T > 300$ GeV and the Higgs pair must have $p_T > 100$ GeV. This could indicate that although the
1690 optimized analysis gives a better significance, tighter cuts might have to be applied in order to fulfill the
1691 trigger requirements, therefore reducing the significance.

1692 Chapter 7

1693 Results

1694 In this chapter we describe the main results of the search for $hh \rightarrow b\bar{b}b\bar{b}$ at the FCC-hh and compare
1695 them with the results obtained using the ATLAS default detector simulation (section 7.1). In section
1696 7.2 we show how the significance of the analysis varies as a function of the granularity of the HCAL
1697 and/or the detector configuration. We also compare the results obtained using particle flow and pure
1698 calorimeter jets.

1699 7.1 Di-Higgs discovery potential at the FCC-hh

1700 The event selection of the optimized analysis for the search for $hh \rightarrow b\bar{b}b\bar{b}$ at the FCC-hh with the
1701 baseline detector design is summarized in tables 7.1 and 7.2 for the signal samples (SM, DM mediator
1702 and type II 2HDM) and for the background samples ($4b + j$, $jj + 0/1/2j$ and $t\bar{t}$), respectively.

1703 From table 7.1, we see that for the BSM models the signal efficiency is higher than for the SM. It
1704 varies from 0.446% for the SM, to 0.487% for the DM mediator model and to 1.666% for the type II 2HDM.
1705 This is due to the existence of heavy new particles in the BSM models that lead to the production of
1706 highly boosted SM Higgs pairs.

Considering the SM production of Higgs pairs, the achieved significance is

$$S/\sqrt{B} = 8.8 \pm 1.6 \text{ (stat.)} {}^{+4.1}_{-3.0} \text{ (sys.)} \quad (2.8 \pm 0.5 \text{ (stat.)} {}^{+1.3}_{-1.0} \text{ (sys.)}) \quad (7.1)$$

1707 for an integrated luminosity of $30 (3) \text{ ab}^{-1}$. For $\mathcal{L} = 30 \text{ ab}^{-1}$, the significance is above the 5σ threshold.
1708 This result indicates that with the entire dataset that is expected to be accumulated by the FCC-hh
1709 detector it should be possible to observe the production of Higgs pairs.

1710 For the signal model that includes a 1 TeV dark matter mediator that can decay to pairs of SM
1711 Higgs bosons the achieve significance is $2.3 \pm 0.4 \text{ (stat.)} {}^{+1.1}_{-0.8} \text{ (sys.)}$ ($0.73 \pm 0.13 \text{ (stat.)} {}^{+0.34}_{-0.25} \text{ (sys.)}$) for an
1712 integrated luminosity of $30 (3) \text{ ab}^{-1}$. The significance is well bellow the 5σ threshold for both luminosities.
1713 Therefore, we do not expect to be able to detect or exclude this signal at the FCC-hh. In this model, the
1714 coupling of the DM mediator to the Higgs pairs is small which means that the contribution from the box

Table 7.1: Cumulative efficiency, in percentage, of each event selection criterion for the signal samples (SM, DM mediator and 2HDM). The absolute value of expected events after some key selection cuts is shown in curved brackets. The number of expected events is normalized to $\mathcal{L} = 30 \text{ ab}^{-1}$. The double horizontal line marks the pre-selection cuts. These results were obtained using the FCC-hh baseline detector design, as implemented in Delphes by the FCC-hh study group.

Selection [FCC-hh]	SM	DM mediator	2HDM type II
Gen level	100 $(2704 \pm 12) \times 10^3$	100 $(65400 \pm 29) \times 10^2$	100 $(13977 \pm 7) \times 10^3$
$N(\text{b-tags}) \geq 4$	92.488	92.593	93.430
$p_T(j_1, j_2) \geq 200 \text{ GeV}$	16.602 $(4490 \pm 5) \times 10^3$	17.033 $(11140 \pm 12) \times 10^2$	33.975 $4734 \pm 4 \times 10^3$
<hr/>			
$p_T(j_1) \geq 300 \text{ GeV}$	13.521	14.007	20.869
$p_T(j_1 + j_2) \geq 100 \text{ GeV}$	10.933	11.301	22.863
$\tau_{21}(j_1, j_2) < 0.4$	1.309	1.410	3.952
$ \Delta\eta(hh) < 1.5$	1.071	1.154	3.479
$FW2(j_1) > 0.2$	0.989	1.064	3.276
$(100 < M_{SD}(j_1, j_2) < 135) \text{ GeV}$	0.446 $(1207 \pm 8) \times 10^2$	0.487 $(3188 \pm 20) \times 10$	1.666 $(2328 \pm 8) \times 10^2$

¹⁷¹⁵ diagram dominates over the resonant production (s-channel diagram), just like in the SM. In addition,
¹⁷¹⁶ the cross section is smaller than for the SM process which leads to a smaller significance even though
¹⁷¹⁷ the efficiency is higher.

For the type II 2HDM the achieved significance is

$$S/\sqrt{B} = 16.9 \pm 3.0 \text{ (stat.)} {}^{+8.0}_{-5.9} \text{ (sys.)} \quad (5.4 \pm 0.9 \text{ (stat.)} {}^{+2.5}_{-1.9} \text{ (sys.)}) \quad (7.2)$$

¹⁷¹⁸ for an integrated luminosity of $30 (3) \text{ ab}^{-1}$. These results indicate that the contribution of this model to
¹⁷¹⁹ the production of Higgs pairs can be observed (or excluded) at the FCC-hh. When compared to the
¹⁷²⁰ SM and DM mediator signal samples, this sample has a higher efficiency which translates to a higher
¹⁷²¹ significance, therefore making it a very exciting and achievable benchmark.

¹⁷²² 7.1.1 Comparing with the ATLAS detector

¹⁷²³ The event selection of the search for $hh \rightarrow b\bar{b}b\bar{b}$ with the ATLAS detector at a CM energy of $\sqrt{s} = 100$
¹⁷²⁴ TeV is summarized in tables 7.3 and 7.4 for the signal and background samples, respectively.

¹⁷²⁵ It is interesting to compare the results obtained with the FCC-hh default detector simulation with the
¹⁷²⁶ ones obtained using the simulation of the ATLAS detector. These are summarized in table 7.5 in terms
¹⁷²⁷ of the achieved significance for an integrated luminosity of 30 ab^{-1} , for the different signal models.

¹⁷²⁸ For all the signal models, the significance increases approximately 50% going from the ATLAS de-
¹⁷²⁹ tector to the FCC-hh. This percentage is computed as $\left(\left((S/\sqrt{B})_{\text{FCC}} - (S/\sqrt{B})_{\text{ATLAS}} \right) / (S/\sqrt{B})_{\text{ATLAS}} \right) \times$

Table 7.2: Cumulative efficiency, in percentage, of each event selection criterion for the background samples ($4b + j$, $jj + 0/1/2 j$ and $t\bar{t} + 0/1/2j$). The absolute value of expected events after some key selection cuts is shown in curved brackets. The number of expected events is normalized to $\mathcal{L} = 30 \text{ ab}^{-1}$. The double horizontal line marks the pre-selection cuts. These results were obtained using the FCC-hh baseline detector design, as implemented in Delphes by the FCC-hh study group.

Selection [FCC-hh]	$4b + j$	$jj + 0/1/2j$	$t\bar{t}$
Gen level	100 $(49035 \pm 12) \times 10^6$	100 $(54698 \pm 13) \times 10^{10}$	100 $(22503 \pm 11) \times 10^8$
$N(\text{b-tags}) \geq 4$	75.819	3.963	53.495
$p_T(j_1, j_2) \geq 200 \text{ GeV}$	17.811 $(8734 \pm 5) \times 10^6$	0.742 $(4058 \pm 11) \times 10^9$	1.056 $(2377 \pm 11) \times 10^7$
<hr/>			
$p_T(j_1) \geq 300 \text{ GeV}$	12.744	0.422	0.718
$p_T(j_1 + j_2) \geq 100 \text{ GeV}$	10.901	0.245	0.617
$\tau_{21}(j_1, j_2) < 0.4$	0.256	0.002	0.037
$ \Delta\eta(hh) < 1.5$	0.130	0.001	0.024
$FW2(j_1) > 0.2$	0.105	0.001	0.014
<hr/>			
$(100 < M_{SD}(j_1, j_2) < 135) \text{ GeV}$	0.007 $(341 \pm 10) \times 10^4$	0.00003 $(17 \pm 11) \times 10^7$	0.0007 $(149 \pm 28) \times 10^5$

1730 100. For the SM signal, nonetheless, using the ATLAS default detector configuration the achieved signif-
1731 icance is already above 5σ , for $\mathcal{L} = 30 \text{ ab}^{-1}$: $S/\sqrt{B} = 5.7 \pm 1.3 \text{ (stat.) } {}^{+3.1}_{-2.4} \text{ (sys.)}$. This indicates that the
1732 CM energy and the high luminosity are the key factors driving the discovery potential of the accelerator.

1733 7.2 Hadronic calorimeter granularity studies for future colliders

1734 In this section we present the results that allow us to compare the different detector configurations. In
1735 section 7.2.1, we compare the resolution of the jet mass and of the τ_{21} variable for the different detector
1736 configurations. In section 7.2.2, we show the results obtained with the baseline and optimized analyses
1737 and compare them in terms of the achieved significances. In the optimized analyses, the statistical
1738 fluctuations are higher because the $jj + 0/1/2 j$ background with $500 < H_T < 1000$, which has the
1739 largest statistical weight, is not rejected as efficiently. Therefore, the shapes of the plots are easier to
1740 discern for the baseline analyses.

1741 The cutflow tables for the baseline and optimized analysis for all detector configurations, for all signal
1742 models and using particle flow and calorimeter can be found in appendix E. In addition, the significances
1743 achieved for all possible combinations are summarized in tables E.1 and E.2.

Table 7.3: Cumulative efficiency, in percentage, of each event selection criterion for the signal samples (SM, DM mediator and 2HDM). The absolute value of expected events after some key selection cuts is shown in curved brackets. The number of expected events is normalized to $\mathcal{L} = 30 \text{ ab}^{-1}$. The double horizontal line marks the pre-selection cuts. These results were obtained using the ATLAS detector design, as implemented in Delphes.

Selection [ATLAS]	SM	DM mediator	2HDM type II
Gen level	100 $(27043 \pm 12) \times 10^3$	100 $(65400 \pm 29) \times 10^2$	100 $(13978 \pm 6) \times 10^3$
$N(\text{b-tags}) \geq 4$	88.690	88.787	89.643
$p_T(j_1, j_2) \geq 200 \text{ GeV}$	15.533 $(4201 \pm 5) \times 10^3$	15.941 32.181 $(10426 \pm 12) \times 10^2$	$(4498 \pm 4) \times 10^3$
<hr/>			
$p_T(j_1) \geq 300 \text{ GeV}$	12.599	13.061	29.141
$p_T(j_1 + j_2) \geq 100 \text{ GeV}$	10.185	10.526	21.523
$\tau_{21}(j_1, j_2) < 0.4$	1.139	1.220	3.411
$ \Delta\eta(hh) < 1.5$	0.891	0.960	2.930
$FW2(j_1) > 0.2$	0.796	858	2.684
$(100 < M_{SD}(j_1, j_2) < 135) \text{ GeV}$	0.333 $(901 \pm 7) \times 10^2$	0.360 $(2358 \pm 18) \times 10$	1.266 $(1770 \pm 7) \times 10^2$

Table 7.4: Cumulative efficiency, in percentage, of each event selection criterion for the background samples ($4b + j$, $jj + 0/1/2j$ and $t\bar{t} + 0/1/2j$). The absolute value of expected events after some key selection cuts is shown in curved brackets. The number of expected events is normalized to $\mathcal{L} = 30 \text{ ab}^{-1}$. The double horizontal line marks the pre-selection cuts. These results were obtained using the ATLAS detector design, as implemented in Delphes.

Selection [ATLAS]	$4b + j$	$jj + 0/1/2j$	$t\bar{t}$
Gen level	100 $(49035 \pm 15) \times 10^6$	100 $(54698 \pm 15) \times 10^{10}$	100 $(22503 \pm 9) \times 10^8$
$N(\text{b-tags}) \geq 4$	71.617	3.747	51.782
$p_T(j_1, j_2) \geq 200 \text{ GeV}$	16.299 $(7993 \pm 6) \times 10^6$	0.685 $(379 \pm 11) \times 10^9$	0.985 $(2215 \pm 9) \times 10^7$
<hr/>			
$p_T(j_1) \geq 300 \text{ GeV}$	11.627	0.390	0.669
$p_T(j_1 + j_2) \geq 100 \text{ GeV}$	9.932	0.227	0.574
$\tau_{21}(j_1, j_2) < 0.4$	0.234	0.003	0.031
$ \Delta\eta(hh) < 1.5$	0.113	0.001	0.019
$FW2(j_1) > 0.2$	0.082	0.001	0.010
$(100 < M_{SD}(j_1, j_2) < 135) \text{ GeV}$	0.005 $(253 \pm 11) \times 10^4$	0.00004 $(23 \pm 15) \times 10^7$	0.0007 $(160 \pm 24) \times 10^5$

Table 7.5: Significances achieved with the ATLAS and FCC-hh detector configurations for $\mathcal{L} = 30 \text{ ab}^{-1}$ for the three benchmark signal models: SM, 1 TeV DM mediator and 2HDM with $m_H = 900 \text{ GeV}$.

Signal sample	ATLAS	FCC-hh
SM	$5.7 \pm 1.3 \text{ (stat.)} {}^{+2.7}_{-2.0} \text{ (sys.)}$	$8.8 \pm 1.6 \text{ (stat.)} {}^{+4.1}_{-3.1} \text{ (sys.)}$
1 TeV DM mediator	$1.50 \pm 0.23 \text{ (stat.)} {}^{+0.7}_{-0.5} \text{ (sys.)}$	$2.3 \pm 0.4 \text{ (stat.)} {}^{+1.1}_{-0.8} \text{ (sys.)}$
2HDM type II	$11.3 \pm 1.7 \text{ (stat.)} {}^{+5.4}_{-3.9} \text{ (sys.)}$	$16.9 \pm 3.0 \text{ (stat.)} {}^{+8.0}_{-5.9} \text{ (sys.)}$

1744 7.2.1 Resolution of jet mass and N-subjetiness

1745 The softdrop mass of the leading Higgs candidate for the SM signal sample is shown in figure 7.1(a) for
 1746 the different detector configurations. The same plot is shown in figure 7.1(b) for calorimeter jets. It can
 1747 be seen that the mass resolution increases as we increase the granularity, i.e, the mass peaks becomes
 1748 narrower. This effect is more pronounced when using pure calorimeter jets. In order to quantify this effect
 1749 we use the full width at half maximum (FWHM). For particle flow (calorimeter) jets, the FWHM varies
 1750 from 126 (130) for the ATLAS detector configuration to 124 (122) for the FCC granularity with $\eta, \phi \times 2$
 1751 which corresponds to a 1% (6%) effect.

1752 The invariant mass of the Higgs pair is shown in figure 7.2 for the SM signal when using particle flow
 1753 jets. The same distribution is shown for the DM mediator and 2HDM signals in figures 7.3(a) and 7.3(b),
 1754 respectively. For the SM, the mass spectrum of the Higgs pair does not show any resonance peak. On
 1755 the one hand, the production is dominated by the box diagram. On the other hand, even if we only had
 1756 the contribution from the triangle diagram, the Higgs that decays to a pair of Higgs bosons has to be off
 1757 shell, therefore we expect a broad spectrum. For the DM mediator model, there is an enhancement with
 1758 respect to the SM for $M(hh) \sim 1 \text{ TeV}$. This is due to the contribution of the 1 TeV DM mediator decaying
 1759 to pairs of SM Higgs bosons. Nonetheless, the spectrum is still quite broad because the box diagram
 1760 stills gives a very large contribution. For the 2HDM, there is a clear peak at $M(hh) \sim 900 \text{ GeV}$ because
 1761 resonant production dominates. The mass resolution of the resonances does not seem to increase as
 1762 the granularity increases. This picture holds even when using HCAL jets.

1763 The τ_{21} variable for the leading Higgs candidate for the SM signal (filled lines) and for the $4b + j$
 1764 background (dashed lines) is shown in figure 7.4(a) for the different detector configurations for particle
 1765 flow jets. The same plot is show in figure 7.4(b) for calorimeter jets. The separation between signal
 1766 and background increases as the granularity increases. This was expected because an increase in the
 1767 granularity of the hadronic calorimeter should help resolve better the substructure of boosted jets. For
 1768 particle flow jets, the distance between the maximum points of the two distributions varies from 0.4 for
 1769 the ATLAS detector, ATLAS HCAL and ATLAS HCAL with $\eta \times 4$ to 0.44 for the FCC HCAL with $\phi/2$ and to
 1770 0.46 for the remaining configurations. For calorimeter jets the distance between the maximum is always
 1771 smaller than when using particle flow jets, considering the same detector configuration. Therefore, the
 1772 separation is always better when using particle flow jets. However, when using calorimeter jets, there is
 1773 a larger difference in the shape of the distributions for the multiple detector configurations, particularly
 1774 when going from the ATLAS granularity with $\eta \times 4$ to the FCC granularity with $\phi/2$.

1775 The separation is the largest between the signal and the $jj + 0/1/2 j$ background, as expected.
1776 For this background, the distance between the maximums of the distributions varies from 0.48 (0.24) to
1777 0.56 (0.48), for particle flow (calorimeter) jets. These distributions can be found in figures F.2(a) and
1778 F.2(b) in appendix F.

1779 7.2.2 Signal efficiency and significance

1780 Figure 7.5(a) shows the signal efficiency for the three signal models: SM (filled squares), 1 TeV DM
1781 mediator (empty squares) and type II 2HDM with $m_H = 900$ GeV (crosses), for eflow jets, for the baseline
1782 analysis. The same plot is shown in figure 7.5(b) for calorimeter jets. For eflow jets the efficiency
1783 increases as we increase the granularity, for all signal models. It varies approximately 30% between the
1784 lowest value (ATLAS default) and the highest value (FCC granularity with $\eta, \phi \times 2$). For HCAL jets, this
1785 tendency also exists with the exception of the first point which corresponds to the ATLAS default detector
1786 configuration. [WHY? OPTIMIZATION OF ATLAS?]. In addition, the efficiency changes more when using
1787 pure calorimeter jets. It varies by approximately 98% between the ATLAS detector configuration and the
1788 configuration with the FCC granularity and $\eta, \phi \times 2$. The efficiency is higher for both BSM models than
1789 for the SM. This is because these models were chosen to have very heavy particles decaying to a pair
1790 of highly boosted Higgs pairs. For the optimized analysis, these plots follow a very similar tendency. The
1791 absolute values of the efficiencies are slightly higher, as expected. These plots can be found in figures
1792 F.3(a) and F.3(b) in appendix F, for particle flow and calorimeter jets, respectively.

1793 The significances achieved with the baseline analysis as a function of the detector configuration
1794 for the SM signal, the DM mediator model and the type II 2HDM are shown in figures 7.6(a), 7.7(a)
1795 and 7.8(a), respectively. The same plots are shown for the optimized analysis in figures 7.6(b), 7.7(b)
1796 and 7.8(b). The square markers refer to analysis performed using particle flow jets. The statistical
1797 uncertainty associated with each value of the significance is computed using standard error propaga-
1798 tion and is shown as error bars. The grey blocks represent the total uncertainty. For the baseline
1799 analysis, regardless of the signal model considered, the significance chances by approximately 15%
1800 when going from the ATLAS detector configuration to the configuration with the FCC granularity in-
1801 creased by a factor of two in η and ϕ . For the optimized analysis the change is of approximately
1802 54%. These percentages, as well as the ones given in the following paragraph, are calculated as
1803 $((S/\sqrt{B})_{\text{FCC}} - (S/\sqrt{B})_{\text{ATLAS}})/(S/\sqrt{B})_{\text{ATLAS}} \times 100$.

1804 Motivated by the small change in significance over the range of configurations that were tested,
1805 we implemented exactly the same analysis but using HCAL jets instead of eflow jets. The results are
1806 shown in the same plots using triangular markers and with green error blocks. On the one hand, the
1807 achieved significance is always smaller when using HCAL jets because we are not making use of the
1808 tracking information. On the other hand, when using HCAL jets, the significance changes more over
1809 the configuration range. For the SM signal, it varies by approximately 80% when going from the ATLAS
1810 detector configuration to the configuration with the FCC granularity increased by a factor of two in η and
1811 ϕ . For the DM mediator model, this value is 77% and for the 2HDM it is 60%. These percentages refer

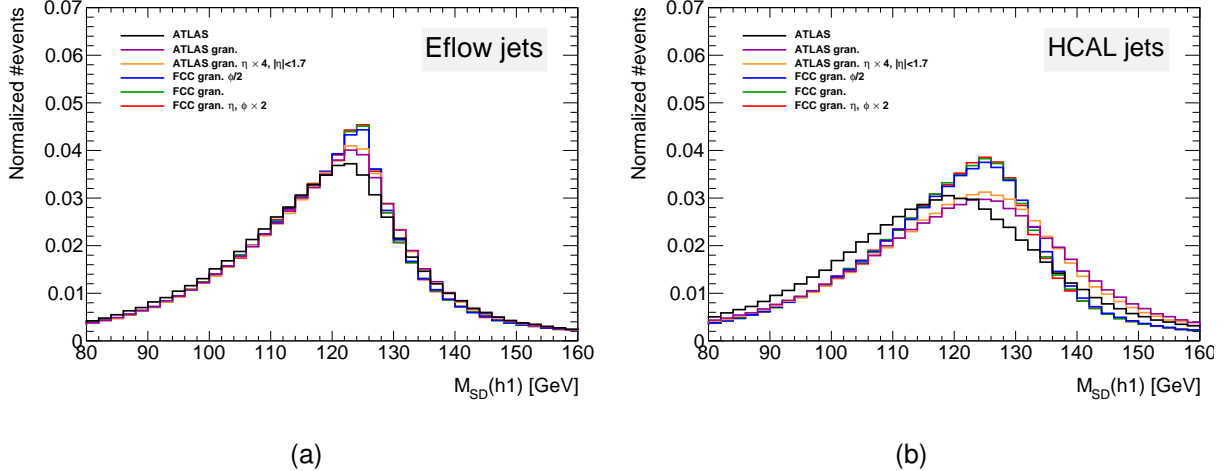


Figure 7.1: Leading Higgs candidate softdrop mass after the pre-selection cuts for particle flow (a) and calorimeter (b) jets. The colors indicate the different detector configurations. The x axis range is from 80 GeV to 160 GeV in order to make the differences between the histograms more clear.

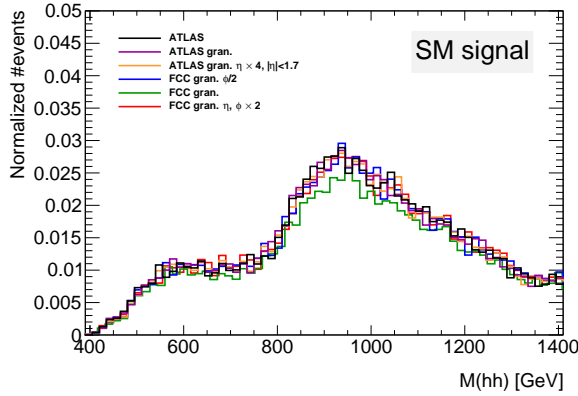


Figure 7.2: Invariant mass of the Higgs pair for the SM signal. The plots include the events that pass all the analysis cuts. The colors indicate the different detector configurations.

1812 to the baseline analysis. For the optimized analysis the change is of 71%, 69% and 55%, for the SM, DM
 1813 mediator and 2HDM signal models, respectively.

1814 All in all, given the large uncertainties, it is hard to conclude on the tendency followed by the plots
 1815 of the significance as a function of the detector configuration. Nonetheless, the significance does seem
 1816 to increase as the granularity increases, which is what was expected. As previously discussed, this
 1817 effect is more accentuated when using pure calorimeter jets because we are only making use of the
 1818 information provided by the hadronic calorimeter and therefore the analysis is more sensitive to its
 1819 transversal segmentation (granularity), which is exactly the parameter that is varied in this study.

1820 The small change in the significance when using eflow jets and the fact that the change increases
 1821 when using HCAL jets indicate that in the FCC-hh baseline detector design the resolution of the tracking
 1822 system is so good, in particular, so much better than the HCAL spatial resolution (given by its transversal
 1823 segmentation), that it becomes the limiting factor.

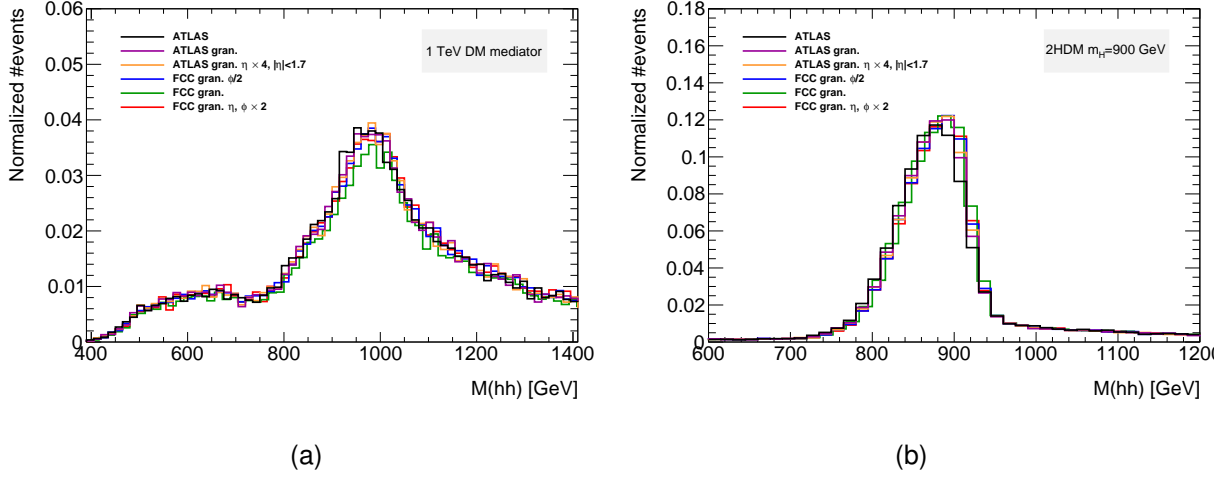


Figure 7.3: Invariant mass of the Higgs pair for the 1 TeV DM mediator (a) and for the 2HDM with $m_H = 900$ GeV (b). The plots include the events that pass all the analysis cuts. The colors indicate the different detector configurations.

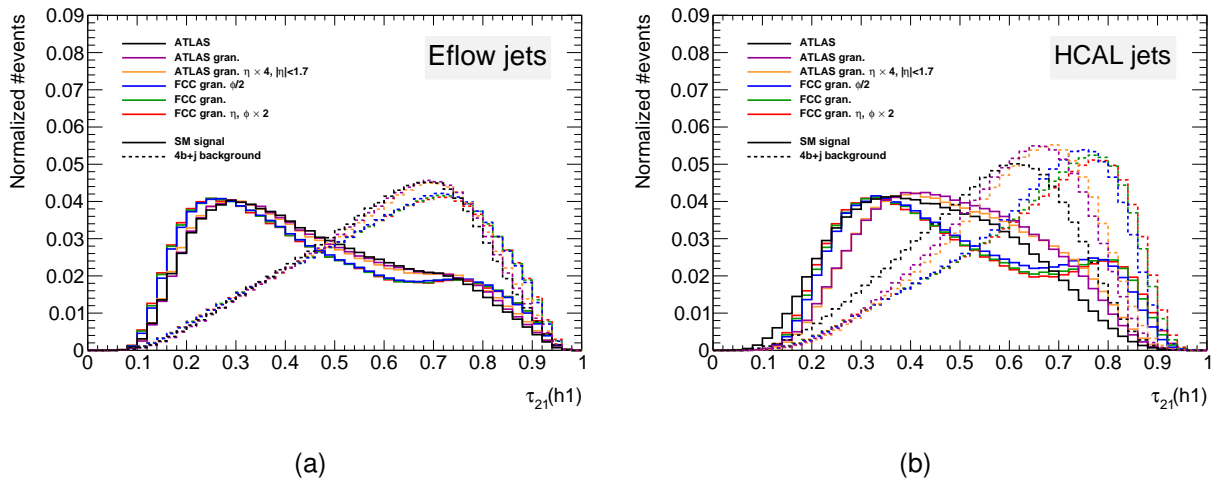


Figure 7.4: Leading Higgs candidate τ_{21} distribution for eflow jets (a) and for HCAL jets (b). The colors indicate the different detector configurations. The distributions are shown for the signal (filled lines) and for the $4b + j$ background (dashed lines).

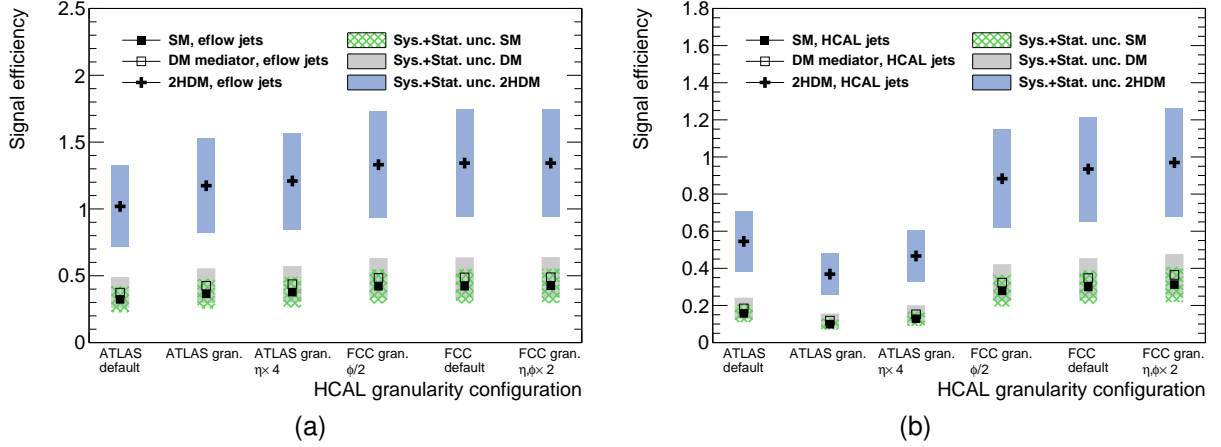


Figure 7.5: Signal efficiency as a function of the detector configuration for particle flow jets (a) and for calorimeter jets (b). Three signal models are shown: SM (filled squares), 1 TeV DM mediator (empty squares) and type II 2HDM with $m_H = 900$ GeV (crosses). The statistical error bars are drawn but are smaller than the markers.

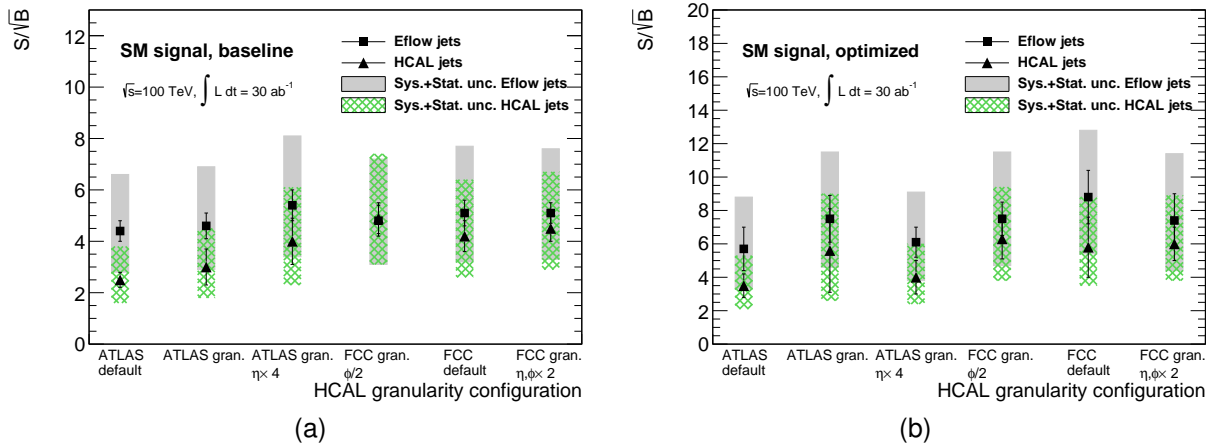


Figure 7.6: Significance as a function of the detector configuration for the SM signal, for the baseline (a) and optimized (b) analyses. The significances are shown for eflow jets (squares) and pure HCAL jets (triangles).

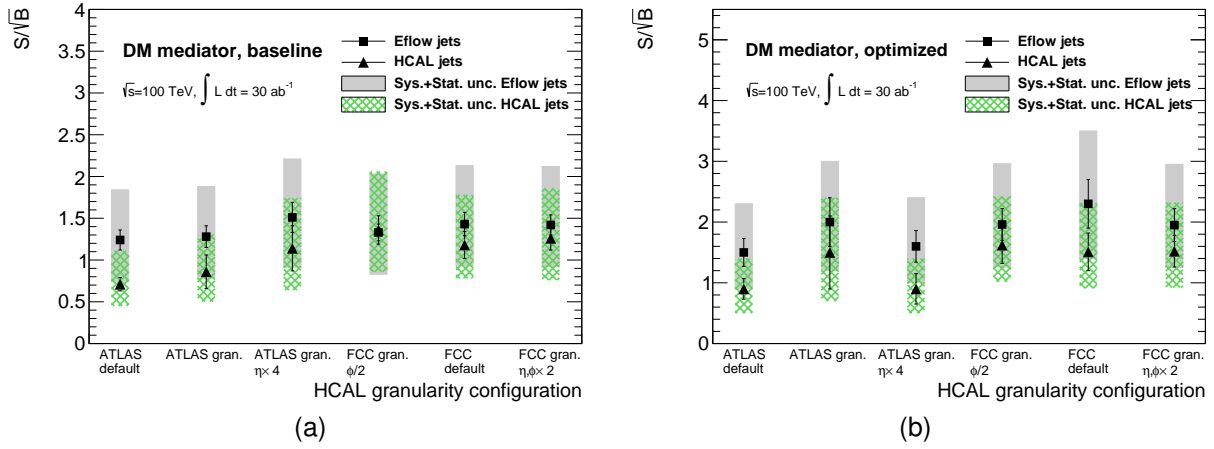


Figure 7.7: Significance as a function of the detector configuration for the DM mediator signal, for the baseline (a) and optimized (b) analyses. The significances are shown for eflow jets (squares) and pure HCAL jets (triangles).

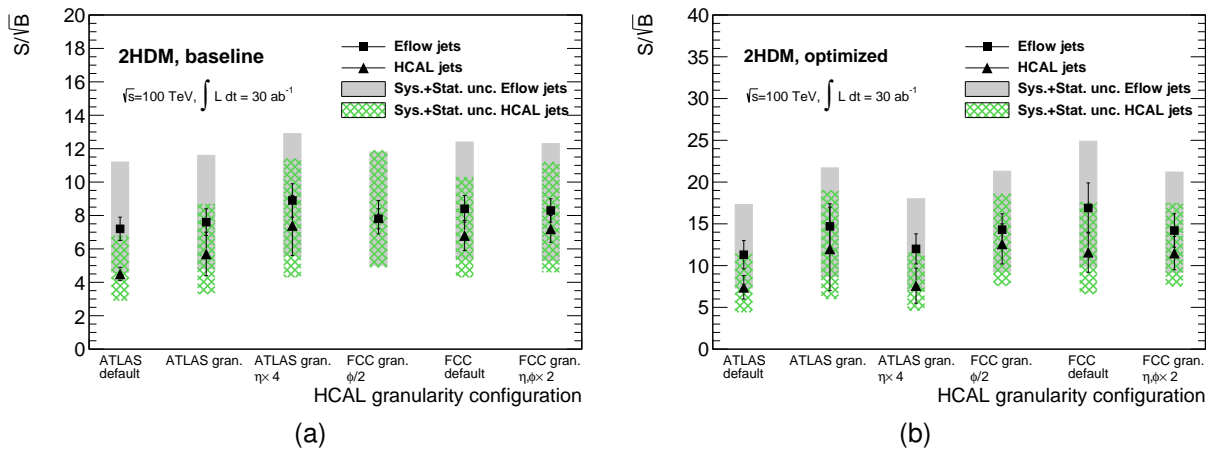


Figure 7.8: Significance as a function of the detector configuration for the 2HDM signal, for the baseline (a) and optimized (b) analyses. The significances are shown for eflow jets (squares) and pure HCAL jets (triangles).

1824

Chapter 8

1825

Conclusions

1826 This thesis presented a feasibility study targeting the search for Higgs pair production in the $pp \rightarrow hh \rightarrow$
1827 $b\bar{b}b\bar{b}$ channel at a center of mass energy of $\sqrt{s} = 100$ TeV. The analysis targeted a boosted kinematic
1828 regime. The impact of the granularity of the hadronic calorimeter in the achieved significance was
1829 analyzed.

1830 The analysis consisted of a cut-based event selection designed to efficiently select signal events con-
1831 sistent with a boosted topology. In addition to standard kinematic variables, jet substructure variables,
1832 namely a ratio of N-subjetiness variables and a Fox-Wolfram momentum, are used to further suppress
1833 the background. The analysis required the existence of at least two b-tagged large- R jets consistent
1834 with having two subjets and with $p_T > 200$ GeV. Multijet production through QCD interactions and $t\bar{t}$
1835 production constitute the main backgrounds. The very large yield of the backgrounds when compared
1836 to the signal makes this a very challenging analysis.

1837 In addition to SM Higgs pair production, two BSM benchmark processes were considered: a 1
1838 TeV dark matter mediator and a heavy Higgs boson with $m_H = 900$ GeV in the framework of the
1839 CP-conserving type II 2HDM, both decaying to pairs of SM Higgs bosons. The existence of heavy
1840 resonances is expected to enhance Higgs pair production with respect to the SM.

1841 For the hadronic Future Circular Collider (FCC-hh), the significance obtained was $S/\sqrt{B} = 8.8 \pm$
1842 1.6 (stat.) $^{+4.1}_{-3.0}$ (sys.) (2.8 ± 0.5 (stat.) $^{+1.3}_{-1.0}$ (sys.)) for an integrated luminosity of $\mathcal{L} = 30$ (3) ab^{-1} . For
1843 $\mathcal{L} = 30 \text{ ab}^{-1}$, the value is above the observation threshold (5σ) which indicates that the full dataset that is
1844 expected to be collected during the operation of the FCC-hh should be enough to claim the observation
1845 of Higgs pair production, assuming SM production. For the CP-conserving type II 2HDM with $m_H = 900$
1846 GeV, the achieved significance was $S/\sqrt{B} = 16.9 \pm 3.0$ (stat.) $^{+8.0}_{-5.9}$ (sys.) (5.4 ± 0.9 (stat.) $^{+2.5}_{-1.9}$ (sys.))
1847 for an integrated luminosity of $\mathcal{L} = 30$ (3) ab^{-1} , which makes it an accessible benchmark for the HL-
1848 LHC and future colliders. The achieved significance for the 1 TeV DM mediator is of order 2 even for
1849 an integrated luminosity of $\mathcal{L} = 30 \text{ ab}^{-1}$, which makes it a very challenging benchmark and probably
1850 unaccessible even at future high energy colliders.

1851 With the ATLAS detector simulation, the achieved significance for the SM signal is $S/\sqrt{B} = 5.7 \pm$
1852 1.3 (stat.) $^{+3.1}_{-2.4}$ (sys.) (1.8 ± 0.4 (stat.) $^{+0.9}_{-0.6}$ (sys.)) for an integrated luminosity of $\mathcal{L} = 30$ (3) ab^{-1} , for

1853 which the nominal value is also above the observation threshold. This result indicates that the factors
1854 driving the discovery potential of the accelerator are the CM energy and high luminosity as opposed to
1855 the resolution of the detector.

1856 The resolution of the jet mass and the separation provided by the τ_{21} variable are shown to increase
1857 as the granularity of the HCAL increases. This effect is more evident when using pure calorimeter jets.

1858 When using particle flow jets, the change in the significance over the range of detector configurations
1859 tested is small, for all signal models. For the baseline (optimized) analysis, it varies by approximately
1860 15% (54%), for all signal models, between the ATLAS default detector configuration and the FCC-hh
1861 detector with twice the granularity in η and ϕ . Using pure calorimeter jets, the change in significance is
1862 more accentuated. For the SM signal, it varies by approximately 80% (71%), considering the baseline
1863 (optimized) analysis. For the same detector configuration, the significance is always smaller when using
1864 calorimeter jets. The same qualitative conclusions hold for the BSM models. The effect of the granularity
1865 is of the same order of magnitude as for the SM. These results lead to the conclusion that the jet
1866 reconstruction performance is dominated by the tracking system.

1867 As future work, performing studies similar to the one presented here but using other benchmark
1868 processes as well as full detector simulation would be of the utmost importance to the optimization of
1869 the design of particle detectors for future high energy hadronic colliders. In addition, the impact of pileup
1870 should be assessed and multivariate techniques could be implemented to further optimize the event
1871 selection.

Bibliography

- [1] J. Goldstone. Field Theories with Superconductor Solutions. *Nuovo Cim.*, 19:154–164, 1961. doi: 10.1007/BF02812722.
- [2] Y. Nambu and G. Jona-Lasinio. Dynamical Model of Elementary Particles Based on an Analogy with Superconductivity. 1. *Phys. Rev.*, 122:345–358, 1961. doi: 10.1103/PhysRev.122.345. [,127(1961)].
- [3] G. Arnison et al. Experimental Observation of Lepton Pairs of Invariant Mass Around 95-GeV/c**2 at the CERN SPS Collider. *Phys. Lett.*, B126:398–410, 1983. doi: 10.1016/0370-2693(83)90188-0. [,7.55(1983)].
- [4] G. Arnison et al. Experimental Observation of Isolated Large Transverse Energy Electrons with Associated Missing Energy at $s^{**}(1/2) = 540\text{-GeV}$. *Phys. Lett.*, B122:103–116, 1983. doi: 10.1016/0370-2693(83)91177-2. [,611(1983)].
- [5] F. Wilczek. Spontaneous symmetry breaking: General. <http://web.mit.edu/8.701/www/LectureNotes/8.701spontaneousSymmetryBreaking-GeneralFA13.pdf>, 2013. Accessed 2018-01-11.
- [6] P. W. Higgs. Broken Symmetries and the Masses of Gauge Bosons. *Phys. Rev. Lett.*, 13:508–509, 1964. doi: 10.1103/PhysRevLett.13.508. [,160(1964)].
- [7] F. Englert and R. Brout. Broken Symmetry and the Mass of Gauge Vector Mesons. *Phys. Rev. Lett.*, 13:321–323, 1964. doi: 10.1103/PhysRevLett.13.321. [,157(1964)].
- [8] G. S. Guralnik, C. R. Hagen, and T. W. B. Kibble. Global Conservation Laws and Massless Particles. *Phys. Rev. Lett.*, 13:585–587, 1964. doi: 10.1103/PhysRevLett.13.585. [,162(1964)].
- [9] R. Costa Batalha Pedro, J. Maneira, and P. Conde Muio. Search for the Higgs boson at ATLAS/LHC in WH associated production and decay to b quark pairs, Apr 2017. URL <https://cds.cern.ch/record/2304102>. Presented 09 Nov 2017.
- [10] C. S. Wu, E. Ambler, R. W. Hayward, D. D. Hoppes, and R. P. Hudson. Experimental test of parity conservation in beta decay. *Phys. Rev.*, 105:1413–1415, Feb 1957. doi: 10.1103/PhysRev.105.1413. URL <https://link.aps.org/doi/10.1103/PhysRev.105.1413>.

- 1899 [11] M. Goldhaber, L. Grodzins, and A. W. Sunyar. Helicity of neutrinos. *Phys. Rev.*, 109:
 1900 1015–1017, Feb 1958. doi: 10.1103/PhysRev.109.1015. URL <https://link.aps.org/doi/10.1103/PhysRev.109.1015>.
- 1901
 1902 [12] S. M. Bilenky and J. Hosek. GLASHOW-WEINBERG-SALAM THEORY OF ELECTROWEAK
 1903 INTERACTIONS AND THE NEUTRAL CURRENTS. *Phys. Rept.*, 90:73–157, 1982. doi: 10.
 1904 1016/0370-1573(82)90016-3.
- 1905 [13] R. Frederix, S. Frixione, V. Hirschi, F. Maltoni, O. Mattelaer, P. Torrielli, E. Vryonidou, and M. Zaro.
 1906 Higgs pair production at the LHC with NLO and parton-shower effects. *Phys. Lett.*, B732:142–149,
 1907 2014. doi: 10.1016/j.physletb.2014.03.026.
- 1908 [14] M. Mangano. *Physics at the FCC-hh, a 100 TeV pp collider*. CERN Yellow Reports: Monographs.
 1909 CERN, Geneva, 2017. URL <https://cds.cern.ch/record/2270978>.
- 1910 [15] T. Plehn, M. Spira, and P. M. Zerwas. Pair production of neutral Higgs particles in gluon-
 1911 gluon collisions. *Nucl. Phys.*, B479:46–64, 1996. doi: 10.1016/0550-3213(96)00418-X, 10.1016/
 1912 S0550-3213(98)00406-4. [Erratum: Nucl. Phys.B531,655(1998)].
- 1913 [16] S. Borowka, N. Greiner, G. Heinrich, S. Jones, M. Kerner, J. Schlenk, U. Schubert, and T. Zirke.
 1914 Higgs Boson Pair Production in Gluon Fusion at Next-to-Leading Order with Full Top-Quark Mass
 1915 Dependence. *Phys. Rev. Lett.*, 117(1):012001, 2016. doi: 10.1103/PhysRevLett.117.079901, 10.
 1916 1103/PhysRevLett.117.012001. [Erratum: Phys. Rev. Lett.117,no.7,079901(2016)].
- 1917 [17] S. Borowka, N. Greiner, G. Heinrich, S. P. Jones, M. Kerner, J. Schlenk, and T. Zirke. Full top
 1918 quark mass dependence in Higgs boson pair production at NLO. *JHEP*, 10:107, 2016. doi:
 1919 10.1007/JHEP10(2016)107.
- 1920 [18] H. C. van de Hulst, E. Raimond, and H. van Woerden. Rotation and density distribution of the
 1921 Andromeda nebula derived from observations of the 21-cm line. 14:1, Nov. 1957.
- 1922 [19] Y. Fukuda et al. Evidence for oscillation of atmospheric neutrinos. *Phys. Rev. Lett.*, 81:1562–1567,
 1923 1998. doi: 10.1103/PhysRevLett.81.1562.
- 1924 [20] Q. R. Ahmad et al. Measurement of the rate of $\nu_e + d \rightarrow p + p + e^-$ interactions produced by
 1925 8B solar neutrinos at the Sudbury Neutrino Observatory. *Phys. Rev. Lett.*, 87:071301, 2001. doi:
 1926 10.1103/PhysRevLett.87.071301.
- 1927 [21] Q. R. Ahmad et al. Direct evidence for neutrino flavor transformation from neutral current
 1928 interactions in the Sudbury Neutrino Observatory. *Phys. Rev. Lett.*, 89:011301, 2002. doi:
 1929 10.1103/PhysRevLett.89.011301.
- 1930 [22] B. Gripaios. Lectures on Physics Beyond the Standard Model. 2015.
- 1931 [23] N. M. A. 2018. Popular information, 2004. URL <https://www.nobelprize.org/prizes/physics/2004/popular-information/>.
- 1932

- [24] V. Branchina, F. Contino, and P. M. Ferreira. Electroweak vacuum lifetime in two Higgs doublet models. 2018.
- [25] J. F. Gunion and H. E. Haber. The CP conserving two Higgs doublet model: The Approach to the decoupling limit. *Phys. Rev.*, D67:075019, 2003. doi: 10.1103/PhysRevD.67.075019.
- [26] H. Sun, Y.-J. Zhou, and H. Chen. Constraints on large-extra-dimensions model through 125-GeV Higgs pair production at the LHC. *Eur. Phys. J.*, C72:2011, 2012. doi: 10.1140/epjc/s10052-012-2011-4.
- [27] P. Huang, A. Joglekar, M. Li, and C. E. M. Wagner. Corrections to di-Higgs boson production with light stops and modified Higgs couplings. *Phys. Rev.*, D97(7):075001, 2018. doi: 10.1103/PhysRevD.97.075001.
- [28] G. Aad et al. Observation of a new particle in the search for the Standard Model Higgs boson with the ATLAS detector at the LHC. *Phys. Lett.*, B716:1–29, 2012. doi: 10.1016/j.physletb.2012.08.020.
- [29] S. Chatrchyan et al. Observation of a new boson at a mass of 125 GeV with the CMS experiment at the LHC. *Phys. Lett.*, B716:30–61, 2012. doi: 10.1016/j.physletb.2012.08.021.
- [30] Observation of $H \rightarrow b\bar{b}$ decays and VH production with the ATLAS detector. Technical Report ATLAS-CONF-2018-036, CERN, Geneva, Jul 2018. URL <http://cds.cern.ch/record/2630338>.
- [31] Observation of Higgs boson decay to bottom quarks. Technical Report arXiv:1808.08242. CMS-HIG-18-016-003, CERN, Geneva, Aug 2018. URL <https://cds.cern.ch/record/2636067>. * Temporary entry *.
- [32] A. M. Sirunyan et al. Observation of the Higgs boson decay to a pair of τ leptons with the CMS detector. *Phys. Lett.*, B779:283–316, 2018. doi: 10.1016/j.physletb.2018.02.004.
- [33] A. M. Sirunyan et al. Observation of $t\bar{t}H$ production. *Phys. Rev. Lett.*, 120:231801, 2018. doi: 10.1103/PhysRevLett.120.231801.
- [34] M. Aaboud et al. Observation of Higgs boson production in association with a top quark pair at the LHC with the ATLAS detector. 2018.
- [35] Measurement of the Higgs boson mass in the $H \rightarrow ZZ^* \rightarrow 4\ell$ and $H \rightarrow \gamma\gamma$ channels with $\sqrt{s}=13\text{TeV}$ pp collisions using the ATLAS detector. Technical Report ATLAS-CONF-2017-046, CERN, Geneva, Jul 2017. URL <http://cds.cern.ch/record/2273853>.
- [36] G. Aad et al. Combined Measurement of the Higgs Boson Mass in pp Collisions at $\sqrt{s} = 7$ and 8 TeV with the ATLAS and CMS Experiments. *Phys. Rev. Lett.*, 114:191803, 2015. doi: 10.1103/PhysRevLett.114.191803.
- [37] M. Aaboud et al. Measurement of the W -boson mass in pp collisions at $\sqrt{s} = 7$ TeV with the ATLAS detector. *Eur. Phys. J.*, C78(2):110, 2018. doi: 10.1140/epjc/s10052-017-5475-4.

- 1967 [38] R. Nisius. Measurements of the top quark mass with the ATLAS detector. *PoS*, EPS-HEP2017:
1968 453, 2017. doi: 10.22323/1.314.0453.
- 1969 [39] Measurement of the top quark mass with muon+jets final states in pp collisions at $\sqrt{s} = 13$ TeV.
1970 Technical Report CMS-PAS-TOP-16-022, CERN, Geneva, 2017. URL <http://cds.cern.ch/record/2255834>.
- 1972 [40] CERN. The high-luminosity lhc. <http://cds.cern.ch/record/2114693>, 2015. Accessed
1973 2018/01/11.
- 1974 [41] T. Koffas. ATLAS Higgs physics prospects at the high luminosity LHC. *PoS*, ICHEP2016:426,
1975 2017.
- 1976 [42] A. M. Henriques Correia. The ATLAS Tile Calorimeter. Technical Report ATL-TILECAL-PROC-
1977 2015-002, CERN, Geneva, Mar 2015. URL <https://cds.cern.ch/record/2004868>.
- 1978 [43] ATLAS liquid argon calorimeter: Technical design report. 1996.
- 1979 [44] M. Cacciari, G. P. Salam, and G. Soyez. The Catchment Area of Jets. *JHEP*, 04:005, 2008. doi:
1980 10.1088/1126-6708/2008/04/005.
- 1981 [45] Optimisation of the ATLAS b -tagging performance for the 2016 LHC Run. Technical Report ATL-
1982 PHYS-PUB-2016-012, CERN, Geneva, Jun 2016. URL <https://cds.cern.ch/record/2160731>.
- 1983 [46] Commissioning of the ATLAS high-performance b -tagging algorithms in the 7 TeV collision data.
1984 Technical Report ATLAS-CONF-2011-102, CERN, Geneva, Jul 2011. URL <https://cds.cern.ch/record/1369219>.
- 1986 [47] G. Aad et al. Expected Performance of the ATLAS Experiment - Detector, Trigger and Physics.
1987 2009.
- 1988 [48] A. Ruiz-Martinez and A. Collaboration. The Run-2 ATLAS Trigger System. Technical Report ATL-
1989 DAQ-PROC-2016-003, CERN, Geneva, Feb 2016. URL <https://cds.cern.ch/record/2133909>.
- 1990 [49] S. D. Ellis and D. E. Soper. Successive combination jet algorithm for hadron collisions. *Phys. Rev.*,
1991 D48:3160–3166, 1993. doi: 10.1103/PhysRevD.48.3160.
- 1992 [50] M. Wobisch and T. Wengler. Hadronization corrections to jet cross-sections in deep inelastic
1993 scattering. In *Monte Carlo generators for HERA physics. Proceedings, Workshop, Hamburg,*
1994 *Germany, 1998-1999*, pages 270–279, 1998. URL https://inspirehep.net/record/484872/files/arXiv:hep-ph_9907280.pdf.
- 1996 [51] M. Cacciari, G. P. Salam, and G. Soyez. The Anti- $k(t)$ jet clustering algorithm. *JHEP*, 04:063,
1997 2008. doi: 10.1088/1126-6708/2008/04/063.
- 1998 [52] A. Altheimer et al. Boosted objects and jet substructure at the LHC. Report of BOOST2012, held
1999 at IFIC Valencia, 23rd-27th of July 2012. *Eur. Phys. J.*, C74(3):2792, 2014. doi: 10.1140/epjc/
2000 s10052-014-2792-8.

- 2001 [53] G. A. et al. Performance of jet substructure techniques for large-r jets in proton-proton collisions
 2002 at $\sqrt{s} = 7$ tev using the atlas detector. *Journal of High Energy Physics*, 2013(9), Sep 2013. doi:
 2003 10.1007/JHEP09(2013)076. URL [https://doi.org/10.1007/JHEP09\(2013\)076](https://doi.org/10.1007/JHEP09(2013)076).
- 2004 [54] J. Thaler and K. Van Tilburg. Identifying Boosted Objects with N-subjettiness. *JHEP*, 03:015,
 2005 2011. doi: 10.1007/JHEP03(2011)015.
- 2006 [55] C. Chen. New approach to identifying boosted hadronically-decaying particle using jet substruc-
 2007 ture in its center-of-mass frame. *Phys. Rev.*, D85:034007, 2012. doi: 10.1103/PhysRevD.85.
 2008 034007.
- 2009 [56] J. M. Butterworth, A. R. Davison, M. Rubin, and G. P. Salam. Jet substructure as a new Higgs
 2010 search channel at the LHC. *Phys. Rev. Lett.*, 100:242001, 2008. doi: 10.1103/PhysRevLett.100.
 2011 242001.
- 2012 [57] I. Hinchliffe, A. Kotwal, M. L. Mangano, C. Quigg, and L.-T. Wang. Luminosity goals for a 100-TeV
 2013 pp collider. *Int. J. Mod. Phys.*, A30(23):1544002, 2015. doi: 10.1142/S0217751X15440029.
- 2014 [58] N. Arkani-Hamed, T. Han, M. Mangano, and L.-T. Wang. Physics opportunities of a 100 TeV
 2015 protonproton collider. *Phys. Rept.*, 652:1–49, 2016. doi: 10.1016/j.physrep.2016.07.004.
- 2016 [59] S. Banerjee, C. Englert, M. L. Mangano, M. Selvaggi, and M. Spannowsky. $hh + \text{jet}$ production at
 2017 100 TeV. *Eur. Phys. J.*, C78(4):322, 2018. doi: 10.1140/epjc/s10052-018-5788-y.
- 2018 [60] C. Helsens. Fcc/he-lhc physics/performance studies towards the cdr. URL: https://indico.cern.ch/event/675588/contributions/2765045/attachments/1572548/2484309/Clement_FCC.pdf, 2017.
- 2021 [61] T. an FCC-hh Detector Magnet System. E. bielert, 2018. URL <https://ep-news.web.cern.ch/content/towards-fcc-hh-detector-magnet-system>.
- 2023 [62] J. Faltova. Electromagnetic calorimeter using lar technology for fcc-hh. URL: https://indico.cern.ch/event/556692/contributions/2465166/attachments/1468150/2272205/ecal_fccBerlin.pdf, 2017.
- 2026 [63] A. Zaborowska. Electromagnetic calorimetry based on liquid argon for the fcc-hh experi-
 2027 ments. URL: https://indico.cern.ch/event/656491/contributions/2923535/attachments/1631506/2601159/FCChh_LArCalo_Zaborowska.pdf, 2018.
- 2029 [64] C. Neubser. Performance studies and requirements on the calorimeters for a fcc-hh ex-
 2030 periment. URL: <https://indico.ihep.ac.cn/event/6387/session/14/contribution/117/material/slides/0.pdf>, 2017.
- 2032 [65] M. Aaboud et al. Search for pair production of Higgs bosons in the $b\bar{b}b\bar{b}$ final state using proton–
 2033 proton collisions at $\sqrt{s} = 13$ TeV with the ATLAS detector. *Phys. Rev.*, D94(5):052002, 2016. doi:
 2034 10.1103/PhysRevD.94.052002.

- 2035 [66] A. M. Sirunyan et al. Search for a massive resonance decaying to a pair of Higgs bosons in the
 2036 four b quark final state in proton-proton collisions at $\sqrt{s} = 13$ TeV. 2017.
- 2037 [67] G. Aad et al. Searches for Higgs boson pair production in the $hh \rightarrow bb\tau\tau, \gamma\gamma WW^*, \gamma\gamma bb, bbbb$
 2038 channels with the ATLAS detector. *Phys. Rev.*, D92:092004, 2015. doi: 10.1103/PhysRevD.92.
 2039 092004.
- 2040 [68] A. M. Sirunyan et al. Search for Higgs boson pair production in events with two bottom quarks and
 2041 two tau leptons in proton-proton collisions at $\sqrt{s} = 13$ TeV. 2017.
- 2042 [69] M. Aaboud et al. A search for resonant and non-resonant Higgs boson pair production in the
 2043 $b\bar{b}\tau^+\tau^-$ decay channel in pp collisions at $\sqrt{s} = 13$ TeV with the ATLAS detector . Technical Report
 2044 arXiv:1808.00336, CERN, Geneva, Aug 2018. URL <https://cds.cern.ch/record/2632994>. *
 2045 Temporary entry *.
- 2046 [70] V. Khachatryan et al. Search for two Higgs bosons in final states containing two photons and
 2047 two bottom quarks in proton-proton collisions at 8 TeV. *Phys. Rev.*, D94(5):052012, 2016. doi:
 2048 10.1103/PhysRevD.94.052012.
- 2049 [71] G. Aad et al. Search For Higgs Boson Pair Production in the $\gamma\gamma b\bar{b}$ Final State using pp Collision
 2050 Data at $\sqrt{s} = 8$ TeV from the ATLAS Detector. *Phys. Rev. Lett.*, 114(8):081802, 2015. doi:
 2051 10.1103/PhysRevLett.114.081802.
- 2052 [72] A. M. Sirunyan et al. Search for resonant and nonresonant Higgs boson pair production in the
 2053 $b\bar{b}lnlnu$ final state in proton-proton collisions at $\sqrt{s} = 13$ TeV. 2017.
- 2054 [73] M. Aaboud et al. Combination of searches for heavy resonances decaying into bosonic and
 2055 leptonic final states using 36 fb^{-1} of proton-proton collision data at $\sqrt{s} = 13$ TeV with the ATLAS
 2056 detector. 2018.
- 2057 [74] G. Aad and t. . others.
- 2058 [75] J. K. Behr, D. Bortoletto, J. A. Frost, N. P. Hartland, C. Issever, and J. Rojo. Boosting Higgs pair
 2059 production in the $b\bar{b}b\bar{b}$ final state with multivariate techniques. *Eur. Phys. J.*, C76(7):386, 2016. doi:
 2060 10.1140/epjc/s10052-016-4215-5.
- 2061 [76] Study of the double Higgs production channel $H(\rightarrow b\bar{b})H(\rightarrow \gamma\gamma)$ with the ATLAS experiment
 2062 at the HL-LHC. Technical Report ATL-PHYS-PUB-2017-001, CERN, Geneva, Jan 2017. URL
 2063 <https://cds.cern.ch/record/2243387>.
- 2064 [77] Higgs pair production at the High Luminosity LHC. Technical Report CMS-PAS-FTR-15-002,
 2065 CERN, Geneva, 2015. URL <https://cds.cern.ch/record/2063038>.
- 2066 [78] N. P. Hartland. Double Higgs production from $HH \rightarrow (b\bar{b})(b\bar{b})$ at a 100 TeV hadron collider. *PoS*,
 2067 DIS2016:115, 2016.

- 2068 [79] S. V. Chekanov, M. Beydler, A. V. Kotwal, L. Gray, S. Sen, N. V. Tran, S. S. Yu, and J. Zuzelski.
2069 Initial performance studies of a general-purpose detector for multi-TeV physics at a 100 TeV pp
2070 collider. *JINST*, 12(06):P06009, 2017. doi: 10.1088/1748-0221/12/06/P06009.
- 2071 [80] S. Chekanov. Boosted jets in high-granularity calorimeter at a 100 TeV pp collider. BOOST 2017,
2072 2017.
- 2073 [81] S. Chekanov. Physics requirements for a Hadron Calorimeter for a 100 TeV proton-proton collider.
2074 FCC week 2015, 2015.
- 2075 [82] S. Chekanov. Simulation of a high-granular hadronic calorimeter for multi-TeV physics. FCC week
2076 2016, 2016.
- 2077 [83] J. Alwall, M. Herquet, F. Maltoni, O. Mattelaer, and T. Stelzer.
- 2078 [84] T. Sjostrand, S. Mrenna, and P. Z. Skands. A Brief Introduction to PYTHIA 8.1. *Comput. Phys.*
2079 *Commun.*, 178:852–867, 2008. doi: 10.1016/j.cpc.2008.01.036.
- 2080 [85] J. de Favereau, C. Delaere, P. Demin, A. Giammanco, V. Lematre, A. Mertens, and M. Selvaggi.
2081 DELPHES 3, A modular framework for fast simulation of a generic collider experiment. *JHEP*, 02:
2082 057, 2014. doi: 10.1007/JHEP02(2014)057.
- 2083 [86] E. Boos et al. Generic user process interface for event generators. In *Physics at TeV colliders.*
2084 *Proceedings, Euro Summer School, Les Houches, France, May 21-June 1, 2001*, 2001. URL
2085 <http://lss.fnal.gov/archive/preprint/fermilab-conf-01-496-t.shtml>.
- 2086 [87] M. Cacciari, G. P. Salam, and G. Soyez. FastJet User Manual. *Eur. Phys. J.*, C72:1896, 2012. doi:
2087 10.1140/epjc/s10052-012-1896-2.
- 2088 [88] D. Buskulic et al. Performance of the ALEPH detector at LEP. *Nucl. Instrum. Meth.*, A360:481–506,
2089 1995. doi: 10.1016/0168-9002(95)00138-7.
- 2090 [89] Particle-Flow Event Reconstruction in CMS and Performance for Jets, Taus, and MET. Technical
2091 Report CMS-PAS-PFT-09-001, CERN, Geneva, Apr 2009. URL <http://cds.cern.ch/record/1194487>.
- 2093 [90] FCC study group. Fccsw. <https://github.com/HEP-FCC/FCCSW>, 2018.
- 2094 [91] G. Barrand et al. GAUDI - A software architecture and framework for building HEP data processing
2095 applications. *Comput. Phys. Commun.*, 140:45–55, 2001. doi: 10.1016/S0010-4655(01)00254-5.
- 2096 [92] F. Gaede, B. Hegner, and P. Mato. Podio: An event-data-model toolkit for high energy physics
2097 experiments. *Journal of Physics: Conference Series*, 898(7):072039, 2017. URL <http://stacks.iop.org/1742-6596/898/i=7/a=072039>.
- 2099 [93] FCC-hh study group. Eventproducer. <https://github.com/FCC-hh-framework/EventProducer>,
2100 2018.

- 2101 [94] N. D. Christensen and C. Duhr. FeynRules - Feynman rules made easy. *Comput. Phys. Commun.*,
2102 180:1614–1641, 2009. doi: 10.1016/j.cpc.2009.02.018.
- 2103 [95] T. general Two-Higgs-Doublet Model. C. degrande, c. duhr, m. herquet, 2018. URL <http://feynrules.irmp.ucl.ac.be/wiki/2HDM>.
- 2105 [96] C. Degrande. Automatic evaluation of UV and R2 terms for beyond the Standard Model La-
2106 grangians: a proof-of-principle. *Comput. Phys. Commun.*, 197:239–262, 2015. doi: 10.1016/j.
2107 cpc.2015.08.015.
- 2108 [97] H. E. Haber and O. Stl. New LHC benchmarks for the \mathcal{CP} -conserving two-Higgs-doublet
2109 model. *Eur. Phys. J.*, C75(10):491, 2015. doi: 10.1140/epjc/s10052-015-3697-x, 10.1140/epjc/
2110 s10052-016-4151-4. [Erratum: Eur. Phys. J.C76,no.6,312(2016)].
- 2111 [98] D. de Florian et al. Handbook of LHC Higgs Cross Sections: 4. Deciphering the Nature of the
2112 Higgs Sector. 2016. doi: 10.23731/CYRM-2017-002.
- 2113 [99] M. Grazzini, G. Heinrich, S. Jones, S. Kallweit, M. Kerner, J. M. Lindert, and J. Mazzitelli. Higgs
2114 boson pair production at NNLO with top quark mass effects. *JHEP*, 05:059, 2018. doi: 10.1007/
2115 JHEP05(2018)059.
- 2116 [100] C. Patrignani et al. Review of Particle Physics. *Chin. Phys.*, C40(10):100001, 2016. doi: 10.1088/
2117 1674-1137/40/10/100001.
- 2118 [101] T. Sjostrand, S. Mrenna, and P. Z. Skands. PYTHIA 6.4 Physics and Manual. *JHEP*, 05:026, 2006.
2119 doi: 10.1088/1126-6708/2006/05/026.
- 2120 [102] M. Aaboud et al. Search for pair production of Higgs bosons in the $b\bar{b}b\bar{b}$ final state using proton-
2121 proton collisions at $\sqrt{s} = 13$ TeV with the ATLAS detector. 2018.
- 2122 [103] C. Helsens. Heavy resonances at 100tev, 2018. URL https://indico.cern.ch/event/704428/contributions/2957537/attachments/1627728/2594323/Resonances_FCC_hh_helsens.pdf.

2124 **Appendix A**

2125 **Jet radius discussion**

2126 It is important to discuss if the radius of the jet that is used to reconstruct the boosted Higgs boson
2127 candidates ($R = 0.8$) is the appropriate one. The question arises because in ATLAS boosted objects
2128 with $p_T \sim 200$ GeV are reconstructed using $R = 1.0$ jets. In this work, we work with a CM energy of 100
2129 TeV and require that the two leading jets have $p_T > 200$ GeV and use jets with $R = 0.8$. It is necessary
2130 to understand if these jets are large enough to fully reconstruct the Higgs candidates.

2131 As a first approximation we compute the angle between the b quarks produced by the decay of
2132 a Higgs boson. We assume that the b quarks are massless and that the Higgs moves only in the
2133 transverse plane (perpendicular to the beam pipe) such that it has no longitudinal momentum and the
2134 angle between the b quarks is given by $\Delta\phi$. For $p_T(\text{Higgs}) = 200$ GeV, we get $\Delta\phi(b, \bar{b}) = 1.1$ which is
2135 smaller than the jet's diameter (1.6) and therefore the two b quarks can both be contained inside the jet
2136 and the Higgs boson fully reconstructed.

2137 Another test we can make is to compute the
2138 ΔR between the b quarks coming from the lead-
2139 ing Higgs candidate with p_T larger than a given
2140 value, using truth level information. In figure A.1
2141 we show the distribution of $\Delta R(b, \bar{b})$ for p_T of
2142 the leading Higgs candidate larger than 200 GeV
2143 (solid blue) and 300 GeV (solid black). To obtain
2144 the dashed histograms we apply the p_T to both
2145 Higgs candidates. The integral of the histograms
2146 between 0 and 1.6 gives an estimate of the frac-
2147 tion of signal we keep if we apply these p_T cuts.
2148 For $p_T(h_1) > 200(300)$ GeV we get that 93(98) %
2149 of the signal has b quarks with $\Delta R < 1.6$ and
2150 therefore can be fully reconstructed using a jet with $R = 0.8$.

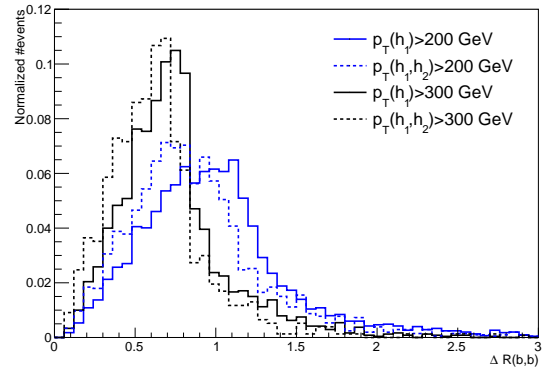


Figure A.1: $\Delta R(b, \bar{b})$ distributions for $p_T(h_1) > 200/300$ GeV (solid blue/black) and for $p_T(h_1, h_2) > 200/300$ GeV (dashed blue/black).

2151 **Appendix B**

2152 **Additional background processes**

2153 In this section we discuss the importance of additional background processes and estimate how they
2154 influence the analysis. In particular, we investigate backgrounds involving Higgs bosons. We consider
2155 the $t\bar{t}h$ and $h + 0/1/2 j$ processes. The effective cross section, efficiency and expected number of events
2156 for an integrated luminosity of $\mathcal{L} = 30 \text{ ab}^{-1}$ are summarized in table B.1. Including these backgrounds
2157 in the analysis leads to a decrease in the significance of 0.26%, which we consider to be a very small
2158 effect. Therefore, neglecting these backgrounds is a safe assumption.

Table B.1: Effective cross section ($\sigma \times \text{BR} \times \text{k-factor}$), efficiency and expected number of events for $\mathcal{L} = 30 \text{ ab}^{-1}$ for the $t\bar{t}h + 0/1 j(h \rightarrow b\bar{b})$ and $h + 0/1/2 j(h \rightarrow b\bar{b})$ backgrounds.

Process	$\sigma \times \text{BR} \times \text{k-factor} [\text{pb}]$	Efficiency [%]	Expected nb. events ($\mathcal{L} = 30 \text{ ab}^{-1}$)
$t\bar{t}h + 0/1 j(h \rightarrow b\bar{b})$	31.86	0.089	8.5×10^5
$h + 0/1/2 j(h \rightarrow b\bar{b})$	1286.52	0.0041	1.6×10^6

2159 In addition, we also estimate the error associated with not considering the a sample of $4b + j$ with
2160 $p_T(j) < 200 \text{ GeV}$. In order to do so, we generate a sample with 110k events of $4b + j$ with $(30 < p_T(j) <$
2161 $200) \text{ GeV}$. The cross section is $\sigma = 7450 \text{ pb}$. No event goes through the cuts $p_T(\text{leading jet}) > 300$
2162 GeV and $p_T(\text{Higgs pair}) > 100 \text{ GeV}$. However, if we assume that 1 events goes through the cuts (which
2163 corresponds to a very conservative $9.09 \times 10^{-4}\%$ efficiency) we have an expected number of events of
2164 2.03×10^6 for an integrated luminosity of $\mathcal{L} = 30 \text{ ab}^{-1}$. If we include this background, the significance
2165 decreases by 0.22% which is a very small effect. Therefore, it is safe to neglect this background.

2166 **Appendix C**

2167 **Softdrop mass**

2168 It is noticeable in the softdrop mass spectrum of both Higgs candidates (for signal and backgrounds) the
2169 existence an atypical peak close to zero. In this section we explain the origin of this feature.

2170 We believe that the peak close to zero corresponds to Higgs candidates ($R = 0.8$ jets) that do not
2171 contain both b quarks from the Higgs decay. The plot that supports this conclusion is shown in figure
2172 C.1. It shows the correlation between the maximum ΔR between the Higgs candidate jet axis and one
2173 of the b quarks (y axis) and the jet's mass (x axis). The horizontal line corresponds to $\Delta R = 0.8$. For
2174 small masses (< 80 GeV) the maximum ΔR is usually larger than 0.8 which means that at least one
2175 of the b quarks is not contained in the jet's cone. When applying the soft drop procedure to these jets,
2176 soft radiation is removed and we are left with a single b quark. The mass of b quarks is ~ 5 GeV and
2177 therefore we get a peak at this mass.

2178 In practice, this does not affect our analysis because we place a mass window cut around the Higgs
2179 boson mass and therefore the low mass peak is removed. Nonetheless, the study presented here is
2180 extremely important because it helps rule out possible malfunctions of the soft drop algorithm and gives
2181 us confidence that we understand exactly what is happening.

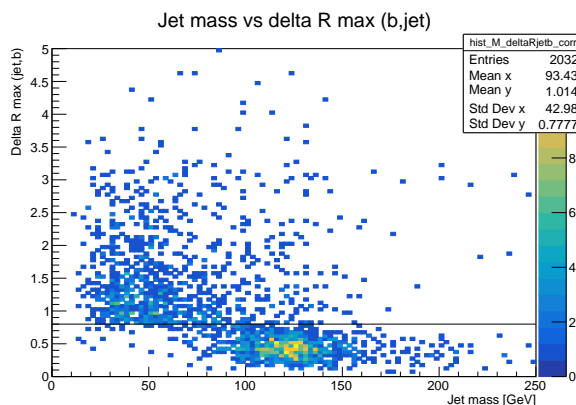


Figure C.1: Correlation between the maximum ΔR between the Higgs candidate jet and one of the b quarks (y axis) and the jet's mass (x axis). The horizontal line corresponds to $\Delta R = 0.8$.

2182 **Appendix D**

2183 **Samples generation: parameters**

2184 In this appendix we list the values of parameters used in MadGraph (section D.1) and Pythia (section
2185 D.2) to generate the samples used in this work.

2186 **D.1 MadGraph**

2187 The MadGraph5 level cuts are summarized in table D.1. We show only the most relevant cuts for this
2188 analysis: the minimum p_T of light and b quarks, $p_{T,j}^{\min}$ and $p_{T,b}^{\min}$, the maximum pseudorapidity range for
2189 light and b quarks, η_j^{\max} and η_b^{\max} and the ΔR separation between two light quarks, $\Delta R(jj)$, two b
2190 quarks, $\Delta R(bb)$, and between a light and b quarks, $\Delta R(jb)$. The $xqcut$ parameter is a measure of the
2191 required parton separation at Madgraph level. Whenever MadGraph produces two partons, i and j , it
2192 defines the distance between them as $\sqrt{2 * \min(p_{T,i}, p_{T,j}) [\cosh(\eta_i - \eta_j) - \cos(\phi_i - \phi_j)]}$. If the value of
2193 this expression is smaller than the specified value of $xqcut$ then we do not generate the event. The
2194 $bwcutoff$ parameter defines what is considered to be on-shell s-channel resonances. The H_T variable
2195 is the scalar sum of the p_T of all truth level partons, including b quarks.

2196 **D.2 Pythia**

2197 The settings for jet matching can be found in table D.2 under the corresponding samples' columns. We
2198 perform the jet matching procedure (merge=on) using the MLM matching scheme and the appropriate
2199 algorithm for a parton level process generated in MadGraph (scheme=1). We do not read the matching
2200 parameters from the MadGraph file (setMad=off) because this option is not available for these files.
2201 The size of the cone drawn around the jet's center, the maximum pseudorapidity and the maximum
2202 number of jets to be matched are given by coneRadius, etaJetMax and nJetMax, respectively. The cone
2203 radius is set to one. The maximum allowed pseudorapidity of jets is ten which is a much loser cut than
2204 the acceptance of any current or future detector. The maximum number of jets is set to four for the
2205 $jj + 0/1/2 j$ and to two for the $t\bar{t} + 0/1/2 j$. The $qCut$ parameter defines the k_T scale for merging shower
2206 products into jets.

Table D.1: Generator (MadGraph5) level cuts for the signal and background samples.

MadGraph5	SM ($h \rightarrow b\bar{b}$) & BSM hh	hh & 4b+j (QCD)	4b+j (QCD+EWK)	4b+j (EWK)	jj+0/1/2 j	tt+0/1/2 j
$p_{T,j}^{\min}, p_{T,b}^{\min}$ [GeV]	0	200; 30 500; 30	20; 15	20; 15	20; 5	5; 5
$\eta_j^{\max}, \eta_b^{\max}$	—	5; 5	5; 3	5; 3	8; 8	8; 8
$\Delta R(jj), \Delta R(bb), \Delta R(jb)$	0.001	0.4; 0.1; 0.3	0.4; 0.2; 0.4	0.4; 0.2; 0.4	0; 0.001; 0.001	0.001
xqcut [GeV]	0	0	0	0	20	60
bwcutoff [GeV]	30	15	15	15	30	30
H_T	—	—	—	—	0 – 500 500 – 1k 1k – 2k 2k – 4k 4k – 7.2k 7.2k – 15k 15k – 25k 25k – 35k 35k – 100k	—

Table D.2: Pythia settings for the signal and background samples.

Pythia	hh ($h \rightarrow b\bar{b}$)	4b+j	jj+0/1/2 j	tt+0/1/2 j
Relevant settings	25:onMode=off 25:onIfAny= 5 -5	—	Jet matching: merge=on scheme=1 setMad=off coneRadius=1.0 etaJetMax=10 nJetMax=4 qCut=30	Jet matching: merge=on scheme=1 setMad=off coneRadius=1.0 etaJetMax=10 nJetMax=2 qCut=60
Description	Turn on the $h \rightarrow b\bar{b}$ decay for the undecayed Higgs, in the case of the SM sample, or for both Higgs in the case of the BSM samples.	—	Set the parameters for jet matching (a detailed description can be found in the text).	

2207 Appendix E

2208 Cutflow tables

2209 In this appendix we summarize the significances achieved with the different detector configurations and for
 2210 the SM (table E.1), DM mediator (in black) and 2HDM (in blue) (table E.2) signal samples. In addition,
 2211 we collect the cutflow tables for the baseline and optimized analysis, for particle flow and calorimeter jets
 2212 and for all detector configurations that were tested. The efficiencies of the cuts are shown for all cuts.

Table E.1: Summary of the significances obtained with particle flow and calorimeter jets for the baseline and optimized analysis for the SM signal.

Configuration	Eflow jets		HCAL jets	
	Baseline	Optimized	Baseline	Optimized
ATLAS	$4.4^{+2.1}_{-1.6}$; 4.4 ^{+2.1} _{-1.6}	$5.7^{+3.1}_{-2.4}$	$2.50^{+1.3}_{-0.9}$	$3.5^{+1.8}_{-1.4}$
ATLAS gran.	$4.6^{+2.3}_{-1.6}$	$7.5^{+3.7}_{-2.9}$	$3.0^{+1.5}_{-1.2}$	$5.6^{+3.4}_{-3.0}$
ATLAS gran. $\eta \times 4$	$5.4^{+2.7}_{-2.0}$	$6.1^{+3.0}_{-2.3}$	$4.0^{+2.1}_{-1.7}$	$4^{+2.0}_{-1.6}$
FCC gran. $\phi/2$	$4.8^{+2.4}_{-1.7}$	$7.5^{+3.7}_{-2.8}$	$4.9^{+2.5}_{-1.8}$	$6.3^{+3.0}_{-2.2}$
FCC	$5.1^{+2.6}_{-1.9}$	$8.8^{+4.4}_{-3.4}$	$4.2^{+2.2}_{-1.6}$	$5.8^{+3.0}_{-2.3}$
FCC gran. $\eta, \phi \times 2$	$5.1^{+2.5}_{-1.8}$	$7.4^{+3.9}_{-3.0}$	$4.5^{+2.2}_{-1.6}$	6^{+3}_{-3}

Table E.2: Summary of the significances obtained with particle flow and calorimeter jets for the baseline and optimized analysis for the DM mediator and 2HDM signal processes.

Configuration	Eflow jets		HCAL jets	
	Baseline	Optimized	Baseline	Optimized
ATLAS	$1.24^{+0.62}_{-0.45}$; $7.2^{+3.6}_{-2.6}$	$1.50^{+0.75}_{-0.57}$; $11.3^{+5.6}_{-4.3}$	$0.71^{+0.36}_{-0.26}$; $4.5^{+2.3}_{-1.6}$	$0.90^{+0.47}_{-0.36}$; $7.4^{+3.8}_{-2.9}$
ATLAS gran.	$1.28^{+0.64}_{-0.47}$; $7.6^{+3.8}_{-2.8}$	$2.0^{+1.0}_{-0.8}$; $14.7^{+7.4}_{-5.8}$	$0.86^{+0.45}_{-0.36}$; $5.7^{+3.0}_{-2.4}$	$1.5^{+0.9}_{-0.8}$; 12^{+7}_{-7}
ATLAS gran. $\eta \times 4$	$1.51^{+0.75}_{-0.55}$; $8.9^{+4.4}_{-3.3}$	$1.60^{+0.80}_{-0.61}$; $12.0^{+6.0}_{-4.5}$	$1.14^{+0.61}_{-0.48}$; $7.4^{+4.0}_{-3.1}$	$0.90^{+0.50}_{-0.40}$; $7.6^{+4.2}_{-3.4}$
FCC gran. $\phi/2$	$1.33^{+0.66}_{-0.48}$; $7.8^{+3.9}_{-2.8}$	$1.96^{+0.96}_{-0.73}$; $14.3^{+7.0}_{-5.3}$	$1.36^{+0.69}_{-0.51}$; $7.9^{+4.1}_{-3.0}$	$1.62^{+0.81}_{-0.64}$; $12.6^{+6.3}_{-5.0}$
FCC	$1.43^{+0.72}_{-0.52}$; $8.4^{+4.2}_{-3.1}$	$2.3^{+1.2}_{-0.9}$; $16.9^{+8.5}_{-6.6}$	$1.18^{+0.61}_{-0.44}$; $6.8^{+3.5}_{-2.5}$	$1.51^{+0.78}_{-0.59}$; $11.6^{+6.0}_{-4.7}$
FCC gran. $\eta, \phi \times 2$	$1.42^{+0.71}_{-0.51}$; $8.3^{+4.1}_{-3.0}$	$1.95^{+0.96}_{-0.73}$; $14.2^{+7.0}_{-5.3}$	$1.26^{+0.63}_{-0.46}$; $7.2^{+3.6}_{-2.6}$	$1.52^{+0.78}_{-0.59}$; $11.5^{+5.9}_{-4.5}$

Table E.3: Cumulative efficiency, in percentage, of each event selection criterion of the baseline analysis for the signal background samples, for particle flow jets (black) and calorimeter jets (blue). The double horizontal line marks the pre-selection cuts. These results were obtained using the ATLAS default detector, as implemented in Delphes.

Selection [ATLAS]	$hh \rightarrow b\bar{b}b\bar{b}$ (SM)	$hh \rightarrow b\bar{b}b\bar{b}$ (DM mediator)	$hh \rightarrow b\bar{b}b\bar{b}$ (2HDM)	$4b + j$	$jj + 0/1/2j$	$t\bar{t}$
Gen level	100; 100	100; 100	100; 100	100; 100	100; 100	100; 100
No. b-tags ≥ 4	88.690; 83.646	88.787; 83.734	89.643; 84.492	71.617; 66.487	3.749; 3.354	51.782; 46.516
$p_T(j_1, j_2) \geq 200$ GeV	15.533; 13.966	15.941; 14.367	32.181; 29.749	16.299; 14.290	0.685; 0.601	0.985; 0.862
<hr/>						
$p_T(j_1) \geq 400$ GeV	7.997; 7.136	8.499; 7.615	19.446; 17.408	6.378; 5.540	0.170; 0.148	0.416; 0.370
$p_T(j_2) \geq 350$ GeV	5.282; 4.707	5.704; 5.104	11.944; 10.394	3.560; 3.075	0.112; 0.097	0.245; 0.218
$p_T(j_1 + j_2) \geq 100$ GeV	4.304; 3.833	4.604; 4.117	8.764; 7.687	3.000; 2.580	0.065; 0.057	0.207; 0.182
$\tau_{21}(j_1) < 0.55$	3.257; 2.805	3.490; 3.022	6.776; 5.839	1.288; 1.380	0.021; 0.032	0.122; 0.107
$\tau_{21}(j_2) < 0.55$	1.648; 1.619	1.809; 1.764	3.779; 3.571	0.545; 0.685	0.008; 0.015	0.064; 0.060
$FW2(j_1) > 0.2$	1.125; 0.724	1.243; 0.795	2.797; 1.836	0.272; 0.189	0.003; 0.003	0.016; 0.008
$(100 < M_{SD}(j1) < 135)$ GeV	0.724; 0.406	0.815; 0.453	2.029; 1.186	0.047; 0.028	0.000; 0.0003	0.003; 0.002
$(100 < M_{SD}(j2) < 135)$ GeV	0.323; 0.157	0.374; 0.184	1.019; 0.545	0.010; 0.005	0.00007; 0.00005	0.00007; 0.00005

Table E.4: Cumulative efficiency, in percentage, of each event selection criterion of the baseline analysis for the signal background samples, for particle flow jets (black) and calorimeter jets (blue). The double horizontal line marks the pre-selection cuts. These results were obtained using the ATLAS granularity.

Selection [ATLAS gran.]	$hh \rightarrow b\bar{b}b\bar{b}$ (SM)	$hh \rightarrow b\bar{b}b\bar{b}$ (DM mediator)	$hh \rightarrow b\bar{b}b\bar{b}$ (2HDM)	$4b + j$	$jj + 0/1/2j$	$t\bar{t}$
Gen level	100; 100	100; 100	100; 100	100; 100	100; 100	100; 100
No. b-tags ≥ 4	92.226; 85.810	92.322; 85.896	93.202; 86.654	75.464; 67.886	3.930; 3.448	53.144; 45.851
$p_T(j_1, j_2) \geq 200$ GeV	16.504; 14.820	16.918; 15.204	33.819; 31.045	17.580; 15.152	0.732; 0.644	1.043; 0.917
<hr/>						
$p_T(j_1) \geq 400$ GeV	8.550; 7.527	9.069; 8.007	20.789; 18.503	6.890; 5.900	0.181; 0.157	0.443; 0.392
$p_T(j_2) \geq 350$ GeV	5.662; 4.977	6.104; 5.390	12.977; 11.293	3.867; 3.295	0.120; 0.105	0.261; 0.232
$p_T(j_1 + j_2) \geq 100$ GeV	4.610; 4.037	4.928; 4.336	9.487; 8.249	3.249; 2.761	0.069; 0.061	0.221; 0.195
$\tau_{21}(j_1) < 0.55$	3.482; 2.653	3.729; 2.851	7.324; 5.629	1.362; 1.193	0.021; 0.027	0.130; 0.097
$\tau_{21}(j_2) < 0.55$	1.649; 1.300	1.813; 1.419	3.902; 2.991	0.535; 0.483	0.007; 0.010	0.063; 0.047
$FW2(j_1) > 0.2$	1.157; 0.468	1.280; 0.509	2.966; 1.264	0.276; 0.117	0.003; 0.001	0.016; 0.005
$(100 < M_{SD}(j1) < 135)$ GeV	0.761; 0.235	0.859; 0.267	2.197; 0.761	0.048; 0.013	0.0004; 0.0001	0.004; 0.001
$(100 < M_{SD}(j2) < 135)$ GeV	0.365; 0.099	0.424; 0.118	1.174; 0.369	0.011; 0.002	0.00008; 0.00001	0.0008; 0.0003

Table E.5: Cumulative efficiency, in percentage, of each event selection criterion of the baseline analysis for the signal background samples, for particle flow jets (black) and calorimeter jets (blue). The double horizontal line marks the pre-selection cuts. These results were obtained using the ATLAS granularity with $\eta \times 4$.

Selection [ATLAS gran. $\eta \times 4$]	$hh \rightarrow b\bar{b}b\bar{b}$ (SM)	$hh \rightarrow b\bar{b}b\bar{b}$ (DM mediator)	$hh \rightarrow b\bar{b}b\bar{b}$ (2HDM)	$4b + j$	$jj + 0/1/2j$	$t\bar{t}$
Gen level	100; 100	100; 100	100; 100	100; 100	100; 100	100; 100
No. b-tags ≥ 4	92.259; 87.076	92.358; 87.167	93.224; 88.043	70.510; 69.147	3.935; 3.523	53.198; 46.560
$p_T(j_1, j_2) \geq 200$ GeV	16.544; 15.131	16.965; 15.566	33.860; 31.667	17.626; 15.567	0.734; 0.665	1.044; 0.938
<hr/>						
$p_T(j_1) \geq 400$ GeV	8.577; 7.697	9.096; 8.203	20.889; 18.877	6.918; 6.079	0.181; 0.162	0.443; 0.400
$p_T(j_2) \geq 350$ GeV	5.682; 5.091	6.126; 5.524	13.064; 11.536	3.875; 3.399	0.120; 0.108	0.261; 0.237
$p_T(j_1 + j_2) \geq 100$ GeV	4.630; 4.139	4.944; 4.442	9.545; 8.447	3.263; 2.852	0.069; 0.062	0.222; 0.200
$\tau_{21}(j_1) < 0.55$	3.518; 2.683	3.758; 2.889	7.397; 5.694	1.359; 1.138	0.020; 0.024	0.131; 0.097
$\tau_{21}(j_2) < 0.55$	1.661; 1.249	1.825; 1.371	3.937; 2.913	0.530; 0.432	0.006; 0.008	0.065; 0.044
$FW2(j_1) > 0.2$	1.182; 0.538	1.309; 0.595	3.031; 1.457	0.281; 0.127	0.003; 0.001	0.017; 0.005
$(100 < M_{SD}(j1) < 135)$ GeV	0.781; 0.289	0.886; 0.329	2.258; 0.932	0.049; 0.016	0.0003; 0.0001	0.004; 0.001
$(100 < M_{SD}(j2) < 135)$ GeV	0.377; 0.128	0.437; 0.152	1.209; 0.466	0.011; 0.003	0.00006; 0.00001	0.0009; 0.0002

Table E.6: Cumulative efficiency, in percentage, of each event selection criterion of the baseline analysis for the signal background samples, for particle flow jets (black) and calorimeter jets (blue). The double horizontal line marks the pre-selection cuts. These results were obtained using the FCC granularity with $\phi/2$.

Selection [FCC gran. $\phi/2$]	$hh \rightarrow b\bar{b}b\bar{b}$ (SM)	$hh \rightarrow b\bar{b}b\bar{b}$ (DM mediator)	$hh \rightarrow b\bar{b}b\bar{b}$ (2HDM)	$4b + j$	$jj + 0/1/2j$	$t\bar{t}$
Gen level	100; 100	100; 100	100; 100	100; 100	100; 100	100; 100
No. b-tags ≥ 4	92.473; 90.243	92.567; 90.345	93.422; 91.223	75.798; 72.741	3.961; 3.732	53.474; 48.883
$p_T(j_1, j_2) \geq 200$ GeV	16.603; 15.838	17.025; 16.255	33.965; 32.916	17.812; 16.706	0.740; 0.705	1.054; 0.983
<hr/>						
$p_T(j_1) \geq 400$ GeV	8.620; 8.091	9.149; 8.606	21.030; 19.759	7.004; 6.534	0.182; 0.172	0.301; 0.419
$p_T(j_2) \geq 350$ GeV	5.707; 5.346	6.160; 5.786	13.185; 12.110	3.922; 3.644	0.120; 0.113	0.263; 0.248
$p_T(j_1 + j_2) \geq 100$ GeV	4.644; 4.336	4.966; 4.651	9.610; 8.858	3.307; 3.062	0.069; 0.064	0.222; 0.209
$\tau_{21}(j_1) < 0.55$	3.630; 3.044	3.886; 3.271	7.617; 6.360	1.371; 1.027	0.018; 0.014	0.138; 0.109
$\tau_{21}(j_2) < 0.55$	1.692; 1.238	1.861; 1.380	4.026; 2.980	0.534; 0.330	0.005; 0.003	0.069; 0.048
$FW2(j_1) > 0.2$	1.266; 0.783	1.403; 0.873	3.234; 2.087	0.314; 0.163	0.003; 0.002	0.020; 0.009
$(100 < M_{SD}(j1) < 135)$ GeV	0.853; 0.528	0.961; 0.601	2.432; 1.567	0.055; 0.026	0.0004; 0.0002	0.004; 0.002
$(100 < M_{SD}(j2) < 135)$ GeV	0.421; 0.279	0.483; 0.323	1.331; 0.883	0.014; 0.007	0.00001; 0.00004	0.0009; 0.0003

Table E.7: Cumulative efficiency, in percentage, of each event selection criterion of the baseline analysis for the signal background samples, for particle flow jets (black) and calorimeter jets (blue). The double horizontal line marks the pre-selection cuts. These results were obtained using the FCC default detector design.

Selection [FCC]	$hh \rightarrow b\bar{b}b\bar{b}$ (SM)	$hh \rightarrow b\bar{b}b\bar{b}$ (DM mediator)	$hh \rightarrow b\bar{b}b\bar{b}$ (2HDM)	$4b + j$	$jj + 0/1/2j$	$t\bar{t}$
Gen level	100; 100	100; 100	100; 100	100; 100	100; 100	100; 100
No. b-tags ≥ 4	92.488; 90.713	92.593; 90.805	93.436; 91.773	75.819; 73.318	3.960; 3.764	53.495; 49.121
$p_T(j_1, j_2) \geq 200$ GeV	16.56915.985	17.033; 16.397	33.975; 33.177	17.811; 16.902	0.742; 0.711	1.056; 0.991
<hr/>						
$p_T(j_1) \geq 400$ GeV	8.606; 8.187	9.156; 8.696	21.047; 19.941	7.008; 6.628	0.183; 0.174	0.446; 0.422
$p_T(j_2) \geq 350$ GeV	5.698; 5.419	6.161; 5.850	13.208; 12.243	3.927; 3.704	0.121; 0.115	0.263; 0.250
$p_T(j_1 + j_2) \geq 100$ GeV	4.639; 4.399	4.968; 4.707	9.630; 8.971	3.311; 3.114	0.070; 0.056	0.223; 0.211
$\tau_{21}(j_1) < 0.55$	3.638; 3.119	3.904; 3.340	7.663; 6.489	1.385; 1.031	0.018; 0.013	0.140; 0.113
$\tau_{21}(j_2) < 0.55$	1.702; 1.256	1.878; 1.391	4.059; 3.012	0.540; 0.327	0.005; 0.003	0.069; 0.048
$FW2(j_1) > 0.2$	1.279; 0.831	1.421; 0.922	3.270; 2.178	0.320; 0.174	0.003; 0.002	0.020; 0.009
$(100 < M_{SD}(j1) < 135)$ GeV	0.860; 0.566	0.973; 0.644	2.456; 1.652	0.056; 0.029	0.0004; 0.00002	0.004; 0.002
$(100 < M_{SD}(j2) < 135)$ GeV	0.421; 0.299	0.487; 0.348	1.343; 0.935	0.014; 0.008	0.00009; 0.00007	0.0008; 0.0005

Table E.8: Cumulative efficiency, in percentage, of each event selection criterion of the baseline analysis for the signal background samples, for particle flow jets (black) and calorimeter jets (blue). The double horizontal line marks the pre-selection cuts. These results were obtained using the FCC granularity with $\eta, \phi \times 2$.

Selection [FCC gran.]	$\eta, \phi \times 2]$	$hh \rightarrow b\bar{b}b\bar{b}$ (SM)	$hh \rightarrow b\bar{b}b\bar{b}$ (DM mediator)	$hh \rightarrow b\bar{b}b\bar{b}$ (2HDM)	$4b + j$	$jj + 0/1/2j$
Gen level		100; 100	100; 100	100; 100	100; 100	100; 100
No. b-tags ≥ 4	92.542; 91.202	92.621; 91.306	93.479; 92.348	75.847; 73.910	3.964; 3.794	53.516; 49.359
$p_T(j_1, j_2) \geq 200$ GeV	16.607; 16.139	17.048; 16.568	33.985; 33.441	17.836; 17.085	0.742; 0.718	1.053; 0.997
<hr/>						
$p_T(j_1) \geq 400$ GeV	8.631; 8.294	9.159; 8.806	21.0473; 20.139	7.020; 6.717	0.183; 0.177	0.446; 0.425
$p_T(j_2) \geq 350$ GeV	5.715; 5.485	4.121; 5.924	13.223; 12.366	3.937; 3.759	0.121; 0.117	0.263; 0.253
$p_T(j_1 + j_2) \geq 100$ GeV	4.651; 4.461	4.966; 4.760	9.638; 9.082	3.318; 3.161	0.069; 0.067	0.222; 0.212
$\tau_{21}(j_1) < 0.55$	3.662; 3.192	3.914; 3.413	7.685; 6.615	1.396; 1.053	0.018; 0.013	0.140; 0.115
$\tau_{21}(j_2) < 0.55$	1.721; 1.279	1.890; 1.419	4.086; 3.064	0.550; 0.334	0.005; 0.003	0.070; 0.050
$FW2(j_1) > 0.2$	1.297; 0.872	1.432; 0.949	3.295; 2.264	0.326; 0.183	0.003; 0.002	0.021; 0.011
$(100 < M_{SD}(j1) < 135)$ GeV	0.871; 0.593	0.978; 0.676	2.470; 1.714	0.056; 0.031	0.0005; 0.0002	0.004; 0.002
$(100 < M_{SD}(j2) < 135)$ GeV	0.425; 0.312	0.489; 0.364	1.343; 0.970	0.014; 0.008	0.00009; 0.00006	0.0009; 0.0006

Table E.9: Cumulative efficiency, in percentage, of each event selection criterion of the optimized analysis for the signal background samples, for particle flow jets (black) and calorimeter jets (blue). The double horizontal line marks the pre-selection cuts. These results were obtained using the ATLAS default detector, as implemented in Delphes.

Selection [ATLAS]	$hh \rightarrow b\bar{b}b\bar{b}$ (SM)	$hh \rightarrow b\bar{b}b\bar{b}$ (DM mediator)	$hh \rightarrow b\bar{b}b\bar{b}$ (2HDM)	$4b + j$	$jj + 0/1/2j$	$t\bar{t}$
Gen level	100; 100	100; 100	100; 100	100; 100	100; 100	100; 100
No. b-tags ≥ 4	88.690; 83.646	88.787; 83.734	89.643; 84.492	71.617; 66.487	3.749; 3.354	51.782; 46.516
$p_T(j_1, j_2) \geq 200$ GeV	15.533; 13.966	15.941; 14.367	32.181; 29.749	16.299; 14.299	0.685; 0.601	0.985; 0.862
<hr/>						
$p_T(j_1) \geq 300$ GeV	12.599; 11.276	13.061; 11.730	29.141; 26.835	11.627; 10.146	0.390; 0.338	0.669; 0.594
$p_T(j_1 + j_2) \geq 100$ GeV	10.185; 9.081	10.526; 9.423	21.523; 19.693	9.932; 8.632	0.227; 0.197	0.574; 0.508
$\tau_{21}(j_1) < 0.4$	4.980; 4.004	5.152; 4.149	11.327; 9.376	1.692; 1.738	0.026; 0.040	0.157; 0.136
$\tau_{21}(j_2) < 0.4$	1.139; 0.974	1.220; 1.035	3.411; 2.931	0.234; 0.276	0.003; 0.006	0.031; 0.029
$ \Delta\eta(h_h) < 1.5$	0.891; 0.753	0.960; 0.803	2.930; 2.494	0.113; 0.138	0.001; 0.003	0.019; 0.017
$FW2(j_1) > 0.2$	0.796; 0.567	0.858; 0.601	2.684; 1.965	0.082; 0.064	0.001; 0.001	0.010; 0.007
$(100 < M_{SD}(j1) < 135)$ GeV	0.610; 0.396	0.658; 0.422	2.138; 1.450	0.022; 0.016	0.0002; 0.0002	0.003; 0.003
$(100 < M_{SD}(j2) < 135)$ GeV	0.333; 0.182	0.360; 0.196	1.266; 0.753	0.005; 0.003	0.00004; 0.00003	0.0007; 0.0005

Table E.10: Cumulative efficiency, in percentage, of each event selection criterion of the optimized analysis for the signal background samples, for particle flow jets (black) and calorimeter jets (blue). The double horizontal line marks the pre-selection cuts. These results were obtained using the ATLAS granularity.

Selection [ATLAS gran.]	$hh \rightarrow b\bar{b}b\bar{b}$ (SM)	$hh \rightarrow b\bar{b}b\bar{b}$ (DM mediator)	$hh \rightarrow b\bar{b}b\bar{b}$ (2HDM)	$4b + j$	$jj + 0/1/2j$	$t\bar{t}$
Gen level	100; 100	100; 100	100; 100	100; 100	100; 100	100; 100
No. b-tags ≥ 4	88.690; 83.646	88.787; 83.734	89.643; 84.492	71.617; 66.487	3.749; 3.354	51.782; 46.516
$p_T(j_1, j_2) \geq 200$ GeV	15.533; 13.966	15.941; 14.367	32.181; 29.749	16.299; 14.299	0.685; 0.601	0.985; 0.862
<hr/>						
$p_T(j_1) \geq 300$ GeV	13.431; 11.950	13.902; 12.392	30.706; 28.059	12.552; 10.792	0.417; 0.364	0.709; 0.630
$p_T(j_1 + j_2) \geq 100$ GeV	10.860; 9.597	11.212; 9.929	22.721; 20.533	10.731; 9.185	0.241; 0.211	0.609; 0.538
$\tau_{21}(j_1) < 0.4$	5.324; 3.286	5.506; 3.391	12.005; 7.571	1.772; 1.209	0.025; 0.027	0.167; 0.108
$\tau_{21}(j_2) < 0.4$	1.131; 0.571	1.213; 0.604	3.479; 1.764	0.217; 0.126	0.002; 0.003	0.031; 0.016
$ \Delta\eta(hh) < 1.5$	0.920; 0.439	0.990; 0.465	3.054; 1.499	0.110; 0.1058	0.001; 0.001	0.019; 0.009
$FW2(j_1) > 0.2$	0.841; 0.304	0.903; 0.320	2.847; 1.097	0.084; 0.027	0.001; 0.0003	0.011; 0.003
$(100 < M_{SD}(j1) < 135)$ GeV	0.658; 0.202	0.710; 0.217	2.309; 0.767	0.022; 0.005	0.0001; 0.00001	0.004; 0.001
$(100 < M_{SD}(j2) < 135)$ GeV	0.375; 0.107	0.408; 0.117	1.424; 0.448	0.006; 0.001	0.00003; 0.000004	0.0007; 0.0002

Table E.11: Cumulative efficiency, in percentage, of each event selection criterion of the optimized analysis for the signal background samples, for particle flow jets (black) and calorimeter jets (blue). The double horizontal line marks the pre-selection cuts. These results were obtained using the ATLAS granularity with $\eta \times 4$.

Selection [ATLAS gran. $\eta \times 4$]		$hh \rightarrow b\bar{b}b\bar{b}$ (SM)	$hh \rightarrow b\bar{b}b\bar{b}$ (DM mediator)	$hh \rightarrow b\bar{b}b\bar{b}$ (2HDM)	$4b + j$	$jj + 0/1/2j$	$t\bar{t}$
Gen level		100; 100	100; 100	100; 100	100; 100	100; 100	100; 100
No. b-tags ≥ 4		88.690; 83.646	88.787; 83.734	89.643; 84.492	71.617; 66.487	3.749; 3.354	51.782; 46.516
$p_T(j_1, j_2) \geq 200$ GeV		15.533; 13.966	15.941; 14.367	32.181; 29.749	16.299; 14.299	0.685; 0.601	0.985; 0.862
<hr/>							
$p_T(j_1) \geq 300$ GeV		13.486; 12.229	13.938; 12.696	30.757; 28.621	12.600; 11.100	0.418; 0.375	0.711; 0.645
$p_T(j_1 + j_2) \geq 100$ GeV		10.889; 9.827	11.250; 10.179	22.773; 20.972	10.774; 9.456	0.242; 0.217	0.612; 0.550
$\tau_{21}(j_1) < 0.4$		5.407; 3.336	5.589; 3.439	12.187; 7.663	1.789; 1.139	0.024; 0.023	0.169; 0.106
$\tau_{21}(j_2) < 0.4$		1.158; 0.556	1.241; 0.591	3.550; 1.755	0.219; 0.111	0.002; 0.002	0.032; 0.015
$ \Delta\eta(hh) < 1.5$		0.944; 0.430	1.013; 0.455	3.116; 1.497	0.111; 0.051	0.001; 0.001	0.020; 0.009
$FW2(j_1) > 0.2$		0.863; 0.331	0.924; 0.348	2.914; 1.205	0.085; 0.027	0.001; 0.0003	0.011; 0.003
$(100 < M_{SD}(j1) < 135)$ GeV		0.676; 0.231	0.726; 0.242	2.371; 0.881	0.022; 0.006	0.001; 0.0001	0.004; 0.002
$(100 < M_{SD}(j2) < 135)$ GeV		0.386; 0.129	0.418; 0.136	1.466; 0.533	0.006; 0.002	0.00005; 0.00002	0.0009; 0.0002

Table E.12: Cumulative efficiency, in percentage, of each event selection criterion of the optimized analysis for the signal background samples, for particle flow jets (black) and calorimeter jets (blue). The double horizontal line marks the pre-selection cuts. These results were obtained using the FCC granularity with $\phi/2$.

	Selection [FCC gran. $\phi/2$]	$hh \rightarrow b\bar{b}b\bar{b}$ (SM)	$hh \rightarrow b\bar{b}b\bar{b}$ (DM mediator)	$hh \rightarrow b\bar{b}b\bar{b}$ (2HDM)	$4b + j$	$jj + 0/1/2j$	$4\bar{t}$
Gen level		100; 100	100; 100	100; 100	100; 100	100; 100	100; 100
No. b-tags ≥ 4		88.690; 83.646	88.787; 83.734	89.643; 84.492	71.617; 66.487	3.749; 3.354	51.782; 46.516
$p_T(j_1, j_2) \geq 200$ GeV		15.533; 13.966	15.941; 14.367	32.181; 29.749	16.299; 14.299	0.685; 0.601	0.985; 0.862
<hr/>							
96	$p_T(j_1) \geq 300$ GeV	13.526; 12.827	14.222; 13.292	30.805; 29.788	12.739; 11.917	0.421; 0.396	0.718; 0.674
	$p_T(j_1 + j_2) \geq 100$ GeV	10.936; 10 - 308	11.291; 10.664	22.806; 21.847	10.902; 10.164	0.244; 0.228	0.617; 0.575
	$\tau_{21}(j_1) < 0.4$	5.792; 4.306	5.987; 4.451	12.968; 9.837	1.928; 0.390	0.023; 0.015	0.186; 0.129
	$\tau_{21}(j_2) < 0.4$	1.286; 0.738	1.385; 0.792	3.888; 2.394	0.248; 0.106	0.002; 0.001	0.037; 0.019
	$ \Delta\eta(hh) < 1.5$	1.054; 0.608	1.135; 0.652	3.424; 2.127	0.127; 0.052	0.001; 0.0004	0.024; 0.012
	$FW2(j_1) > 0.2$	0.974; 0.534	1.046; 0.568	3.233; 1.930	0.102; 0.040	0.001; 0.0004	0.013; 0.005
	$(100 < M_{SD}(j1) < 135)$ GeV	0.770; 0.423	0.830; 0.453	2.645; 1.585	0.026; 0.010	0.0002; 0.0001	0.004; 0.002
	$(100 < M_{SD}(j2) < 135)$ GeV	0.442; 0.263	0.480; 0.281	1.641; 1.027	0.007; 0.003	0.00004; 0.00002	0.0009; 0.0005

Table E.13: Cumulative efficiency, in percentage, of each event selection criterion of the optimized analysis for the signal background samples, for particle flow jets (black) and calorimeter jets (blue). The double horizontal line marks the pre-selection cuts. These results were obtained using the FCC default detector.

Selection [FCC]	$hh \rightarrow b\bar{b}b\bar{b}$ (SM)	$hh \rightarrow b\bar{b}b\bar{b}$ (DM mediator)	$hh \rightarrow b\bar{b}b\bar{b}$ (2HDM)	$4b + j$	$jj + 0/1/2j$	$t\bar{t}$
Gen level	100; 100	100; 100	100; 100	100; 100	100; 100	100; 100
No. b-tags ≥ 4	88.690; 83.646	88.787; 83.734	89.643; 84.492	71.617; 66.487	3.749; 3.354	51.782; 46.516
$p_T(j_1, j_2) \geq 200$ GeV	15.533; 13.966	15.941; 14.367	32.181; 29.749	16.299; 14.299	0.685; 0.601	0.985; 0.862
<hr/>						
$p_T(j_1) \geq 300$ GeV	13.521; 12.943	14.007; 13.388	30.869; 30.029	12.744; 12.06	0.422; 0.401	0.718; 0.677
$p_T(j_1 + j_2) \geq 100$ GeV	10.933; 10.409	11.301; 10.748	22.863; 22.051	10.901; 10.291	0.245; 0.232	0.617; 0.580
$\tau_{21}(j_1) < 0.4$	5.838; 4.444	6.043; 4.585	13.104; 10.136	1.953; 1.252	0.023; 0.015	0.186; 0.133
$\tau_{21}(j_2) < 0.4$	1.309; 0.771	1.410; 0.826	3.953; 2.487	0.256; 0.111	0.002; 0.001	0.037; 0.020
$ \Delta\eta(hh) < 1.5$	1.071; 0.636	1.154; 0.680	3.479; 2.211	0.130; 0.055	0.001; 0.0005	0.024; 0.012
$FW2(j_1) > 0.2$	0.989; 0.566	1.064; 0.603	3.276; 2.030	0.105; 0.044	0.001; 0.0004	0.014; 0.006
$(100 < M_{SD}(j1) < 135)$ GeV	0.783; 0.452	0.844; 0.486	2.688; 1.676	0.026; 0.011	0.0002; 0.0001	0.004; 0.002
$(100 < M_{SD}(j2) < 135)$ GeV	0.446; 0.281	0.486; 0.303	1.666; 1.089	0.007; 0.003	0.00003; 0.000003	0.0007; 0.0005

Table E.14: Cumulative efficiency, in percentage, of each event selection criterion of the optimized analysis for the signal background samples, for particle flow jets (black) and calorimeter jets (blue). The double horizontal line marks the pre-selection cuts. These results were obtained using the FCC granularity with $\eta, \phi \times 2$.

	Selection [FCC gran.] $\eta, \phi \times 2]$	$hh \rightarrow b\bar{b}b\bar{b}$ (SM)	$hh \rightarrow b\bar{b}b\bar{b}$ (DM mediator)	$hh \rightarrow b\bar{b}b\bar{b}$ (2HDM)	$4b + j$	$jj + 0/1/2j$	$t\bar{t}$
Gen level		100; 100	100; 100	100; 100	100; 100	100; 100	100; 100
No. b-tags ≥ 4		88.690; 83.646	88.787; 83.734	89.643; 84.492	71.617; 66.487	3.749; 3.354	51.782; 46.516
$p_T(j_1, j_2) \geq 200$ GeV		15.533; 13.966	15.941; 14.367	32.181; 29.749	16.299; 14.299	0.685; 0.601	0.985; 0.862
<hr/>							
$p_T(j_1) \geq 300$ GeV		13.529; 13.087	14.012; 13.536	30.885; 30.483	12.762; 12.207	0.422; 0.406	0.716; 0.684
$p_T(j_1 + j_2) \geq 100$ GeV		10.941; 10.542	11.305; 10.875	22.874; 22.270	10.919; 10.291	0.244; 0.235	0.615; 0.583
$\tau_{21}(j_1) < 0.4$		5.869; 4.571	6.075; 4.716	13.170; 10.401	1.974; 1.296	0.024; 0.016	0.190; 0.137
$\tau_{21}(j_2) < 0.4$		1.321; 0.800	1.429; 0.861	3.991; 2.577	0.262; 0.117	0.002; 0.001	0.039; 0.021
$ \Delta\eta(hh) < 1.5$		1.078; 0.659	1.169; 0.710	3.508; 2.290	0.134; 0.058	0.001; 0.001	0.024; 0.013
$FW2(j_1) > 0.2$		0.997; 0.592	1.077; 0.635	3.302; 2.113	0.107; 0.047	0.001; 0.0004	0.013; 0.006
$(100 < M_{SD}(j1) < 135)$ GeV		0.787; 0.472	0.851; 0.512	2.708; 1.751	0.027; 0.011	0.0002; 0.0001	0.004; 0.002
$(100 < M_{SD}(j2) < 135)$ GeV		0.451; 0.292	0.490; 0.320	1.671; 1.133	0.007; 0.003	0.00004; 0.00003	0.0009; 0.0004

²²¹³ **Appendix F**

²²¹⁴ **Extra plots**

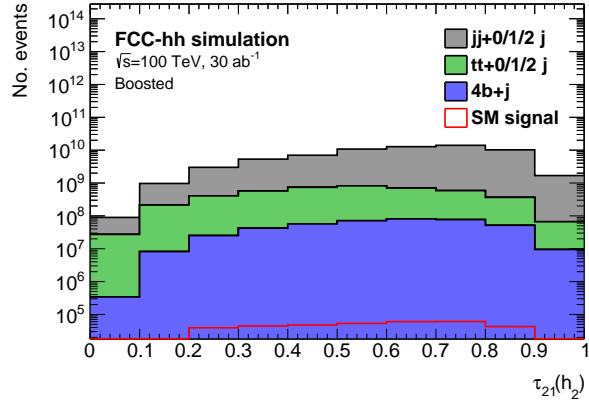


Figure F.1: τ_{21} distribution for the sub leading Higgs candidate for the baseline analysis. The histogram is normalized to $\mathcal{L} = 30 \text{ ab}^{-1}$.

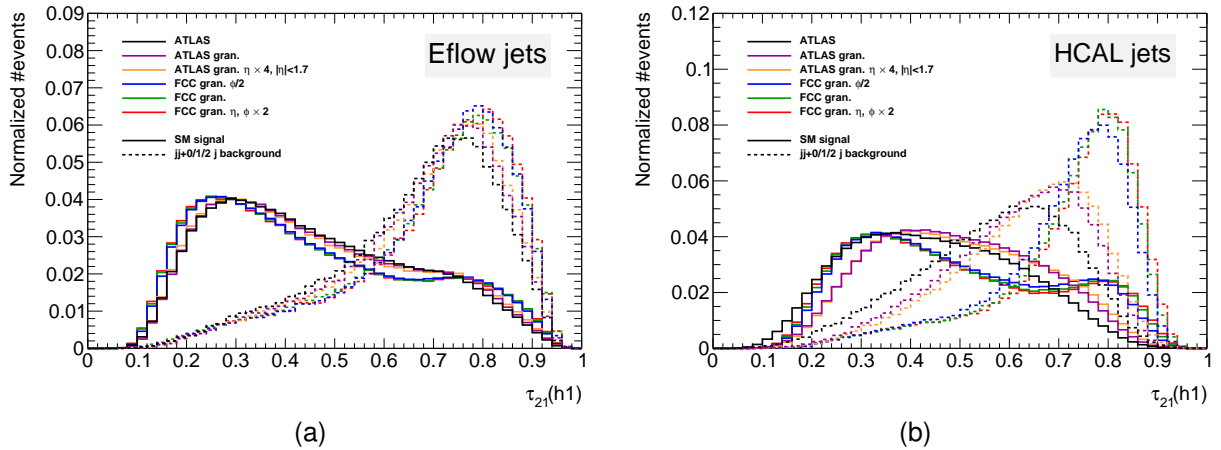


Figure F.2: Sub leading Higgs candidate τ_{21} distribution for eflow jets (a) and for HCAL jets (b). The colors indicate the different detector configurations. The distributions are shown for the signal (filled lines) and for the $jj + 0/1/2 j$ background (dashed lines).

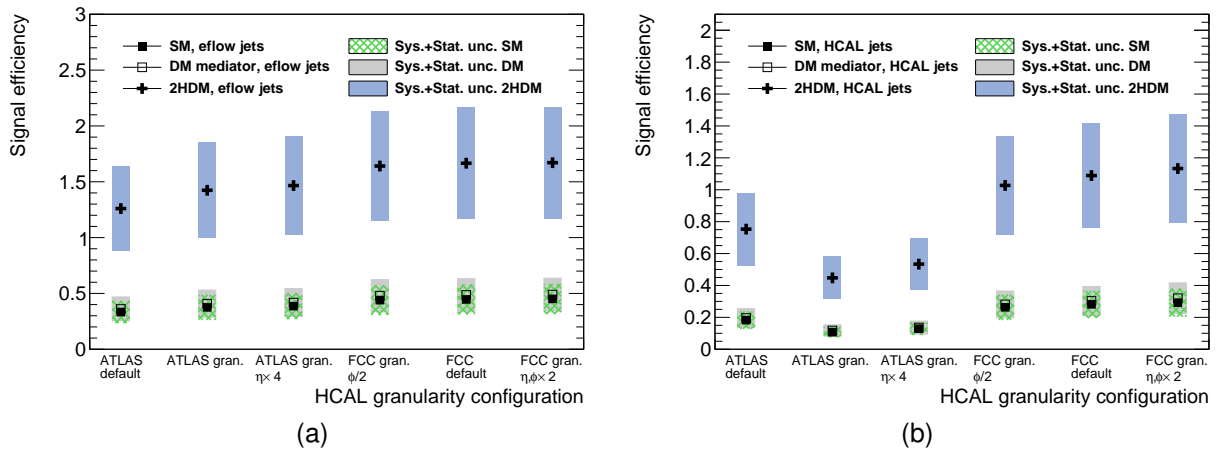


Figure F.3: Signal efficiency as a function of the detector configuration for particle flow jets (a) and for calorimeter jets (b). Three signal models are shown: SM (filled squares), 1 TeV DM mediator (empty squares) and type II 2HDM with $m_H = 900$ GeV (crosses). The statistical error bars are drawn but are smaller than the markers.